Advancing attosecond metrology

Markus Fieß

München 2010

Advancing attosecond metrology

Markus Fieß

Dissertation
an der Fakultät für Physik
der Ludwig-Maximilians-Universität
München

vorgelegt von
Markus Fieß
aus Oberkirch, Deutschland

München, den 11. Juni 2010

Erstgutachter: Prof. Dr. Ferenc Krausz
Zweitgutachter: Prof. Dr. Johannes Barth
Tag der mündlichen Prüfung: 29. Juli 2009

"Die Wissenschaft sucht nach einem Perpetuum mobile.
Sie hat es gefunden: Sie ist es selbst."

Victor Hugo, 1863

Contents

1 Abstract

Diese Arbeit ist zeitaufgelösten Experimenten über die schnellsten Phänomene, zu welchen die Wissenschaft momentan mittels Attosekundenlaserpulsen Zugang hat, gewidmet. Begleitet von der Entwicklung von Laserquellen im nahen Infrarot, im nahen Ultraviolett und im extremen Ultraviolett wurden große Bemühungen in die Konstruktion eines neuartigen experimentellen Aufbaus zur Durchführung von Anregungs-Abfrage-Experimenten auf einer Attosekundenzeitskala, welche bisher nicht möglich waren, investiert. Bezüglich der Dauer und der Energie der erzeugten Laserpulse gelang in allen drei spektralen Bereichen die Schaffung einzigartiger Werkzeuge für zukünftige Experimente der Ultrakurzzeitspektroskopie. Diese neuen Werkzeuge wurden für zeitaufgelöste Experimente genutzt, welche bisher nicht erreichte Einblicke in die Elektronendynamik auf einer Attosekundenzeitskala erlauben. Daher gliedert sich der Aufbau dieser Arbeit, welche die erreichten Fortschritte beschreibt, wie folgt:

- Nach einer allgemeinen Übersicht über die Attosekundenphysik in Kapitel 2 und eine Einführung in die theoretischen Grundlagen in Kapitel 3.1, welche in den folgenden Abschnitten von Bedeutung sein werden, wird in Kapitel 3.2 das Lasersystem vorgestellt, welches die Grundlage für alle weiteren Experimente war.

- Kapitel 4.1 konzentriert sich auf die Entwicklung eines neuartigen experimentellen Aufbaus für Anregungs-Abfrage-Experimente auf einer Attosekundenzeitskala: Das Attosekundenexperiment AS2. Das Fernziel dieses Aufbaus ist die Kombination von Experimenten mit isolierten Attosekundenlaserpulsen und intensiven Laserpulsen aus verschiedenen spektralen Bereichen. Erhebliche Entwicklungsarbeit wurde in die Erzeugung von neuartigen optischen Wellenformen investiert. Die Synthese von optischen Wellenformen bestehend aus einer fundamentalen Welle und deren zweiten Harmonischen wird in Kapitel 4.2 gezeigt. Die Erzeugung von hohen Harmonischen mit solchen Wellenformen führte zur Entdeckung einer Methode zur Synthese von spektral durchstimmbaren isolierten Attosekundenlaserpulsen, welche zukünftige Attosekundenexperimente enorm vereinfachen werden. Die kürzesten und energiereichsten Laserpulse, die jemals im tiefen ultravioletten Spektralbereich erzeugt wurden, werden in Kapitel 4.3 vorgestellt. Die erfolgreiche Entwicklung und Charakterisierung von neuen Optiken im extremen Ultraviolett eröffnet neue Wege in der Erzeugung von maßgeschneiderten Attosekundenpulsen mit bisher unerreichter Pulsenergie und Kontrolle der Phase der XUV-Pulse. Kapitel 4.4 beschreibt die erste vollständige Charakterisierung von phasenmodulierten XUV Mehrlagenspiegeln bezüglich ihrer Reflektivität und Phase. Kapitel 4.5 bezieht sich auf die Einführung von metallbeschichteten XUV-Spiegeln, welche die erreichbare XUV Pulsenergie bei der kürzesten jemals erreichten Attosekundenpulsdauer von nur 80 Attosekunden um zwei Größenordnungen am Ort des untersuchten Systems steigerte.

- Schließlich wurden einige bahnbrechende Experimente zu zeitaufgelösten Messungen der Elektronendynamik in Edelgasatomen durchgeführt. Diese erweitern unser

Abstract

Wissen über Prozesse auf einer Attosekundenzeitskala, welche bisher als instantan betrachtet wurden, und kulminierten in experimentellen Ergebnissen, die immer noch auf eine grundlegende theoretische Erklärung warten. Das Tunneln von Elektronen durch eine Potentialbarriere, welche von einem intensiven elektrischen Laserfeld und einem bindenden atomaren Potential gebildet wird, wurde auf einer Attosekundenzeitskala aufgelöst und ist in Kapitel 5.1 dargestellt. Die zeitliche Struktur des Photoemissionsprozesses, welcher bisher als instantan betrachtet wurde, wurde mit Hilfe der Attosekundenspektroskopie in Kapitel 5.2 offengelegt. Es wurde entdeckt, dass zwischen der Photoemission der 2s- und 2p-Elektronen in Neon eine messbare Verzögerung von 20 Attosekunden vorliegt. Dies ist die kürzeste Zeitdauer, die jemals direkt gemessen wurde. Dieses Ergebnis wird sicherlich weitere zukünftige Untersuchungen sowohl auf theoretischer als auch auf experimenteller Seite anregen.

This thesis is devoted to time-resolved measurements of the fastest phenomena to which science has currently access via direct measurements by means of attosecond laser pulses. Great effort has been invested in the construction of a novel experimental setup for the conduction of pump-probe experiments on an attosecond timescale, which have so far not been possible, accompanied by developments of sources of laser pulses in the near infrared, in the near ultraviolet and in the extreme ultraviolet. Success has been achieved in all three spectral ranges in the generation of unique tools in terms of the shortest pulse duration and pulse energy for future experiments in ultrashort spectroscopy. These new tools have been used for time-resolved experiments, which revealed unprecedented insights into electron dynamics on an attosecond timescale. Therefore, the structure of this thesis describing the achieved progress is as follows:

- After a general overview about attosecond physics in chapter 2 and an introduction into the theoretical basics in chapter 3.1, which will be relevant in the following chapters, chapter 3.2 will present the laser system on which all experiments based.

- Chapter 4.1 will concentrate on the development of a novel experimental setup for attosecond pump-probe experiments: the attosecond beamline AS2. The ultimate goal of this setup was the combination of isolated attosecond laser pulses with laser pulses from different spectral ranges. Substantial work has been invested in the generation of novel optical waveforms. The synthesis of optical waveforms consisting of a fundamental wave and its second harmonic are shown in chapter 4.2. High harmonic generation with these waveforms resulted in the discovery of a technique for the generation of tunable isolated attosecond pulses, which will enormously simplify future attosecond experiments. The shortest and most powerful laser pulses ever generated in the deep ultraviolet are presented in chapter 4.3. The successfull development and characterization of new optics in the extreme ultraviolet spectral range opens the door to the generation of tailored attosecond pulses with unprecedented on target pulse energy and control of the phase of the XUV pulses. Chapter 4.4 describes the first complete characterization of chirped XUV multilayer mirrors in terms of reflectance and phase, which allows for full control of the chirp of attosecond laser pulses in future experimnts. Chapter 4.5 deals with the invention of metal-coated XUV mirrors, which increased the available attosecond pulse energy on target by two orders of magnitude at a duration of 80 attoseconds, which is the shortest pulse duration ever achieved.

- Finally, several groundbreaking experiments have been conducted on time-resolved measurements of electron dynamics in noble gas atoms. They extend our knowledge about processes on the attosecond timescale, which have so far assumed to be instantaneous and culminated in experimental results that are still waiting for a theoretical explanation. The tunneling of electrons through a potential barrier formed by the electric field of an intense laser pulse and the atomic binding potential has been resolved on an attosecond timescale in chapter 5.1. A temporal structure of the photoemission process, which was so far been considered to happen instantaneously, was revealed by means of attosecond spectroscopy in chapter

5.2. It was discovered, that there is a measurable delay of 20 attoseconds between the photoemission of 2s and 2p electrons in neon. To date, this is the shortest directly measured time delay. In the nearby future, this result will certainly stimulate further investigations of this finding on both the theoretical and experimental side.

List of publications:

- A. L. Cavalieri, E. Goulielmakis, B. Horvath, W. Helml, M. Schultze, M. Fieß, V. Pervak, L. Veisz, V. S. Yakovlev, M. Uiberacker, A. Apolonski, F. Krausz and R. Kienberger. *Intense 1.5-cycle near infrared laser waveforms and their use for the generation of ultra-broadband soft-x-ray harmonic continua.* New Journal of Physics, **9**: 242 (2007).

- U. Graf, M. Fieß, M. Schultze, R. Kienberger, F. Krausz and E. Goulielmakis. *Intense few-cycle light pulses in the deep ultraviolet.* Optics Express, **16**: 23, 18956-18963 (2008).

- M. Schultze, M. Fieß, N. Karpowicz, J. Gagnon, M. Korbman, M. Hofstetter, S. Neppl, A. Cavalieri, Y. Komninos, Th. Mercouris, C. A. Nicolaides, R. Pazourek, S. Nagele, J. Feist, J. Burgdörfer, A. M. Azzeer, R. Ernstorfer, R. Kienberger, U. Kleineberg, E. Goulielmakis, F. Krausz and V. S. Yakovlev. *Delay in Photoemission.* Science, *accepted.*

- M. Hofstetter, M. Schultze, M. Fieß, B. Dennhardt, J. Gagnon, E. Goulielmakis, R. Kienberger, E. M. Gullikson, F. Krausz and U. Kleineberg. *Quantitative phase control of attosecond XUV pulses using multilayer mirrors. In preparation.*

- M. Fieß, M. Schultze, E. Goulielmakis, B. Dennhardt, M. Hofstetter, R. Kienberger and F. Krausz. *Versatile apparatus for attosecond metrology and spectroscopy. Submitted.*

- M. Fieß, B. Horvath, T. Wittmann, W. Helml, Y. Cheng, B. Zeng, Z. Xu, A. Scrinzi, J. Gagnon, F. Krausz and R. Kienberger *Tunable XUV continua between 80 and 100 eV. In preparation.*

2 Introduction

Shortly after the invention of the ruby laser by Theodore Maiman in 1960 [1] the first pulsed laser systems have been invented in the picosecond regime [2], which started the race for ever shorter laser pulses as a unique tool for time-resolved measurements of ultrashort processes. The timescale, on which ultrashort processes evolve, is generally determined by the discrete excitation energies of the system under scrutiny. This relationship is dictated by one of the most fundamental laws of quantum mechanics: the energy-time-uncertainty principle, which connects the duration of a time interval Δt during which a transition between two quantum states, that are separated by a energetic gap ΔE, takes place [3]:

$$\Delta t \Delta E \approx \frac{h}{2\pi},$$

Here, h is Planck's constant. An excellent example for this general rule are molecules: The energetic distance between the quantized rotational states in molecules is in the order of a few wavenumbers (8066 cm^{-1} = 1 eV). From this follows that rotational dynamics in molecules evolve on a picosecond timescale and can be excited with photons in the microwave regime. Vibrations between atoms, which are connected by a molecular bond, take place on a femtosecond timescale and can be triggered by photons of the infrared spectrum. Electronic transitions in molecules as well as in atoms [4] and solids [5] exhibit excitation energies in the order of several electron volts and occur on an attosecond timescale. After the breakthrough to the generation of isolated attosecond laser pulses in 2001 [6] this is to date the fastest timescale, to which science has access via direct temporal measurements. Following this line of argument the next even faster timescale encountered by science will be the zeptosecond timescale. The necessary transition energies will be in the order of many thousands of eV and are typical for energetic transitions in atomic nuclei.

A fundamental limitation for the generation of ever shorter laser pulses is the wavelength of the electric field carrier wave since the laser pulse duration cannot not be substantially shorter than one period of the carrier wave as depicted in Fig. 1.

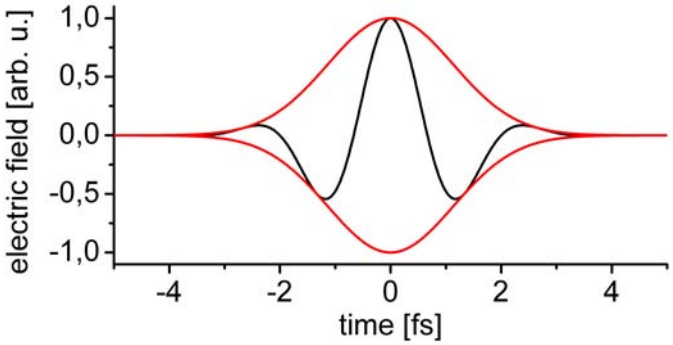

Fig. 1: Carrier electric field wave (black line) and envelope (red line) of a single cycle laser pulse (FWHM) with a central wavelength of 800 nm.

Therefore, femtosecond science starts in the near infrared and ends in the near ultraviolet of the electromagnetic spectrum, where one oscillation cycle lasts about 1 fs. Consequently, attosecond physics starts in the near ultraviolet range and ends to date in the extreme ultraviolet at a pulse duration of 80 attoseconds, which is so far the shortest pulse duration of an isolated laser pulse ever generated [7]. For this reason, approaching substantially shorter pulse durations will inevitably be accompanied by a shift of the laser spectrum towards the X-ray and later on γ-ray regime. These rather trivial insights come along with some absolutely nontrivial technological challenges concerning the generation of ultrashort laser pulses with ever shorter pulse durations and unavoidably ever higher photon energies, which are also subject of this thesis. A few of them shall be mentioned in the following:

- Absorption of radiation by air: For radiation with wavelengths below 200 nm absorption by oxygen and at slightly shorter wavelengths also by nitrogen as natural components of air sets in. Therefore, for a long time this spectral range has been neglected by science for the simple practical reason that experiments with such high energetic photons require vacuum conditions making experiments more expensive and complicated. The design of vacuum chambers, pumping schemes and a great number of motorized optics, which are installed in vaccum and have to be controllable during the experiment from outside, was one of the major tasks also in this work.

- The availability of optics: in the near infrared, visible and near ultraviolet range of the electromagnetic spectrum all kinds of reflective, birefringent and beamsplitting optics are obtainable, most of which have been improved during more than 100 years. However, for radiation with wavelengths below 200 nm this situation

changes dramatically for several reasons: first, science in the spectral range of extreme ultraviolet and higher photon energies is comparably young, the development of powerful optics as available for lower photon energies therefore topic of ongoing research. Second, materials that exhibit a high reflectance at small angles of incidence (AOI) do not exist, whereas the AOI is measured between the material surface normal and the propagation direction of the incident light. Therefore, reflective optics in the XUV are limited to gracing incidence optics and multilayer mirrors, that can be fabricated in a few spectral windows of the extreme ultraviolet spectrum.

- The availability of lasing media: the classical picture of a laser is a lasing medium between two mirrors, in which a population inversion is generated by an external energy source. **L**ight **A**mplification by **S**timulated **E**mission of **R**adiation is by definition a condition for the operability of a laser system, i.e. spontaneous emission may not be stronger than stimulated emission. Already Einstein showed that the ratio between spontaneous and induced emission scales with the third power of the photon energy [8]. For this reason the development of laser systems at ever higher photon energies becomes more and more difficult. Therefore, attosecond laser pulses in the XUV spectral range are currently only accessible via high harmonic generation (HHG) with powerful laser pulses in the near infrared and visible spectral range. Unfortunately, the typical conversion efficiency in such HHG processes at repetition rates of a few kHz is around 10^{-6} resulting in extremely low XUV pulse energies in the pJ range.

So far, only a very small number of experiments revealing dynamics on an attosecond timescale have been done, most of them in noble gases [4] or solids [5]. The measurement of attosecond dynamics in molecules beyond H_2 like e.g. larger biomolecules, which are of great importance in daily life, has not suceeded yet. These first measurements will unfold the electron dynamics in molecules, which are the first step in the formation and break of chemical bonds between atoms, and therefore allow deeper insights in one of the most fundamental processes in chemisty, biology and physics. Of course, the theoretical description of electron dynamics in molecules is much more difficult compared to the one in isolated atomic systems like noble gases. However, this is exactly what makes these experiments attractive. Attosecond spectroscopy with molecules will by no means be limited to valence electron dynamics. In close analogy to the Mössbauer effect [9], which reveals a dependence of the energy states of atomic nuclei on the type of chemical bond the surrounding electron shells form with neighboring atoms, the dynamics of inner shell electrons will be affected by chemical bonds formed by the surrounding valence electrons, too.

Preparing the experimental conditions for attosecond experiments with molecules on such a level was one task of this thesis. The unique tool, which has been developed for such an experiment, is an attosecond beamline that allows simultaneous measurements of

- ion mass spectra for the detection of charged molecular fragments generated during

the break of chemical bonds in a molecule,

- photoelectron spectra for the detection of the evolution of the electronic states in molecules after their electronic excitation,
- and transient XUV absorption spectra, which complement the detection of electron dynamics via photoelectron spectra measurements.

The generation of laser pulses covering the spectral range from the near infrared up to the extreme ultraviolet spectral range has been developed for pump-probe-experiments with molecules:

- attosecond XUV laser pulses with unprecedented pulse energies at kHz repetition rate.
- powerful fundamental laser pulses covering the near infrared and visible spectral range as driving laser pulses [10].
- powerful ultrashort laser pulses in the deep ultraviolet as a prerequisite for the electronic excitation of smaller molecules [11].
- synthesized ω+2ω waveforms for an electronic excitation of target systems depending on a tailored optical waveform.

To date, the availabilty of these tools in one and the same experimental setup is unique and opens the door to a great number of experiments, which have not been accessible in the past.

3 Basic physics and technologies

3.1 Theory

3.1.1 Harmonic generation with intense laser fields

For nonmagnetic materials that contain no free charges and no free currents the 1-dim. wave equation of optics can be derived from Maxwell's equations [12, 13]:

$$\frac{\partial^2 \mathscr{E}}{\partial z^2} - \frac{1}{c_0^2}\frac{\partial^2 \mathscr{E}}{\partial t^2} = \mu_0 \frac{\partial^2 \mathscr{P}}{\partial t^2}$$

This equation has the form of a driven wave equation for the electric field $\mathscr{E}$. The polarization $\mathscr{P}$ of the material acts as a source term on the right-hand side of this equation. In absence of resonances and in case of electric field strengths $\mathscr{E}$ that are much smaller than typical atomic field strengths the nonlinear response $\mathscr{P}$ of the polarization on the incident electric field $\mathscr{E}$ can be described by the following power series:

$$\mathscr{P} = \varepsilon_0 \left[\chi^{(1)}\mathscr{E} + \chi^{(2)}\mathscr{E}^2 + \chi^{(3)}\mathscr{E}^3 + \ldots\right] \tag{1}$$

The $(n+1)^{st}$ order tensors $\chi^{(n)}$ are known as the n^{th}-order optical susceptibilities. In this thesis, only the second- and third-order susceptibilities are of importance. They cause the generation of various nonlinear effects, which will be examined in the following.

In case of the superposition of two electric field waves

$$\mathscr{E}(\vec{r},t) = \frac{1}{2}E_1(\vec{r},t)\exp\left[i(\omega_1 t - \vec{k}_1\cdot\vec{r})\right] + \frac{1}{2}E_2(\vec{r},t)\exp\left[i(\omega_2 t - \vec{k}_2\cdot\vec{r})\right] + c.c.$$

with frequencies ω_1, ω_2 and wave vectors $\vec{k}_1$, $\vec{k}_2$, the second order nonlinear material response is determined by

$$\begin{aligned}\mathscr{E}^2(\vec{r},t) =& \frac{1}{2}E_1E_1^* + \frac{1}{2}E_2E_2^* \\ &+ \frac{1}{4}E_1^2\exp\left[2i(\omega_1 t - \vec{k}_1\cdot\vec{r})\right] + \frac{1}{4}(E_2^*)^2\exp\left[2i(\omega_2 t - \vec{k}_2\cdot\vec{r})\right] \\ &+ \frac{1}{2}E_1E_2\exp\left\{i\left[(\omega_1+\omega_2)t - (\vec{k}_1+\vec{k}_2)\cdot\vec{r}\right]\right\} \\ &+ \frac{1}{2}E_1E_2^*\exp\left\{i\left[(\omega_1-\omega_2)t - (\vec{k}_1-\vec{k}_2)\cdot\vec{r}\right]\right\} \\ &+ c.c.\end{aligned}$$

The first line describes a static electric field in the material known as optical rectification. The second line describes the second harmonic generation (SHG) of the fundamental waves. The third and fourth line describe the sum frequency generation (SFG) and the difference frequency generation (DFG) of the fundamental waves. The efficiency of all

these nonlinear processes is proportional to the second order susceptibility $\chi^{(2)}$.

Third order nonlinear effects, which are proportional to the third order susceptibility $\chi^{(3)}$ and generally called four-wave-mixing processes, are orders of magnitude less efficient than second order nonlinear effects. Instead of listing the complete third order nonlinear polarization of the real electric field

$$\begin{aligned}\mathscr{E}(\vec{r},t) =& \frac{1}{2}E_1(\vec{r},t)\exp\left[i(\omega_1 t - \vec{k}_1\cdot\vec{r})\right] \\ &+ \frac{1}{2}E_2(\vec{r},t)\exp\left[i(\omega_2 t - \vec{k}_2\cdot\vec{r})\right] \\ &+ \frac{1}{2}E_2(\vec{r},t)\exp\left[i(\omega_2 t - \vec{k}_2\cdot\vec{r})\right] + c.c.\end{aligned}$$

only two terms, which matter in the subsequent chapters, shall be mentioned:

$$\begin{aligned}\mathscr{P}_{THG} =& \frac{1}{8}\varepsilon_0\chi^{(3)}E_1|E_1|^2\exp\left\{3i\left[\omega_1 t - \vec{k}_1\cdot\vec{r}\right]\right\} + c.c. \\ \mathscr{P}_{SD} =& \frac{3}{4}\varepsilon_0\chi^{(3)}E_1^2E_2^*\exp\left\{i\left[(2\omega_1-\omega_2)t - (2\vec{k}_1-\vec{k}_2)\cdot\vec{r}\right]\right\} + c.c.\end{aligned}$$

$\mathscr{P}_{THG}$ describes the third harmonic generation (THG) of the fundamental wave with frequency ω_1. $\mathscr{P}_{SD}$ describes the self diffraction (SD) of the fundamental waves at an induced grating in the nonlinear medium. Fig. 2 illustrates the intensity pattern of two interfering laser pulses.

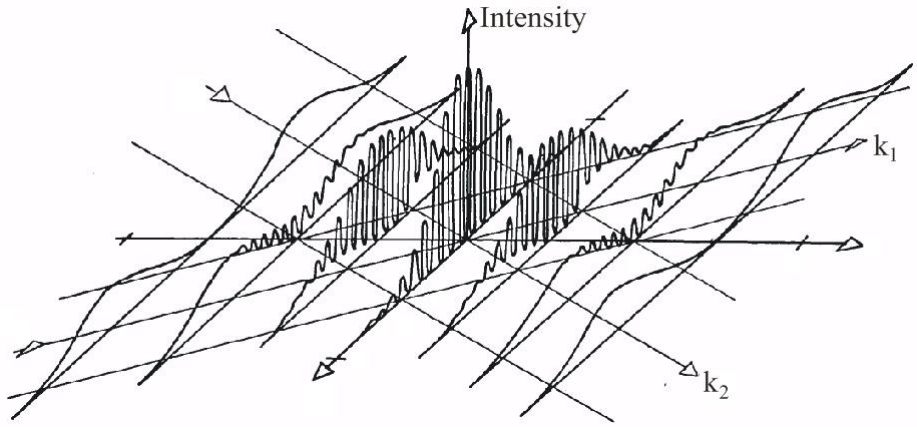

Fig. 2: Intensity pattern of two interfering laser pulses in a nonlinear medium [14].

In case of high intensities this pattern results in a modulation of the refractive index, i.e. an induced phase grating, caused by the nonlinear Kerr effect:

$$n = n_0 + In_2$$

Nonlinear phenomena caused by electric field intensities above approximately 10^{12} W/cm^2 cannot be described any more by means of perturbative theories since in this intensity regime different kinds of ionization processes start to occur. The following examination considers only nonlinear processes caused by laser intensities between 10^{12} W/cm^2 and 10^{15} W/cm^2, which are relevant for the experiments presented in the next chapters.

The main difference between high harmonic generation and low order harmonic generation in the perturbative regime is that the electric field strength of the laser field becomes comparable to the binding electric field strength of electrons in matter. The binding potential of an electron e.g. in a noble gas atom is substantially deformed by the electric field of the laser. Ionization sets in caused by electron tunneling of the bound electrons through a potential barrier formed by a superposition of the external laser field and the atomic binding potential as shown in Fig. 3 a):

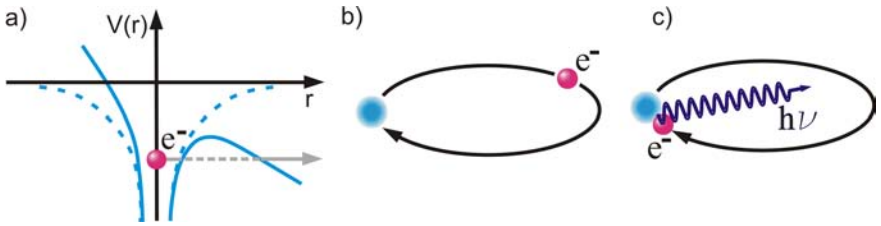

Fig. 3: a) atomic binding potential in absence of an external laser field (blue dashed line) and formation of a potential barrier through which electron tunneling takes place (blue straight line), b) acceleration of the freed electron in the external laser electric field, c) recombination and emission of a photon.

Besides electron tunneling through a potential barrier formed by the external laser field and the atomic binding potential there exist other nonlinear processes leading to ionization in intense laser fields [15, 16]. The most important one is multi-photon-ionization (MPI), which sets in at lower intensities than tunneling ionization. MPI was first regarded as a generalization of the photoeffect with the main difference that instead of one single high energetic photon several photons with lower energy are used to overcome the ionization barrier [17]. Therefore, the photoelectron kinetic energy E_{kin} is given by:

$$E_{kin} = I_p - nh\nu$$

whereas n is the minimum number of photons necessary to overcome the ionization potential I_p. This concept had to be revised after the observation of photoelectrons with even higher kinetic energies

$$E_{kin} = I_p - (n+s)h\nu$$

whereas n is again the minimum number of photons to overcome the ionization potential I_p and s is the number of excess photons absorbed by the photoelectron during the ionization process [18, 19]. In the following chapters of this thesis such high energetic photoelectrons generated by MPI appear in streaking experiments, in which they play the role of a strong but unwanted background signal at lower photoelectron energies.

Ionization in strong laser fields via electron tunneling has been first theoretically described by the theory of Keldysh [20] and an improved theory of Ammosov, Delone and Krainov [21]. Keldysh introduced the dimensionless parameter

$$\gamma = \sqrt{2mI_p}\frac{\omega}{eE},$$

which allows an estimation on wether MPI or electron tunneling is the dominant ionization process in laser fields. m is the electron mass, e the electron charge, ω the laser field angular frequency, E the electric field amplitude and I_p the ionization potential. For a constant laser wavelength follows from $\gamma > 1$, i.e. at low intensities, that MPI dominates the ionization process whereas for $\gamma < 1$, i.e. at high intensities, electron tunneling dominates.

Once the electron has tunneled through the potential barrier, it can be treated as a free classical electron [22] or as a quantum mechanical electron wave packet [23], which is acceralerated by the external electric laser field. First, the released electron is pulled away from the remaining ion, but at the latest after one half-cycle of the electric laser field the sign of the accelerating electric field changes and the electron is pushed back towards the ion. With a rather small but non-negligible probability the back-accelerated electron recombines with the ion and emits the ionization energy plus the kinetic energy, which it acquired during its acceleration in the external laser field, as a high energy photon. A classical calculation [22] of the maximum kinetic energy of the recombining electron results in a so-called cut-off photon energy of

$$E_{cutt-off} = I_p + 3.17U_p$$

where I_p decribes the ionization potential and

$$U_p = \frac{e^2E^2}{4m\omega^2}$$

the ponderomotive energy. e is the electron charge, E the laser electric field amplitude, m the electron mass and ω the laser field angular frequency. An essential finding of these calculations is that the maximum photon energy $E_{cutt-off}$ scales linearly with the laser field intensity but quadratically with its wavelength λ. This motivated intensive efforts in the development of few-cycle laser pulses in the IR for high harmonic generation in order to reach higher XUV photon energies [24]. Unfortunately, the recombination probability

and therefore the HHG efficiency scales with $\lambda^{-5.5\pm0.5}$ [25]. This can be qualitatively explained in the quantum mechanical picture with the stronger spread of the electron wave packet due to the much longer electron trajectories in case of HHG with longer electric field wavelengths:
The group velocities in vacuum for photons and electrons derived from the corresponding dispersion relations reveal that in contrast to photon wavepackets electron wavepackets are dispersed by vacuum:

$$E = \frac{p^2}{2m} \Leftrightarrow \hbar\omega = \frac{\hbar^2 k^2}{2m} \Rightarrow \frac{\partial\omega}{\partial k} = \frac{\hbar k}{m} \propto k \tag{2}$$

$$\omega = ck \Rightarrow \frac{\partial\omega}{\partial k} = c = const. \tag{3}$$

Here, E describes the classical kinetic energy, p the classical momentum, m is the electron mass and k the wavenumber. From eq. (2) follows that the group velocity of electron wavepackets in vacuum depends on the electron momentum, i.e. vacuum is dispersive for electron wavepackets. For photons, however, follows from eq. (3) that the group velocity is independent from the photon momentum. Therefore laser pulses are not dispersed by vacuum. The same argument applies to the HHG generation efficiency with short and long trajectories, which is illustrated in Fig. 4.
Tunneling ionization is possible as soon as the laser intensity is high enough. At even higher intensities bound electrons can overcome the potential barrier before the electric field oscillations have reached its maxima or minima. Electrons, which are released before these extrema, recombine later and propagate along longer trajectories than electrons, which are released after the extrema. In terms of the dispersion of the emitted XUV pulses of each half cycle this has far-reaching consequenses: Long-trajectory electrons experience two zero crossings of the driving electric field. After the second zero crossing they are decelerated on their way back to the ion and, therefore, loose kinetic energy. That's why long-trajectory XUV pulses reveal negative chirp in contrast to short-trajectory pulses, which reveal positive chirp [26]. In practice HHG is only possible by focusing the driver laser pulses into a nonlinear target. The phase-matching conditions set by the position of the nonlinear target relative to the focus dictate the preferred generation of either long or short trajectory high harmonics [27]. Since the recombination probability in case of longer trajectories is substantially reduced, HHG is usually optimized for short-trajectory photons. Therefore, attosecond laser pulses with highest possible photon flux carry positive chirp [28]. Compensation of this chirp can be reached by introducing additional negative chirp after HHG. This is usually done by means of thin metal foils, which are anyway necessary for a subsequent spectral filtering of the generated high harmonic spectrum after HHG.

As already mentioned and shown in Fig. 4 for one half-cycle, the generation of an attosecond laser pulse occurs during each half-cycle of the fundamental carrier wave. Without any further measures this results in the generation of a train of attosecond laser pulses, which corresponds to a modulated spectrum in the spectral domain. In the last 10 years

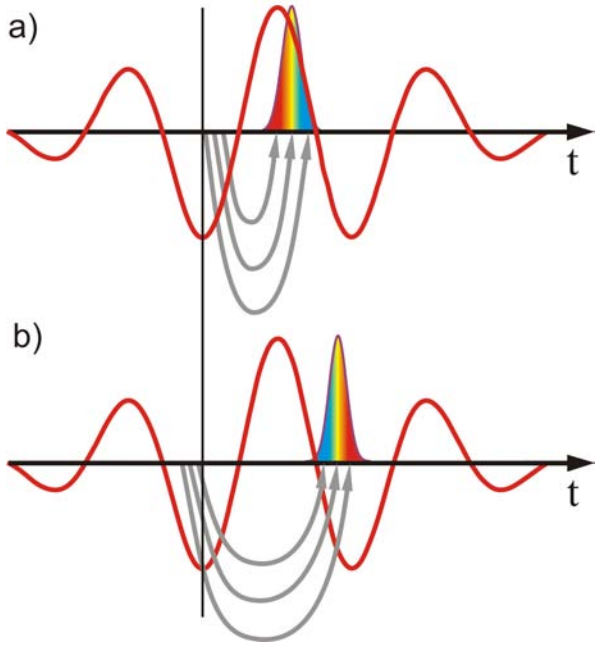

Fig. 4: a) HHG with short trajectories resulting in XUV pulses with positive chirp, b) HHG with long trajectories resulting in XUV pulses with negative chirp. The red curve indicates the electric field of the fundamental laser pulse. The sign of the electric field changes only one time in the case of short trajectories and two times in the case of long trajectories resulting in chirp with opposite sign for HHG with long trajectories.

different concepts have been pursued for the isolation of one single attosecond pulse of such a train of attosecond pulses. All these concepts have in common that they aim for the isolation of a continuous XUV spectrum as the spectral manifestation of an isolated attosecond laser pulse in the time domain. This means that either HHG of all but one half-cycle has to be suppressed or specific high harmonics, which are generated only during one half-cycle, are separated from all other generated high harmonics.

The intensity-gating method requires femtosecond pulse durations of less than 5 fs. It exploits the fact that in case of such short pulse durations only one half-cycle contributes to the cut-off of the generated XUV spectrum. This is depicted in Fig. 5 for the case of short-trajectory HHG:

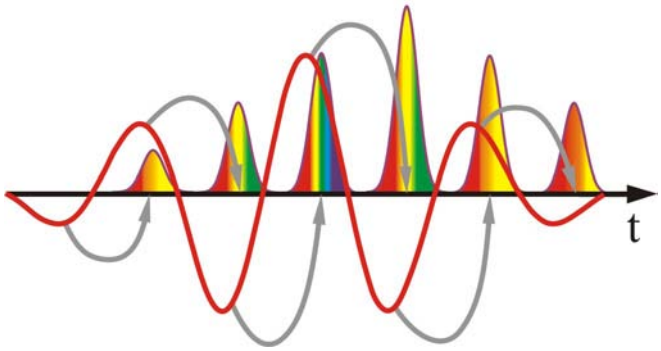

Fig. 5: HHG with few-cycle femtosecond laser pulses: only one half-cycle contributes to the highest photon energies. The gray arrows denote the emission time and recollision time of the electrons. The hight of the XUV peaks denotes the tunneling probability at the emission times.

Spectral filtering of the continuous cut-off of the generated high harmonic spectrum with thin metal filters as shown in Fig. 6 guarantees the isolation of photons, which are generated only during one half-cycle. This method has been applied in this work since it provides the highest possible XUV photon energies and the highest possible XUV photon flux [7]. However, the generation of sub-5-fs driver laser pulses still remains technically challenging.

The polarization-gating method is based on the required linear polarization of the driver electric field for high harmonic generation. The advantage of this technique is, that it works with slightly longer driver pulse durations of about 7 fs. In the general case of elliptic polarization the freed electrons have no chance to recombine since their trajectories do not drive the electrons back to the ion from which they have been emitted. The superposition of two circularly polarized and delayed driver fields with opposite rotation direction assures that only during one half-cycle linearly polarized light occurs and therefore only one single attosecond laser pulse is generated [30, 31]. The drawback of this method is that only a fraction of the fundamental pulse energy is used for high harmonic generation resulting in a substantial reduction of both the achievable maximum photon energy and photon flux.

The third concept for the generation of a continuous high harmonic spectrum, which has also been used in this work, is based on the superposition of the fundamental driver wave with a fraction of its second harmonic wave in order to increase the peak contrast between the main peak of the carrier electric field and the next two adjacent peaks. From

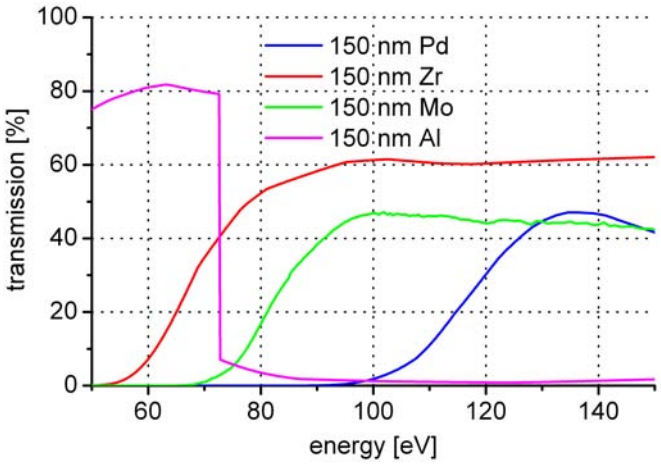

Fig. 6: Transmission curves of thin metal filters, which have been used in this thesis for spectral filtering of XUV spectra [29].

such an increased peak contrast follows that a larger spectral range of XUV photons with highest energy is generated only during one half-cycle of the synthesized $\omega+2\omega$ waveform.

Fig. 7 illustrates this idea in an idealized form:

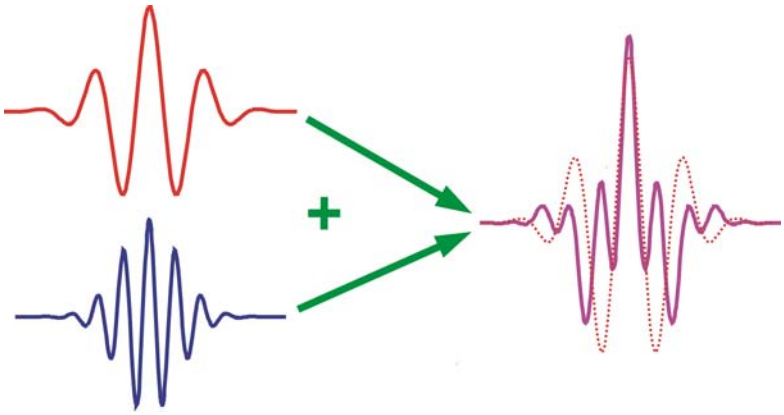

Fig. 7: Superposition of the fundamental wave with its second harmonic wave for increasing the peak contrast between the main peak and the next two adjacent peaks.

A fundamental prerequisite for all three methods is the capability of controling the driver waveform by means of carrier-envelope-phase stabilization. Without full control over the driver waveform the reproducible generation of isolated attosecond laser pulses is impossible.

3.1.2 Attosecond streaking experiments

A fundamental challenge in the generation of ultrashort laser pulses is the precise measurement of their pulse duration. The basic prinicple behind the measurement of a short event in the time domain is, that one needs an even shorter event as a reliable reference for a precise temporal characterization. At the latest when the femtosecond time domain was reached in the 1980ies such even shorter references did simply not exist anymore since the temporal resolution of the so far used electronic detection techniques is limited to the picosecond time domain. From that time on nonlinear processes had to be invented, which use the temporal resolution of ultrashort laser pulses itself as the necessary reference for their temporal characterization. Autocorrelation techniques in case of two identical laser pulses and crosscorrelation techniques in case of two different laser pulses using all available nonlinear processes, like second harmonic generation [32], third harmonic generation, two photon absorption, etc. have been developed for the generation and temporal characterization of ever shorter laser pulses. Unfortunately the mentioned self-referencing techniques suffer from the fact that the reference can only be as short as the event to be measured but not shorter, which would be necessary for a precise temporal characterization. The consequence is the need for an assumed or sometimes rather postulated temporal pulse shape, which eventually has a considerable influence on the value of the resulting pulse duration [33].

This issue was solved by the invention of "frequency resolved optical gating" (FROG) [34,35], which is in principle nothing more than a spectrally resolved autocorrelation, and "spectral phase interferometry for direct electric field reconstruction" (SPIDER) [36]. These methods make use of the spectral domain instead of the time domain that has been used by the so far developed nonlinear correlation techniques. Iterative algorithms in case of FROG and a direct analysis in case of SPIDER enabled for the first time the unambiguous and precise characterisation of ultrashort laser pulses in terms of electric field amplitude and phase by means of a self-referencing technique. A severe drawback of these powerful methods for ultrashort laser pulse characterization is the increased complexity of their experimental realization and data analysis. Whereas nowadays simple second order autocorrelation measurements in the femtosecond domain can be done within seconds, FROG and SPIDER require time consuming measurements in the spectral domain. Furthermore, the result of the analysis of the acquired data critically depends on the data quality and therefore on a rather complicated alignment of the experimental setup.

During the last 10 years the technology, which has been developed for the temporal characterization of femtosecond laser pulses, has been transfered to attosecond physics. The routine application of autocorrelation measurements has so far been prevented by the low pulse energies of isolated attosecond laser pulses and the lack of efficient nonlinear processes in the extreme ultraviolet [37]. Therefore, the state-of-the-art technique for the characterization of attosecond pulses is called "streaking", which was proposed by Itatani et al. [38] and combines the concept of the conventional electronic streak camera [39], the concept of a cross correlation measurement and the FROG-method [40] to a powerful

tool offering access to the electric field amplitude and phase of attosecond laser pulses [41].

Attosecond streaking experiments described in this work are realized as crosscorrelations between an attosecond laser pulse in the extreme ultraviolet (XUV) and a few-cycle femtosecond laser pulse in the near infrared (NIR). The measured physical quantity is the kinetic energy of photoelectrons, which are released by the attosecond XUV-pulse and which is modulated by the electric field of the few-cycle femtosecond pulse. The photoelectron spectra are usually acquired by photoelectron time-of-flight spectrometers, which translate the classic kinetic energy

$$E = \frac{1}{2}mv^2$$

of the photoelectrons with mass m into a flight time t over a certain flight distance s. Micro-channel-plate (MCP) detectors generate a voltage peak when a photoelectron reaches the detector. The voltage peaks generated by the impinging photoelectrons are detected by an electronic readout card. The temporal resolution of the readout card and the flight distance determine the energy resolution of the time-of-flight spectrometer. The conversion of the measured quantity of photoelectron counts $n_t(t)$ per flight time t to photoelectron counts $n_E(E)$ per kinetic energy E results from the conservation of the total number of photoelectrons:

$$\int_{t=0}^{+\infty} n_t(t)dt = \int_{E=+\infty}^{0} n_E(E)dE \Leftrightarrow n_E\left(\frac{m}{2}\left(\frac{s}{t}\right)^2\right) = n_t(t)\frac{t^3}{ms^2} \text{ with } dE = -\frac{ms^2}{t^3}dt$$

A streaking measurement consists of a series of photoelectron spectra acquired by temporally scanning the attosecond pulse through the much longer femtosecond pulse. In absence of the electric field of the fundamental laser pulse the kinetic energy E of the photoelectrons generated by the XUV attosecond pulse is determined by the ionization potential I_p of the utilized gas medium and the photon energy $h\nu$ of the XUV pulse:

$$E = h\nu - I_p$$

In presence of the electric field of the femtosecond laser pulse the momentum $p(t)$ of the generated photoelectrons with respect to the delay time t between the femtosecond pulse and the attosecond pulse is given according to Newton's 2nd law of motion by [42]:

$$\begin{aligned}
\frac{\partial p}{\partial t} &= -e\,E(t) \\
\Leftrightarrow p(t) &= p(t_0) - e\int_{t_0}^{t} E(t')dt' \\
&= p(t_0) + e\int_{t_0}^{t} \frac{\partial A(t')}{\partial t'}dt' \\
&= p(t_0) + e\,[A(t) - A(t_0)]
\end{aligned}$$

whereas the photoelectrons are released by the attosecond pulse at delay time t_0 and $A(t)$ is the vector potential of the electric field. $A(t)$ can be set to zero since already a few femtoseconds after the emission time t_0 the fundamental electric field $E(t)$ is zero. With this follows for the measured kinetic energy:

$$E(t) = \frac{p^2(t)}{2m} = \frac{1}{2m}\left[p^2(t_0) - 2ep(t_0)A(t_0) + e^2A^2(t_0)\right] \tag{4}$$

In case of fundamental intensities of about $1 \cdot 10^{13}$ W/cm^2, which are usually used for streaking experiments, the term $e^2A^2(t_0)$ is much smaller than the term $2ep(t_0)A(t_0)$ in eq. 4. Therefore streaking measurements offer a direct access to the the electric field of the femtosecond laser pulse by a simple derivation of the measured streaking curve with respect to the delay time t between the attosecond pulse and the femtosecond pulse. Interestingly, the streaking amplitude increases with increasing initial momentum p_0. Many times this was also experimentally observed during this work, e.g. in streaking scan 64 on page 91. In general, shorter attosecond pulses require a broader XUV-spectrum. Therefore, an increased temporal resolution in a streaking scan is compromised by a reduced spectral resolution since the spectral bandwidth of the XUV-spectrum is translated into the spectral bandwidth of the generated photoelectron spectrum.

In principle, a streaking measurement is not more than a spectrally resolved cross correlation measurement between the fundamental laser pulse and the attosecond laser pulse and at this point FROG comes into play, since a variation of FROG, which is called XFROG [43], can also be applied to crosscorrelation measurements. In fact, by means of an iterative algorithm it is possible to retrieve the electric field in amplitude and phase for both the fundamental pulse and the attosecond pulse [40]. The only information, which is not accessible via FROG, is the CEP of the XUV pulse.

In order to gain some qualitative information about the chirp of the attosecond pulses a time-consuming FROG retrieval of the acquired data is not necessary. There exist some characteristic features of streaking scans, which unambiguously identify the sign of a potential chirp of the attosecond laser pulse, that are discussed in the following.

Fig. 8 illustrates two different cases of streaking with chirped attosecond XUV pulses:

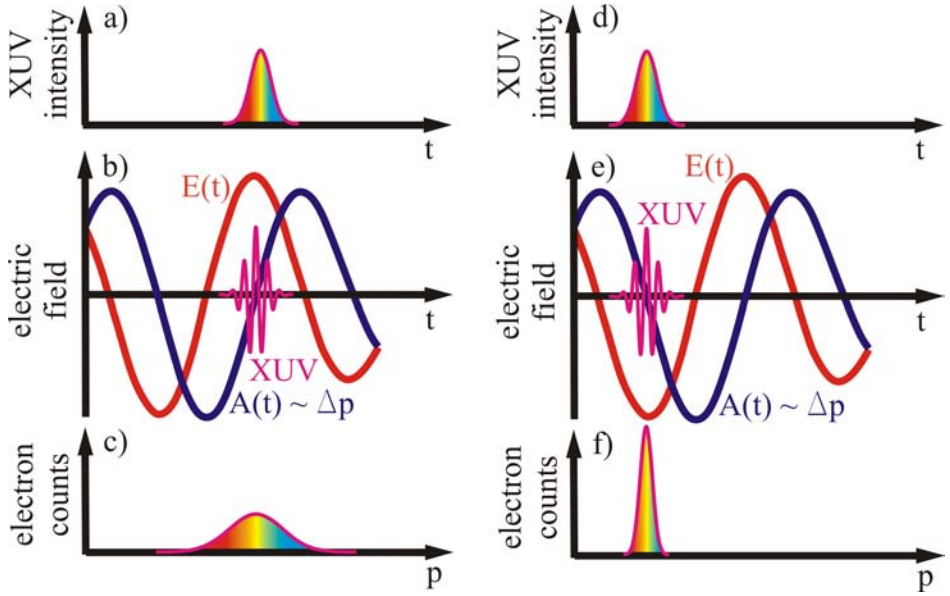

Fig. 8: a) and d): temporal profile of the XUV intensity, chirp is indicated by colors, b) and e): streaking with positive and negative slope of the vector potential $A(t)$, c) and f): photoelectron spectra with different spectral bandwidth and peak count rate caused by the vector potential $A(t)$.

In absence of the electric field of a NIR laser pulse the generated photoelectron spectrum is just a copy of the chirped XUV photon spectrum shifted by the ionization energy I_p of the ionized material. In case of positive chirp of the XUV pulse photoelectrons with less kinetic energy would be emitted earlier by the preceeding red-shifted XUV photons and photoelectrons with higher kinetic energy would be emitted later by the trailing blue-shifted XUV photons. In presence of the fundamental electric field this situation changes. The momentum change Δp of the photoelectrons is given by the vector potential $A(t)$. If the emitted photoelectron spectrum coincides with a zero crossing of the vector potential with positive slope, then the blue-shifted later photoelectrons gain even more energy and the red-shifted earlier photons loose even more kinetic energy. Therefore, the measured photoelectron spectrum is artificially broadened by the momentum change caused by the fundamental electric field whereas the maximum photoelectron count rate is reduced. In case of a zero crossing of the vector potential with negative slope the opposite is the case: blue-shifted later photoelectrons are red-shifted and red-shifted earlier photoelectrons are blue-shifted resulting in a narrower photoelectron spectrum and increased maximum count rate.

3.1.3 Dispersion

The topics, which are addressed in this section, will be of great importance in chapter 4.2 for the calculation of the optical components for the synthesis of waveforms consisting of the fundamental wave and its second harmonic. Furthermore, the concept of the carrier-envelope-phase (CEP) is introduced, which is crucial especially in chapter 3.2 for the active CEP stabilization.

The change of the spectral phase $\Delta\varphi(\lambda)$ of a laser pulse, which is propagating through a material of length l and refractive index $n(\lambda)$ is given by:

$$\Delta\varphi(\lambda) = 2\pi l \frac{n(\lambda)}{\lambda}$$

The absolute spectral phase $\varphi(\omega)$ of a laser pulse can be described by a Taylor-expansion:

$$\begin{aligned}\varphi(\omega) = \varphi(\omega_0) + \left(\frac{d\varphi}{d\omega}\right)\Bigg|_{\omega=\omega_0}(\omega-\omega_0) + \frac{1}{2}\left(\frac{d^2\varphi}{d\omega^2}\right)\Bigg|_{\omega=\omega_0}(\omega-\omega_0)^2 \\ + \frac{1}{6}\left(\frac{d^3\varphi}{d\omega^3}\right)\Bigg|_{\omega=\omega_0}(\omega-\omega_0)^3 + \frac{1}{24}\left(\frac{d^4\varphi}{d\omega^4}\right)\Bigg|_{\omega=\omega_0}(\omega-\omega_0)^4 + \dots\end{aligned}$$

With the relation

$$\frac{d}{d\omega} = -\frac{\lambda^2}{2\pi c}\frac{d}{d\lambda}$$

follows for the corresponding expansion coefficients [44]:

$$\begin{aligned}\varphi_1 &= \frac{d\varphi}{d\omega} = \frac{\lambda^2 l}{c}\left[\frac{n(\lambda)}{\lambda^2} - \frac{1}{\lambda}\frac{dn(\lambda)}{d\lambda}\right] \\ \varphi_2 &= \frac{d^2\varphi}{d\omega^2} = \frac{\lambda^3 l}{2\pi c^2}\frac{d^2n(\lambda)}{d\lambda^2} \\ \varphi_3 &= \frac{d^3\varphi}{d\omega^3} = -\frac{\lambda^4 l}{4\pi^2 c^3}\left[3\frac{d^2n(\lambda)}{d\lambda^2} + \lambda\frac{d^3n(\lambda)}{d\lambda^3}\right] \\ \varphi_4 &= \frac{d^4\varphi}{d\omega^4} = \frac{\lambda^5 l}{\pi^3 c^4}\left[\frac{3}{2}\frac{d^2n(\lambda)}{d\lambda^2} + \lambda\frac{d^3n(\lambda)}{d\lambda^3} + \frac{\lambda^2}{8}\frac{d^4n(\lambda)}{d\lambda^4}\right]\end{aligned}$$

φ_1, which describes the linear change of the spectral phase, is related to the group velocity v_g:

$$v_g = \frac{l}{\varphi_1} = \frac{c}{n - \lambda\frac{dn}{d\lambda}}$$

The group velocity v_g describes the propagation of the envelope of a laser pulse, whereas the phase velocity

$$v_p = \frac{c}{n(\lambda)}$$

describes the propagation of the carrier wave of a laser pulse. In dispersive materials $v_g \neq v_p$ holds generally, which implies that the phase of the field oscillations with respect to the envelope peak – the carrier-envelope-phase – changes during the propagation of a laser pulse through dispersive material. Fig. 9 illustrates the difference between a cosine-shaped waveform and a sine-shaped waveform.

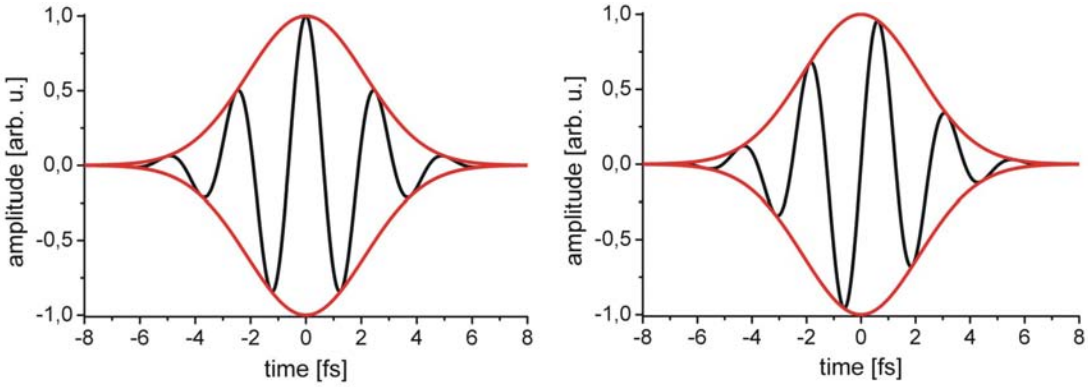

Fig. 9: left: calculated cosine-shaped waveform (black curve) of a laser pulse with a central wavelength of 760 nm and 5 fs full width at half maximum of the electric field envelope (red curve), right: sine-waveform after propagation of a cosine-waveform through 13 μm of fused silica, which causes a CEP shift of $\pi/2$.

φ_2, which describes the quadratic change of the spectral phase, is called GDD (group delay dispersion) or linear chirp. The GVD (group velocity dispersion) is the GDD per material length l:

$$GDD = \varphi_1 = \frac{d^2\varphi}{d\omega^2} = GVD \cdot l$$
$$GVD = \frac{d^2k}{d\omega^2}$$

φ_3, which describes the cubic change of the spectral phase, is called the TOD (third order dispersion). φ_4 describes the quartic change of the spectral phase.

For many materials, the dependence of the refractive index n on the wavelength λ can be well described by the Sellmeier-equation, a description of n by four empirical parameters a_1 - a_4 in a wavelength range usually between 300 and 1100 nm. In an uniaxial birefringent material like e.g. BBO or quartz exist two equal symmetry axes, which differ from a third symmetry axis. The corresponding refractive index for the two identical symmetry axes is called n_o, which stands for ordinary refractive index. The refractive index for

the third symmetry axis is called extraordinary refractive index n_e. For α- and β-BBO the ordinary and extraordinary refractive indices $n_o(\lambda)$ and $n_e(\lambda)$ and its derivatives can generally be described by the following equations:

$$
\begin{aligned}
n(\lambda) &= \left(a_1 + \frac{a_2}{\lambda^2 - a_3} - a_4\lambda^2\right)^{\frac{1}{2}} \\
b &= a_4 + \frac{a_2}{(\lambda^2 - a_3)^2} \\
\frac{dn}{d\lambda} &= -\frac{\lambda b}{n} \\
\frac{d^2n}{d\lambda^2} &= -\frac{b}{n} - \frac{\lambda^2 b^2}{n^3} + \frac{4\lambda^2 a_2}{n\,(\lambda^2 - a_3)^3}
\end{aligned}
$$

The corresponding coefficients for α-BBO are (λ in μm) [45]:

refractive index	a_1	a_2	a_3	a_4
n_o	2.7471	0.01878	0.01822	0.01354
n_e	2.3174	0.01224	0.01667	0.01516

The corresponding coefficients for β-BBO are (λ in μm) [46]:

refractive index	a_1	a_2	a_3	a_4
n_o	2.7405	0.0184	0.0179	0.0155
n_e	2.3730	0.0128	0.0156	0.0044

For crystal quartz the ordinary and extraordinary refractive indices n_o and n_e can be described with a so-called Laurent-series equation:

$$
\begin{aligned}
n &= \left(a_1 + a_2\lambda^2 + \frac{a_3}{\lambda^2} + \frac{a_4}{\lambda^4} + \frac{a_5}{\lambda^6} + \frac{a_6}{\lambda^8}\right)^{\frac{1}{2}} \\
\frac{dn}{d\lambda} &= \frac{1}{n}\left(a_2\lambda - \frac{a_3}{\lambda^3} - \frac{2a_4}{\lambda^5} - \frac{3a_5}{\lambda^7} - \frac{4a_6}{\lambda^9}\right) \\
\frac{d^2n}{d\lambda^2} &= -\frac{1}{n^3}\left(a_2\lambda - \frac{a_3}{\lambda^3} - \frac{2a_4}{\lambda^5} - \frac{3a_5}{\lambda^7} - \frac{4a_6}{\lambda^9}\right)^2 + \frac{1}{n}\left(a_2 + \frac{3a_3}{\lambda^4} + \frac{10a_4}{\lambda^6} + \frac{21a_5}{\lambda^8} + \frac{36a_6}{\lambda^{10}}\right)
\end{aligned}
$$

The corresponding coefficients for crystal quartz are (λ in μm) [47]:

refractive index	a_1	a_2	a_3
n_o	2.35728	$-1.17\cdot10^{-2}$	$1.054\cdot10^{-2}$
n_e	2.3849	$-1.259\cdot10^{-2}$	$1.079\cdot10^{-2}$

refractive index	a_4	a_5	a_6
n_o	$1.34143\cdot10^{-4}$	$-4.45368\cdot10^{-7}$	$5.92362\cdot10^{-8}$
n_e	$1.6518\cdot10^{-4}$	$-1.94741\cdot10^{-6}$	$9.36476\cdot10^{-8}$

3.1.4 Phase-matching in birefringent materials

Like the explanations of the previous section also the concept of phase-matching, which is presented in this section, will be needed for the calculations in chapter 4.2. Efficient harmonic generation in nonlinear media requires the same fundamental and harmonic phase velocities. Otherwise the harmonic is generated by constructive interference over a certain distance and then by destructive interference converted back to fundamental light. Only in case of equal phase velocities, which is called phase-matching, a perfectly constructive interference of the harmonic light waves, which are generated at different places in the whole nonlinear medium, is guaranteed:

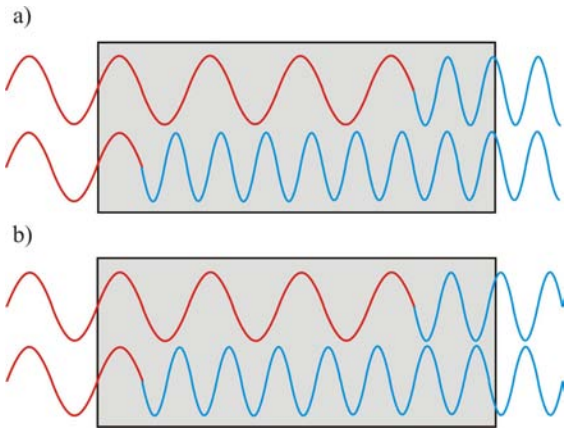

Fig. 10: a) constructive interference of harmonic waves (blue) generated at different locations in the nonlinear medium, b) destructive interference in case of different phase velocities of fundamental (red) and harmonic wave.

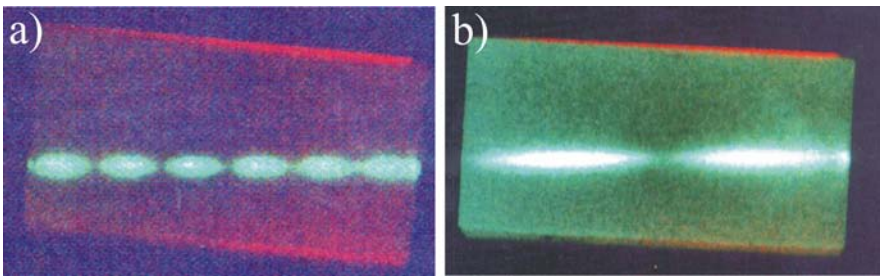

Fig. 11: a) SHG in BBO far away from phase-matching: alternately constructive and destructive interference of the generated SH-waves reduces the SHG efficiency b) SHG in BBO closer to phase-matching [48].

Due to the wavelength-dependant refractive index the phase-velocities of the fundamental and the harmonic wave are different. The solution is the usage of birefringent materials and different polarisations for the fundamental and harmonic waves, so that the funda-

mental and harmonic refractive indices are equal. The o-wave has the ordinary refractive index and the refractive index of the e-wave can be set for phase-matching by changing the angle θ between the optical axis and the k-vector. In case of uniaxial birefringent crystals this composed refractive index n_θ and its derivatives are given by [49]:

$$
\begin{aligned}
n_\theta &= \left(\frac{\cos^2\theta}{n_{o,2\omega}^2} + \frac{\sin^2\theta}{n_{e,2\omega}^2} \right)^{-\frac{1}{2}} \\
\frac{dn_\theta}{d\lambda} &= n_\theta^3 \left(\frac{\cos^2\theta}{n_{o,2\omega}^3} \frac{dn_{o,2\omega}}{d\lambda} + \frac{\sin^2\theta}{n_{e,2\omega}^3} \frac{dn_{e,2\omega}}{d\lambda} \right) \\
\frac{d^2n_\theta}{d\lambda^2} &= \frac{3}{n_\theta} \left(\frac{dn_\theta}{d\lambda} \right)^2 + n_\theta^3 \Bigg[- \frac{3\cos^2\theta}{n_{o,2\omega}^4} \left(\frac{dn_{o,2\omega}}{d\lambda} \right)^2 + \frac{\cos^2\theta}{n_{o,2\omega}^3} \frac{d^2n_{o,2\omega}}{d\lambda^2} \\
&\qquad - \frac{3\sin^2\theta}{n_{e,2\omega}^4} \left(\frac{dn_{e,2\omega}}{d\lambda} \right)^2 + \frac{\sin^2\theta}{n_{e,2\omega}^3} \frac{d^2n_{e,2\omega}}{d\lambda^2} \Bigg]
\end{aligned}
\tag{5}
$$

Besides energy conservation harmonic generation in birefringent crystals has also to fulfill momentum conservation, which is just another interpretation of the term phase-matching. Depending on the orientation of the fundamental wave and the second harmonic wave there are several possible types of phase-matching. Two common geometries are type I and type II phase-matching:

- type I SHG: the fundamental is an o-wave, the second harmonic is an e-wave

$$
\begin{aligned}
2k_{o,\omega} = k_{\theta,2\omega} \Leftrightarrow 2\frac{\omega n_{o,\omega}}{c} &= \frac{2\omega n_{\theta,2\omega}}{c} \Leftrightarrow n_{o,\omega} = n_{\theta,2\omega} \\
\cos^2\theta &= \left(\frac{\frac{1}{n_{o,\omega}^2} - \frac{1}{n_{e,2\omega}^2}}{\frac{1}{n_{o,2\omega}^2} - \frac{1}{n_{e,2\omega}^2}} \right) \\
\Delta k &= k_{\theta,2\omega} - 2k_{o,\omega}
\end{aligned}
$$

- type II SHG: the fundamental is split into an o-wave and an e-wave, the second harmonic is an e-wave

$$
\begin{aligned}
k_{o,\omega} + k_{\theta,\omega} = k_{\theta,2\omega} \Leftrightarrow \frac{\omega n_{o,\omega}}{c} + \frac{\omega n_{\theta,\omega}}{c} &= \frac{2\omega n_{\theta,2\omega}}{c} \Leftrightarrow n_{o,\omega} + n_{\theta,\omega} = 2n_{\theta,2\omega} \\
\Delta k &= k_{\theta,2\omega} - k_{o,\omega} - k_{\theta,\omega}
\end{aligned}
$$

The expression for the phase-matching angle θ follows from eq. 5 and the corresponding equations for the refractive indices. In case of type II SHG exists no simple analytical formula for θ. However, θ can be found numerically by plotting $n_{o,\omega} + n_{\theta,\omega}$ and $2n_{\theta,2\omega}$ for a certain wavelength versus θ and finding the θ-angle at the intersection of both curves.

3.1.5 The spectrum of two laser pulses with a constant delay

The spectral domain of two delayed laser pulses will be needed for understanding the introduction of the slow loop of the active CEP stabilization in chapter 3.2.4 and the technique for the detection of the temporal overlap between two laser pulses, which is presented in chapter 4.1.3.

In the following the spectrum of two interfering laser pulses with real electric fields

$$E_1(t) = \frac{1}{2}\left(\frac{1}{2\pi}\int_{\omega=-\infty}^{+\infty} d\omega\sqrt{I_1(\omega)}e^{i(\phi_1(\omega)-\omega t)} + c.c.\right)$$
$$E_2(t) = \frac{1}{2}\left(\frac{1}{2\pi}\int_{\omega=-\infty}^{+\infty} d\omega\sqrt{I_2(\omega)}e^{i(\phi_2(\omega)-\omega(t+\tau))} + c.c.\right)$$

which are separated by a time delay τ is calculated. The spectral phase

$$\phi_i(\omega) = \varphi_{i0} + \varphi_i(\omega)$$

can be described as a sum of a frequency independent carrier-envelope-phase φ_{i0} and a frequency dependent part $\varphi_i(\omega)$. The complex electric field $E(\omega)$ is the Fourier transform of the real electric field $E(t)$ in the time domain:

$$\begin{aligned} E(\omega) &= \int_{t=-\infty}^{+\infty} dt E(t)e^{-i\omega t} \\ E(\omega) &= \sqrt{I(\omega)}e^{i\phi(\omega)} \\ E(\omega) &= E^*(-\omega) \\ I(\omega) &= I(-\omega) \\ \phi(\omega) &= -\phi(-\omega) \end{aligned}$$

For the measured spectrum $I(\omega)$ of two laser pulses $E_1(t)$ and $E_2(t)$ follows:

$$\begin{aligned} I(\omega) &= \left|\int_{t=-\infty}^{+\infty} dt\left[E_1(t)+E_2(t)\right]e^{i\omega t}\right|^2 \\ &= \frac{1}{2}\left|\int_{t=-\infty}^{+\infty} dt\frac{1}{2\pi}\int_{\omega'=-\infty}^{+\infty} d\omega'\left\{\sqrt{I_1(\omega')}\left(e^{i[\phi_1(\omega')-t(\omega'-\omega)]}+e^{-i[\phi_1(\omega')-t(\omega'+\omega)]}\right)\right.\right. \\ &\qquad \left.\left.+\sqrt{I_2(\omega')}\left(e^{i[\phi_2(\omega')-t(\omega'-\omega)-\omega'\tau]}+e^{-i[\phi_2(\omega')-t(\omega'+\omega)-\omega'\tau]}\right)\right\}\right|^2 \end{aligned}$$

Here Dirac's delta function $\delta(\omega)$ is defined by

$$\delta(\omega) = \frac{1}{2\pi} \int_{t=-\infty}^{+\infty} dt\, e^{-i\omega t}$$

With this follows for the spectrum $I(\omega)$:

$$\begin{aligned} I(\omega) = \frac{1}{2}\Bigg| \int_{\omega'=-\infty}^{+\infty} d\omega' \Bigg\{ & \sqrt{I_1(\omega')} \left[e^{i\phi_1(\omega')} \delta(\omega' - \omega) + e^{-i\phi_1(\omega')} \delta(\omega' + \omega) \right] \\ & + \sqrt{I_2(\omega')} \left[e^{i[\phi_2(\omega') - \omega'\tau]} \delta(\omega' - \omega) + e^{-i[\phi_2(\omega') - \omega'\tau]} \delta(\omega' + \omega) \right] \Bigg\} \Bigg|^2 \\ = & \left| \sqrt{I_1(\omega)} e^{i\phi_1(\omega)} + \sqrt{I_2(\omega)} e^{i[\phi_2(\omega) - \omega\tau]} \right|^2 \\ = & I_1(\omega) + I_2(\omega) + 2\sqrt{I_1(\omega) I_2(\omega)} \cos\left[\phi_1(\omega) - \phi_2(\omega) + \omega\tau\right] \end{aligned} \tag{6}$$

3.1.6 The spectrum of a train of laser pulses

The electric field $E(t)$ of a pulse train of a mode-locked laser with repetition rate $1/T$ is essential for the comprehension of the concept of the carrier-envelope-phase and its active stabilization presented in chapter 3.2.4. It can be described as a convolution of the complex electric field $pulse(t)$ of a single laser pulse consisting of a carrier $\exp(i\omega_0 t)$ and an envelope function $\hat{E}(t)$ and a comb $comb(t)$ of delta functions $\delta(t-nT)$ multiplied with a phase factor $\exp(in\Delta\phi+\phi_0)$, which describes the linear CEP shift between subsequent pulses of a mode-locked pulse train:

$$\begin{aligned}
pulse(t) &= \hat{E}(t)\exp(i\omega_0 t)\\
comb(t) &= \sum_{n=-\infty}^{+\infty}\exp\left[i(n\Delta\phi+\phi_0)\right]\delta(t-nT)\\
E(t) &= pulse(t) * comb(t)\\
&= \int_{t'=-\infty}^{+\infty} dt'\hat{E}(t-t')\exp\left[i\omega_0(t-t')\right]\sum_{n=-\infty}^{+\infty}\exp\left[i(n\Delta\phi+\phi_0)\right]\delta(t'-nT)\\
&= \sum_{n=-\infty}^{+\infty}\hat{E}(t-nT)\exp\left\{i\left[\omega_0(t-nT)+n\Delta\phi+\phi_0\right]\right\}
\end{aligned}$$

Using the convolution theorem and Poisson's sum rule (20), which is derived in chapter 7.1, with $2\pi x = \omega T - \Delta\phi$ one obtains for the electric field $E(\omega)$ of a mode-locked pulse train in the spectral domain:

$$\begin{aligned}
E(\omega) &= \mathcal{F}\left[pulse(t) * comb(t)\right]\\
&= \mathcal{F}\left[pulse(t)\right]\cdot\mathcal{F}\left[comb(t)\right]\\
&= \mathcal{F}\left[\hat{E}(t)\exp(i\omega_0 t)\right]\int_{t=-\infty}^{+\infty}dt\sum_{n=-\infty}^{+\infty}\exp\left[i(n\Delta\phi+\phi_0)\right]\delta(t-nT)\exp(-i\omega t)\\
&= \mathcal{F}\left[\hat{E}(t)\exp(i\omega_0 t)\right]\exp(i\phi_0)\sum_{n=-\infty}^{+\infty}\exp\left[in(\Delta\phi-\omega T)\right]\\
&= \mathcal{F}\left[\hat{E}(t)\exp(i\omega_0 t)\right]\frac{2\pi}{T}\exp(i\phi_0)\sum_{m=-\infty}^{+\infty}\delta\left(\omega-\frac{2\pi m}{T}-\frac{\Delta\phi}{T}\right)\\
&= \hat{E}(\omega)\cdot comb(\omega)
\end{aligned}$$

$E(\omega)$ describes an envelope function

$$\hat{E}(\omega) = \mathcal{F}\left[\hat{E}(t)\exp(i\omega_0 t)\right]$$

multiplied with a comb-like spectrum

$$comb(\omega) = \frac{2\pi}{T} \exp(i\phi_0) \sum_{m=-\infty}^{+\infty} \delta\left(\omega - \frac{2\pi}{T}m - \frac{\Delta\phi}{T}\right)$$

with comb lines

$$\begin{aligned} \omega_m &= \frac{2\pi}{T}m + \frac{\Delta\phi}{T} \\ &= f_{rep}m + f_{CEO}, \end{aligned}$$

at the distance

$$f_{rep} = \frac{2\pi}{T}$$

between adjacent comb lines and the carrier-envelope offset frequency

$$f_{CEO} = \frac{\Delta\phi}{T} = \frac{\Delta\phi f_{rep}}{2\pi}.$$

From $f_{CEO} = 0$ follows $\Delta\phi = 0$, which means that CEP stable laser pulses in the time domain have a zero offset frequency in the frequency domain. Fig. 12 illustrates the spectrum of a train of modelocked laser pulses:

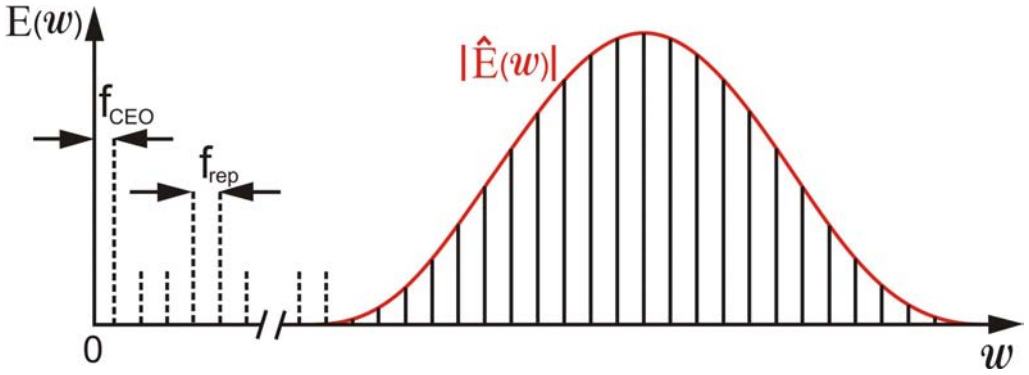

Fig. 12: Schematic view of a frequency comb spectrum.

3.2 Laser system

The laser system is based on a commercial core (Femtolasers Produktions Gesellschaft) adapted to the needs of the experiment. It generates CEP-stabilized laser pulses with 3.5 fs pulse duration (FWHM), 300 μJ pulse energy at 3 kHz repetition rate and a spectrum spanning from 450 nm to 1050 nm with a central wavelength of 760 nm [10]. The laser system can be divided into three parts: the oscillator, the amplifier and a hollow core fiber, which are described in the following.

3.2.1 Oscillator

The first observation of mode-locking in Ti:sapphire laser oscillators in 1991 by Spence et al. [50] and its theoretical explanation by means of the nonlinear Kerr effect [51] revolutionized the generation of ultrashort laser pulses. Compared to the dye laser systems, which have been used before, solid state lasers considerably simplified the operation of ultrashort laser systems. Hence, the oscillator system used in this work is a solid state laser based on Ti:Sa as gain medium. A predecessor of the oscillator has been published in [52]. Mode-locking is achieved by Kerr-lens mode locking in combination with a soft aperture formed by the focal spot size of the pump laser beam in the gain medium, which is smaller than the focal spot size of mode-locked laser beam. Therefore, only intense laser pulses, which are focused by the self-induced Kerr-lens and formed by mode-locked laser modes, experience gain, whereas unlocked laser modes suffer to much loss and eventually die out:

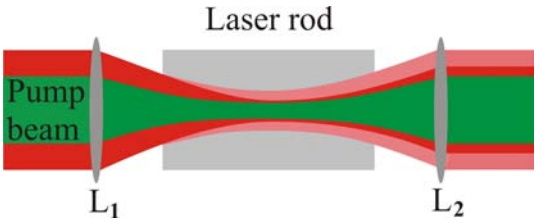

Fig. 13: Schematic view of Kerr-lens mode-locking: dark red output beam is high intensity pulsed radiation, light red output beam is low intensity beam [53].

Today's state-of-the-art femtosecond oscillators make use of chirped mirrors [54] for intracavity dispersion control. Chirped mirrors combine high reflectance with precise control of linear and even higher order chirp and are therefore superior to conventional prism or grating compressors.

A photo of the oscillator, which has been used in this work, is presented in the following figure:

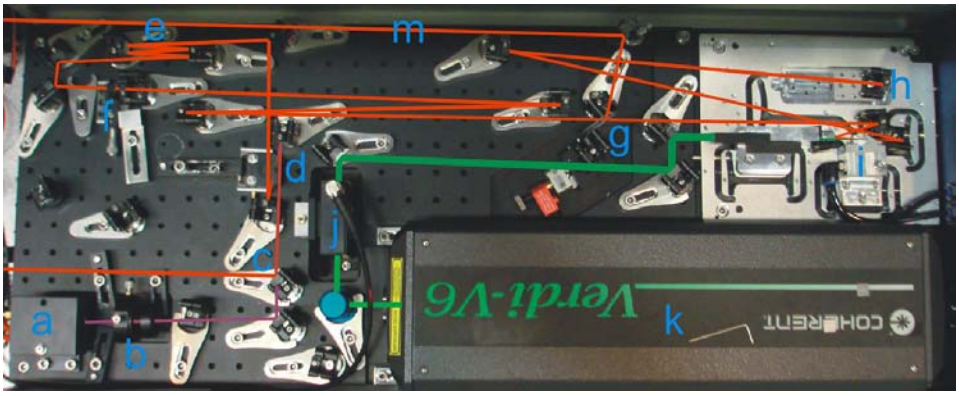

Fig. 14: Schematic beampaths in the oscillator of the modelocked laser pulses (red) and the pump laser (green): a) photo diode for beat signal detection, b) filter and lens for beat signal, c) beamsplitter for separation of beat signal from oscillator output, d) PPLN-crystal, e) chirped mirrors, f) output coupler, g) wedge with one reflection used for spectrum measurement, h) end mirror, i) Ti:Sa-crystal, j) acousto-optical modulator, k) pump laser, m) reflection from wedge for intracavity spectrum measurement.

The oscillator is based on an astigmatism-compensated X-folded geometry. 4.35 W of a frequency-doubled Nd:YVO_4 at 532 nm are focused with a lens in a Ti:Sapphire crystal as gain medium, which is cut at Brewster's angle in order to prevent reflection losses. The GDD of the laser pulses is controlled by a set of chirped mirrors and wedged fused silica plates. The wedged shape of the output coupler, which transmits 15 % of the incident radiation, prevents backreflections from outside into the oscillator, which could disturb the formation of mode-locked laser pulses. After transmission through the output coupler the laser pulses are compressed by two reflections upon each of two chirped mirrors. Afterwards they are focused in a periodically poled lithium niobate (PPLN) crystal, which is part of the fast loop of the CEP stabilization that is described in more detail in chapter 3.2.4. The chirp caused by the transmission through the PPLN crystal is compensated by another set of chirped mirrors and finally the subsequent amplifier system is seeded with CEP stabilized laser pulses, with 6 fs pulse duration (FWHM), a spectrum from 600 nm to 1000 nm (see Fig. 17), 70 MHz repetition rate and 280 mW average output power.

3.2.2 Multipass amplifier

The amplifier is based on the concept of chirped pulse amplification (CPA), which has been invented in 1985 [55]. The idea behind CPA is to prevent damage of the amplifier gain medium and other optical components by stretching the pulse duration from about

6 fs to about 15 ps and by this keeping the peak intensity of the amplified laser pulse below the damage threshold of the optical compontents. A predecessor of the amplifier has been published in [56]. The amplifier can be divided in three parts: first, a stretcher, which elongates the pulse duration, second, the actual multipass amplifier and ,third, a compressor, which reduces the pulse duration of the amplified pulses close to the Fourier-limit.
A schematic view of the complete amplifier system is shown in Fig. 15:

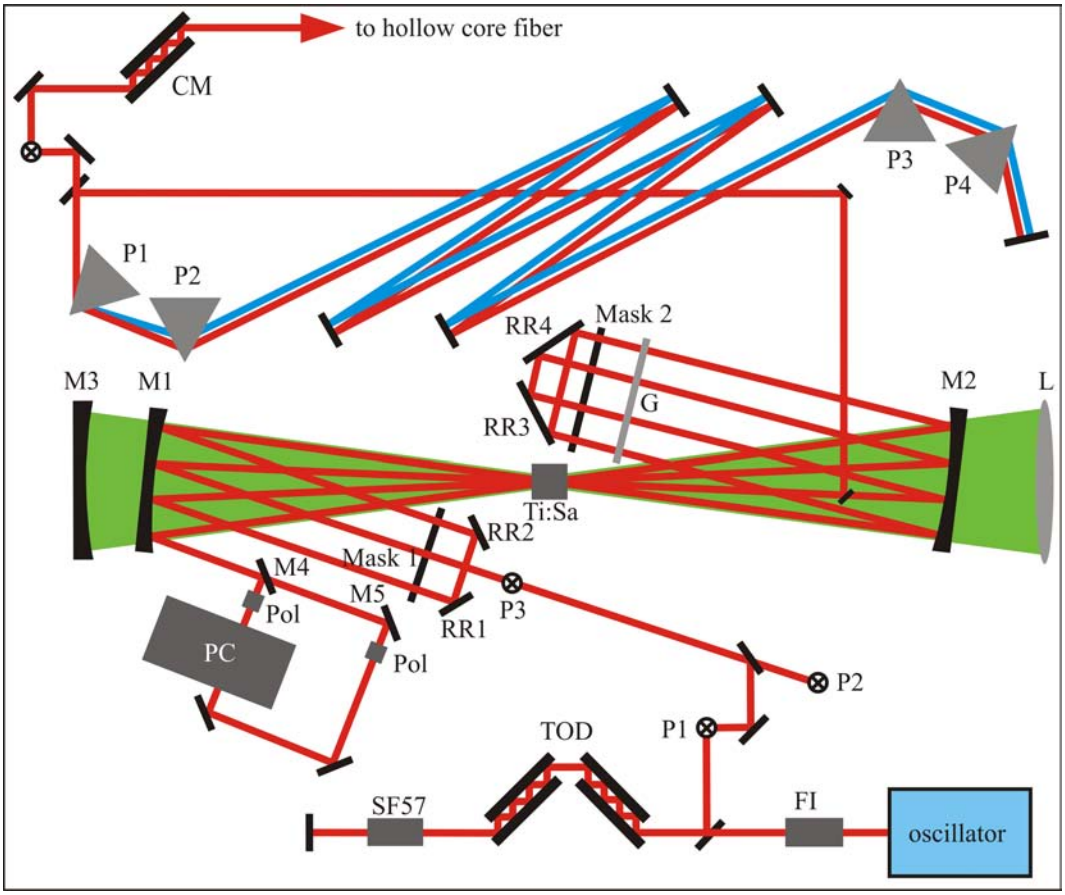

Fig. 15: Schematic view of the CPA-amplifier. FI: Faraday isolator for protecting oscillator from backreflections, TOD: chirped mirrors for cubic chirp compensation, SF57: glass for pulse-stretching, P1 - P3: periscopes, PC: Pockels cell for pulse selection, Pol: polarizers, G: Gauss-filter, Mask 1 and Mask 2: masks for preventing lasing in the amplifier cavity, RR1 - RR4: retroreflectors, M1 and M2: cavity mirrors of amplifier, Ti:Sa: amplifier crystal, M3: retroreflector of pump beam, L: lens, M4 and M5: selecting mirrors after 4th pass, P1 - P4: prisms of prism compressor, CM: positively chirped mirrors for final pulse compression.

The laser pulses, which are generated by the oscillator, propagate first through a Faraday

isolator in order to prevent backreflections or amplifed spontaneous emission (ASE) from disturbing the oscillator. The Faraday isolator is surrounded by two polarizers, which turn the polarization by 90°. After this, about 56 reflections on two pairs of chirped mirrors introduce positive third order dispersion (TOD). The reason for this is that the prism compressor after the amplifier usually overcompensates the TOD, which is generated by the stretcher and other optical components in the amplifier if the overall GDD is zero [56, 57]. The last component of the stretcher is a 5 cm long piece of SF57 glass for pulse stretching.
The multipass amplifier consisting of of a confocal z-folded astigmatically compensated cavity formed by the mirrors M1 and M2 in Fig. 15 is seeded with stretched laser pulses of about 1 nJ pulse energy and a repetition rate of 70 MHz. 9 passes through a 3.5 mm long Brewster-cut Ti:Sa crystal, which is pumped by 20 W of a frequency-doubled diode-pumped Nd:YLF laser at 532 nm, increase the pulse energy by a factor of $1{\cdot}10^6$ to 1.3 mJ with a reduced final repetition rate of 3 kHz. The reduction of the repetition rate takes place after the 4th pass by a Pockels cell, which is sourrounded by two polarizers. Reducing the repetition rate after the 4th pass has two reasons: First, the pulse shape of the nanosecond pump pulse is visible as envelope of the amplified MHz pulse train after detection with a photo diode and the most intense pulse of this pulse train can be easily selected. Second, most of the ASE, which happened during the first four passes, is blocked by the Pockels cell and therefore not further amplified in the next five passes. The amplifier crystal is operated in saturation in order to generate amplified output pulses with the lowest possible fluctuations in pulse energy since these fluctuations would severely compromise the CEP stability and spectral stability due to nonlinear effects (SPM, Kerr-effect) in the subsequent hollow core fiber. Masks 1 and 2 in front of the retroreflectors RR1 - RR4 in Fig. 15 prevent the amplifier cavity from lasing and suppress the ASE. The nine passes for amplification are arranged in a three dimensional geometry ensuring an optimum matching of the seed beam and the pump beam in the amplifier crystal: The first four and the second four passes propagate in two different planes. The 9th pass propagates in a third plane. Fig. 16 illustrates the beam geometry in the amplifier cavity:

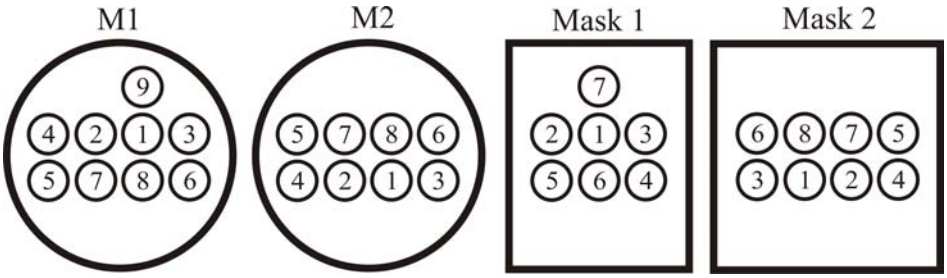

Fig. 16: Pattern on the focusing mirrors M1 and M2 and the masks mask 1 and mask 2 in Fig. 15 generated by the different passes, the viewing direction on M1 and M2 is from the Ti:Sa crystal, the viewing direction on mask 1 is from the retroreflectors RR1 and RR2, the viewing direction on mask 2 is from mirror M2.

The much smaller gain bandwidth of the Ti:Sa compared to the spectrum of the seed pulses results in a reduced spectral bandwidth of the amplified pulses and by this in an increased pulse duration. The spectral narrowing during the amplification is partially compensated by a Gauss-filter in front of mask 2 in Fig. 15, which exhibits a larger spectral transmission in the wings than in the center of the gain bandwidth of Ti:Sa. Nevertheless, the spectrum of the amplified pulses supports only a Fourier-limited pulse duration of 23 fs (see Fig. 17).
In a third step the amplified and still stretched pulses are compressed by means of a prism compressor and positively chirped mirrors. A crucial point of the compression is that in previous systems the compressed laser pulse entered the last prism P1 in Fig. 15 with negative chirp. Due to the high intensities SPM occured in prism P1, which leads in combination with negative chirp to spectral narrowing [58]. Therefore the compression was changed such that the laser pulse enters prism P1 with stronger negative chirp in order to reduce the peak intensity and to avoid SPM. The final compression takes place by 14 reflections on positively chirped mirrors [10]. The overall transmission of the compressor is 83 %, which results in amplified pulses of 1.1 mJ pulse energy, 23 fs pulse duration at a repetition rate of 3 kHz.

3.2.3 Hollow core fiber

The last part of the laser system is a 1 m long hollow core fiber (HCF) with 260 μm core diameter filled with 1.8 bar of Neon for spectral broadening of the amplified laser pulses by means of self phase modulation [59]. A typical output spectrum of the HCF is shown in Fig. 17:

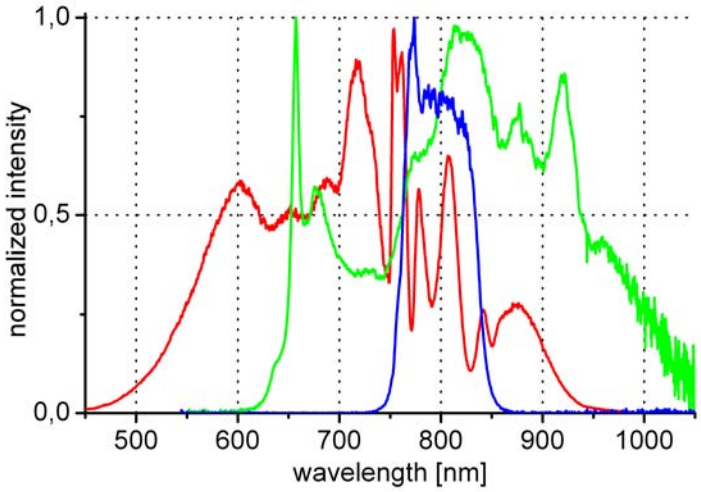

Fig. 17: Intracavity spectrum of oscillator (green), spectrum after prism compressor of amplifier (blue) and spectrum after hollow core fiber (red).

The transmission of the HCF is about 50 %. After pulse compression on three pairs of negatively chirped mirrors laser pulses with 500 μJ pulse energy, 3.5 fs pulse duration (FWHM) and 3 kHz repetition rate are delivered to the experimental setup, which is described in chapter 4.1.

3.2.4 Carrier-envelope-phase stabilization

The active stabilization of the carrier envelope phase (CEP) can be divided into two parts: First, the fast loop stabilizes the CEP of the laser pulses, which are generated by the oscillator. As its name implies, this stabilization is fast and runs on a MHz time scale since it has to compensate fast changes of the CEP due to mechanical vibrations, air currents and other noise sources. On its way through the multipass amplifier and the HCF the CEP stabilized laser pulses accumulate a substantial amount of CEP change, which varies on a Hz scale [60] and is mainly caused by thermal instabilities. This slow CEP drift can be compensated by a second stabilization loop - the slow loop - which runs at 100 Hz. Fast loop and slow loop are completely decoupled since the fast loop balances CEP changes via the pump laser power of the oscillator, whereas the slow loop controls tiny changes in the prism compressor of the CPA amplifier.

The fast loop is based on the f-to-0 method using difference frequency generation based on quasi phase-matching in a periodically poled lithium niobate crystal (PPLN, see Fig. 14) [61]. The frequency comb

$$f_{fund} = k f_{rep} + f_{CEO}$$

of the long wavelength wing of the fundamental spectrum, which is amplified by SPM in the PPLN crystal, is interfered with the frequency comb

$$f_{DFG} = nf_{rep} + f_{CEO} - (mf_{rep} + f_{CEO}) = (n-m)f_{rep},\ \text{n>m} \tag{7}$$

of the generated difference frequency. From equation 7 follows that mode-locked laser pulses synthesized by difference frequency generation are inherently CEP stabilized [62, 63]. The resulting beating frequency

$$f_{beat} = |f_{fund} - f_{DFG}| = |(n-m-k)f_{rep} \pm f_{CEO}| \tag{8}$$

in the spectral region, where both the fundamental and the DFG spectrum interfere, can be observed by frequency analysis of the acquired photodiode signal. f_{CEO}, which is detected by means of a bandpass filter for $n-m-k=0$, is used as an input signal for an analog PI-controller, which stabilizes f_{CEO} at $f_{rep}/4$. This ensures that every fourth pulse of the pulse train, which is leaving the oscillator, has the same CEP. The output signal of the fast loop electronics controls the amplitude of an acousto-optical modulator, which sets the power of the oscillator pump laser (see Fig. 14 on page 33). Since the refractive index in the Ti:Sa crystal depends on the pump power via the nonlinear Kerr effect, both group velocity and phase velocity of the laser pulses can be balanced on a MHz time scale, that

$$f_{CEO} = \frac{f_{rep}}{4}$$

is guarenteed. The Pockels cell in the amplifier picks every 4n^{th} pulse of the MHz pulse train, whereas n is an integer. This ensures that only laser pulses with identical CEP are amplified.

The slow loop is based on the f-to-2f-method. Instead of interfering the DFG spectrum with the fundamental spectrum like in the fast loop, the second harmonic of the red part of the fundamental spectrum is generated and interfered with the blue part of the fundamental spectrum. Fortunately the fundamental spectrum after the HCF is broad enough so that no further spectral broadening e.g. by means of photonic crystal fibers is needed [64]. In contrast to the fast loop the change of the CEP is detected by a spectrometer and as outlined in chapter 3.1.5 the spectrum between two laser pulses delayed by τ is given by:

$$I(\omega) = I_1(\omega) + I_2(\omega) + 2\sqrt{I_1(\omega)I_2(\omega)}\cos\left[\phi_1(\omega) - \phi_2(\omega) + \omega\tau\right]$$

In case of the f-to-2f-interferometer for the fundamental phase ϕ_{Fund} and the phase ϕ_{SH} of the second harmonic as well as for the corresponding spectra $I_{Fund}(\omega)$ and $I_{SH}(\omega)$ holds:

$$\phi_1(\omega) = \phi_{SH}(\omega) = 2\varphi_0 + \varphi_{SH}(\omega)$$
$$\phi_2(\omega) = \phi_{Fund}(\omega) = \varphi_0 + \varphi_{Fund}(\omega)$$
$$I_1(\omega) = I_{SH}(\omega)$$
$$I_2(\omega) = I_{Fund}(\omega)$$

This gives a modulated spectrum with modulation period $\Delta f = 1/\tau$, which decreases with increasing delay τ. Since the necessary delay τ between the blue part of the fundamental pulse and the frequency-doubled red part of the fundamental pulse is usually determined by the chirp of the fundamental laser pulse, which is sent into the f-to-2f-interferometer, a fundamental pulse with stronger chirp causes a higher modulation frequency in the observed f-to-2f-interferogram. The phase shift φ_0 of the fringes with modulation period Δf is a direct measure of the fundamental CEP:

$$I(\omega) = I_{Fund}(\omega) + I_{SH}(\omega) + 2\sqrt{I_{Fund}(\omega) I_{SH}(\omega)} \cos\left[\phi_{SH}(\omega) - \phi_{Fund}(\omega) + \omega\tau + \varphi_0\right]$$

A typical spectrum acquired by the f-to-2f-interferometer is shown in Fig. 18:

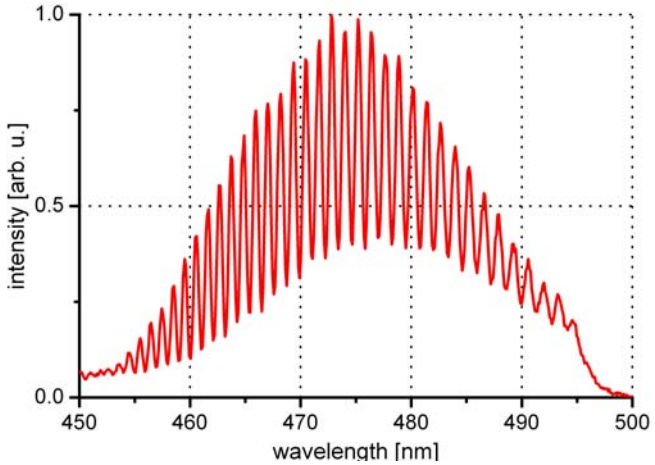

Fig. 18: Spectrum of fundamental laser pulse and generated second harmonic for CEP stabilization after the hollow core fiber.

A shift of the fringes of this spectrum by 2π corresponds to a CEP shift of 2π. Therefore the PID algorithm of the slow loop stabilizes the position of the fringes by moving prism P2 in Fig. 15 on page 34. This time the group velocity and the phase velocity of the laser pulses are balanced by changing the amount of glass in the laser beam. These prism movements have no substantial influence on the laser pulse duration since only tiny movements on a μm-scale are needed for the necessary CEP corrections.

4 Frontiers advanced

4.1 Novel setup for the combination of attosecond XUV-pulses with intensive laser pulses of different spectral ranges

4.1.1 Design of the vacuum system

An overview of the AS2 beamline is shown in Fig. 19. The laser system as described in chapter 3.2 generates laser pulses with vertical polarization, which is more appropriate for designing XUV mirrors with high reflectance at non-normal incidence. These laser pulses, propagating in a vacuum system, are focused on a gas target T1 by a concave mirror M2, ROC = -1200 mm. The target consists of a nickel tube (3 mm diameter, 300 μm wall thickness, Good Fellow) filled with Neon at a backing pressure of 200 mbar. In the 100-μm diameter focus high harmonics with photon energies up to 140 eV are generated. Most of the optical components are motorized and can be adjusted under vacuum conditions: the flat mirror M1 and the concave mirror M2 in the HHG chamber (see Fig. 19) are motorized for steering the direction of the beam. The gas target T1 can be moved in all three directions in space in order to position the gas target relative to the laser focus for optimum high harmonic generation. The movement along the beam axis allows to position the target into the part of the confocal parameter, where preferably short-trajectory harmonics are generated [27].

After HHG, both the generated high harmonic beam and the remaining fundamental light propagate collinearly into the second vacuum chamber, the delay chamber. Here the fundamental light and the high harmonics are separated into the two paths of a Mach-Zehnder interferometer. One leg of the interferometer provides the possibility of adjusting the delay between the fundamental driving pulse and the generated attosecond pulse. The much smaller divergence of the high harmonic beam compared to the fundamental beam allows for the spatial separation of the two beams by means of a perforated mirror PM1 with a hole diameter of 1.0 mm through which the HH beam can pass. The distance between the target T1 and PM1 amounts to 900 mm. The fundamental light transmitted through the hole of PM1 is blocked by thin metal filters selected according to their transmittance (e.g. 500 nm Zr for the energy range of 70 to 140 eV, Lebow). These metal foils act as high pass filters for the high harmonic radiation. In combination with the reflectance characteristics of the multilayer mirror ML a part of the HH spectrum is reflected. For few cycle laser pulses at a certain CEP the cut-off part of the continuum is smooth [65]. Filtering this region of the spectrum corresponds to the isolation of one single attosecond pulse out of an attosecond pulse train in the time domain [6]. HHG is optimized in terms of beam profile by means of an XUV sensitive camera (XUV camera PIXIS XO, Roper Scientific, CCD 1 in Fig. 19) and in terms of spectral distribution with a home-made grating spectrometer (grating 001-0266, Hitachi [66]). In order to preserve the interferometer stability, the multilayer mirror ML is not moved for beam profile measurements or spectral measurements of the generated HH. Instead, mirrors coated with 80 % Au and 20 % Pd (Georg Albert PVD) on superpolished silicon substrates (Gooch & Housego) are moved in with a translation stage. At large incidence angles ($> 80°$,

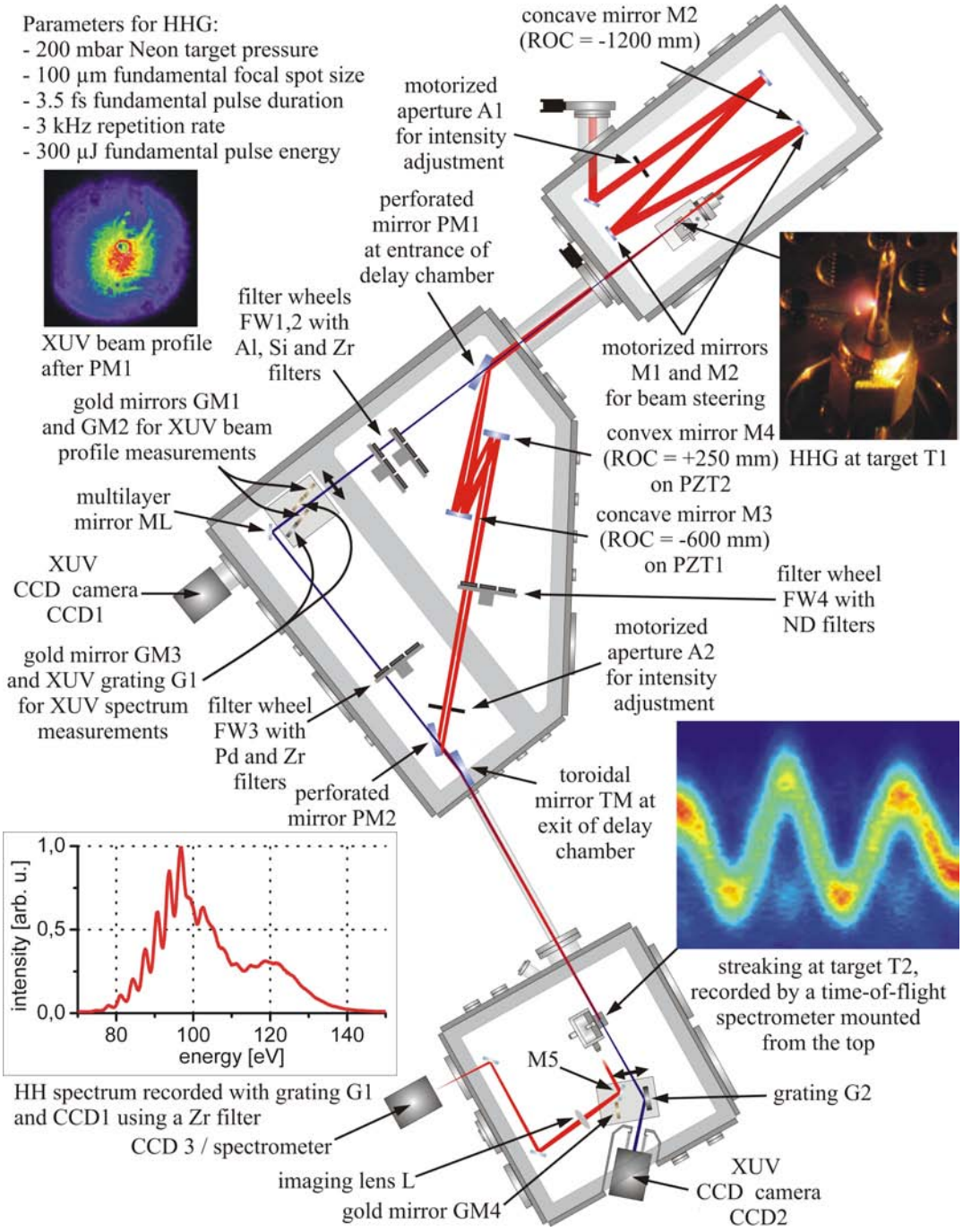

Fig. 19: Experimental setup consisting of three vacuum chambers: chamber for HHG (top right), delay chamber (middle) and experiment chamber (bottom right).

measured from the normal axis resulting in a reflectance > 60 %) the HH radiation is reflected on two gold mirrors, bypassing the multilayer mirror, and is detected for beam profile measurements on a camera chip of a XUV CCD camera (CCD1 in Fig. 19). For spectral measurements the high harmonics are reflected off a third gold mirror, which can be inserted and subsequently dispersed by a grating. The dispersed beam again circumvents the multilayer mirror and spectra are measured with the same XUV camera CCD1. For propagation of the HH to the experiment, all gold mirrors are moved out of the XUV beam.

The mirrors M3 and M4 in the other path of the Mach-Zehnder interferometer combine three functions:

1. A telescope that consists of M3 (ROC = -600 mm) and M4 (ROC = +250 mm) for reducing the beam diameter.
2. The delay between the fundamental pulse and the attosecond pulse in the other path of the interferometer is set by moving mirror M3, which is mounted on a nm-resolution piezo translation stage.
3. Instabilities of the Mach-Zehnder interferometer are compensated by movements of mirror M4, which is mounted on a piezo translation stage as well. M4 is the active part of a stabilization system of the interferometer, which is described in chapter 4.1.4.

The paths of both the fundamental beam and the high harmonics beam are recombined by a second perforated mirror PM2 with a hole diameter of 2.0 mm, which is approximately the XUV beam diameter at this point of the diverging XUV beam. The beams are subsequently focused on the experimental target T2 by a toroidal mirror TM (Société Européenne de Systèmes Optiques). The optical path length of the legs of the interferometer is 1700 mm. The distance between the second perforated mirror PM2 and the toroidal mirror is 100 mm. The toroidal mirror is coated with nickel, the angle of incidence is 86° measured from the normal axis, the effective focal length is 720 mm and the accepted fundamental beam diameter is 6 mm. The divergence of the fundamental beam after the telescope formed by mirrors M3 and M4 is set such that the toroidal mirror TM focuses both the fundamental and the HH beam at the position of the experimental target T2. The distance between TM and T2 is 982 mm. The focal spot size of the fundamental focus generated by the toroidal mirror in the experiment chamber is 150 μm, the maximum intensity is $5{\cdot}10^{13}$ W/cm^2. The focal spot size of the XUV beam, measured with the knife-edge method, is 40 μm and therefore by a factor of 3 to 4 smaller than the focal spot size of the intense fundamental beam.

The experimental target T2 consists of a gas nozzle with motorized movement along all three dimensions. In pump-probe experiments, photoelectron spectra, ion mass spectra and transient HH spectra can be measured for different delays between the fundamental pulse and the XUV pulse. The photoelectron spectra are recorded by means of an electron time-of-flight spectrometer (Stefan Käsdorf, Geräte für Forschung und Industrie)

with an energy resolution of about 1 % of the total kinetic photoelectron energy. The ion mass spectra are measured with a reflectron spectrometer (Stefan Käsdorf, Geräte für Forschung und Industrie) [67]. Transient HH spectra can be measured with a second XUV-spectrometer after dispersion of the HH beam on grating G2 and detection of the spectra on CCD2 (grating 541 00 220, Jobin Yvon; XUV camera PIXIS XO, Roper Scientific). A photo of the target in the experiment chamber is shown in Fig. 20:

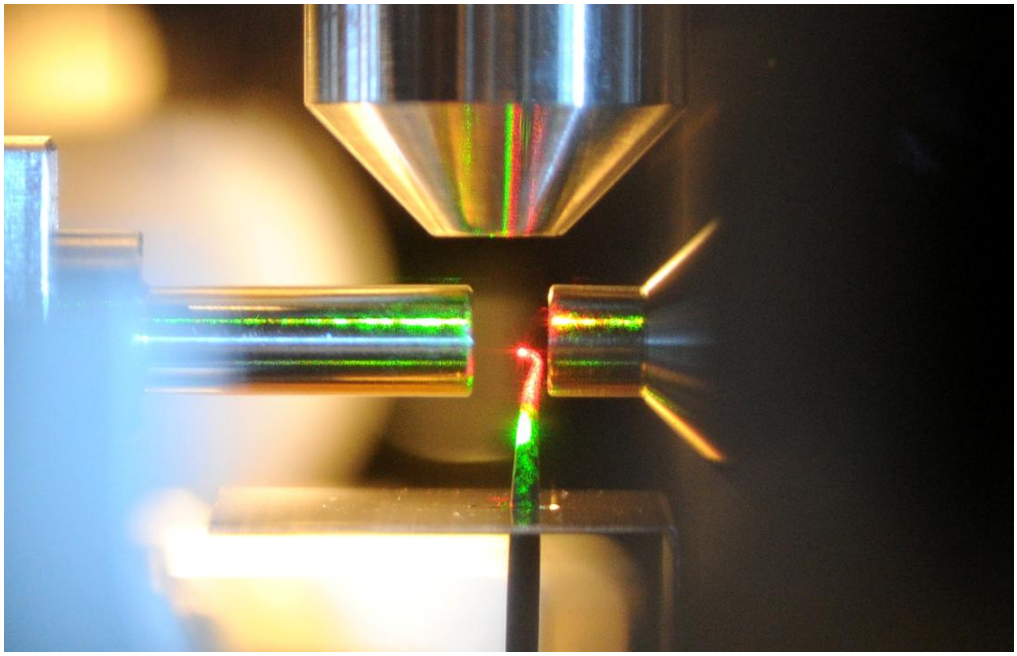

Fig. 20: Photo of the experimental target in the experiment chamber. The viewing direction is oposed to the propagation direction of the laser beam. The horizontal cylinders are the repeller and extractor of the reflectron ion spectrometer. Pump and probe laser pulses are focused by the toroidal mirror on the tip of gas nozzle in between. The conical entrance of the electron time-of-flight spectrometer is mounted from the top.

Typical gas loads for HHG result in a pressure of $5{\cdot}10^{-3}$ mbar in the HHG chamber. Differential pumping between the three vacuum chambers allows for a pressure of $5{\cdot}10^{-4}$ mbar in the delay chamber and $8{\cdot}10^{-6}$ mbar in the experiment chamber. The micro-channel plate (MCP) detector of the electron time-of-flight spectrometer, which is mounted to the experiment chamber, is differentially pumped by a separate turbo molecular pump. The maximum gas load of the experimental target T2 is set such that the pressure of $3{\cdot}10^{-6}$ mbar for Neon as target sample is not exceeded in order to ensure safe operation of the MCP detector.

Summarizing all these features, four distinct advantages of the 2nd generation attosecond beamline compared to its predecessors can be stated:

1. The spatial separation of the fundamental light from the generated XUV light allows for a tailoring of the pump laser pulse according to the requirements of the experimental target, e.g. by nonlinear frequency conversion. In the previous attosecond beamlines [7, 68] a manipulation of the remaining fundamental light after HHG was not possible due to the collinear propagation of fundamental light and XUV light after HHG.

2. The angle of incidence on the flat multilayer mirror ML is 45°, which allows for mirror designs with significant higher reflectivity and larger spectral bandwidth for s-polarized XUV light as compared to near-normal incidence mirror designs as used in the previous attosecond beamlines.

3. Focusing both the fundamental and the HH beam by means of a toroidal mirror at grazing incidence offers simultaneous access to transient absorption measurements and photoelectron streaking experiments at large XUV photon flux.

4. A much longer Rayleigh range of both the fundamental and the XUV beam in the focus of the experimental target simplifies the alignment for streaking experiments considerably.

4.1.2 Calibration of an XUV grating spectrometer

The XUV spectrometers (G1 and G2 in Fig. 19) are calibrated using the absorption edges of aluminum and silicon foils. The XUV radiation is horizontally dispersed by the grating and the different wavelength components are recorded on the CCD-chip. Full vertical binning of the CCD chip results in raw spectra with the number of counts versus the pixel column number n. In the narrow wavelength range of interest it is a reasonable assumption that the pixel number n is proportional to the wavelength λ. The pixel number of the silicon absorption edge is n_1; the pixel number of the aluminum absorption edge is n_2. With this follows the corresponding wavelength λ for each pixel n:

$$\lambda(n) = \frac{\lambda(n_1) - \lambda(n_2)}{n_1 - n_2}(n - n_2) + \lambda(n_2)$$

The conversion from wavelengths λ in nm to photon energies E in eV is calculated by E[eV]=1239/λ[nm] derived from $E = h\nu$. Typical raw spectra recorded after transmission through thin aluminum, silicon and zirconium foils and the corresponding calibrated XUV spectra are shown in Fig. 21:

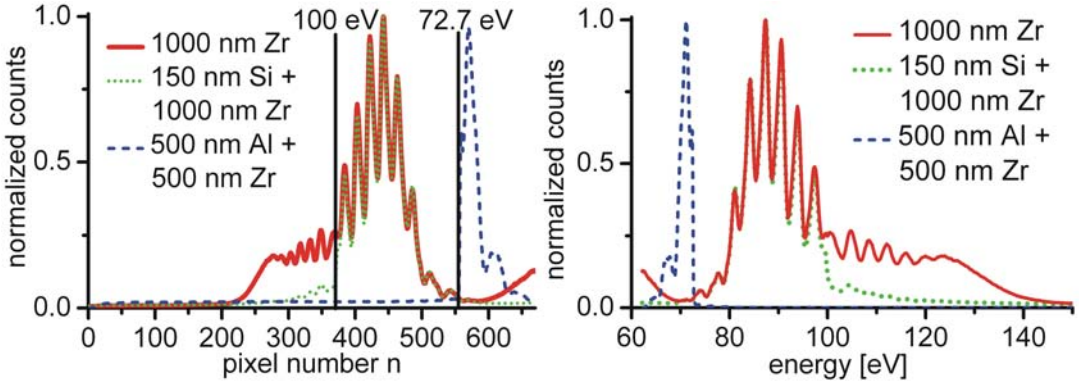

Fig. 21: Raw HH spectra (left) and calibrated HH spectra (right) measured after transmission through thin metal foils made of Zr (solid line), Si (dotted line) and Al (dashed line). The spectrum below 70 eV in case of a 1000 nm zirconium filter shows the second diffraction order of the grating.

4.1.3 Alignment of the temporal overlap

Finding the temporal overlap of the pump and the probe pulses is straightforward in a collinear setup like in the first generation attosecond beamline [7,68]. The metal filters, which block the fundamental light that propagates along the XUV beam path, are removed and two fundamental laser pulses are interfered in the focus of the experimental target. Each of the two laser pulses propagates along one of the two paths of the interferometer. A lens, which images the focus at the position of the experimental target through a glass window on a CCD-camera outside the vacuum chamber, is sufficient for the detection of the interference pattern between two fundamental laser pulses (CCD3 in Fig. 19). In case of a large interferometer setup, however, this method causes severe difficulties since the coherence length of the fundamental laser pulses amounts to only a few microns and determines the delay range within which this spatial interference is visible. Finding this micrometer-size overlap region in a Mach-Zehnder interferometer is non-trivial. Using a high-resolution spectrometer, one can observe the interference in the spectral domain over a much wider delay range. The same imaging system in combination with a spectrometer (HR4000, 0.05 nm resolution, Ocean Optics) instead of a CCD camera observes spectral fringes as described by eq. 6 on page 29. In the ideal case the two laser beams separated by a time delay τ have an equal spectrum $I_1(\omega) = I_2(\omega) = S(\omega)$ and zero phase $\phi_1(\omega) = \phi_2(\omega) = 0$. Then, the measured spectrum is given by:

$$I(\omega) = 2S(\omega)\,[1 + \cos(\omega\tau)] \tag{9}$$

This means that the spectrum of two delayed but apart from that identical laser pulses is the modulated spectrum of a single pulse, whereas the modulation frequency increases with increasing delay τ between the two pulses. Assuming a spectral resolution of 0.05 nm at 750 nm it follows that a delay

$$\tau = 1/\Delta f = \left[c\left(\frac{1}{750\,nm} - \frac{1}{750.05\,nm}\right)\right]^{-1} = 37.5\,ps$$

corresponding to 11 mm difference of optical path length in an interferometric setup can still be detected.

A prerequisite for the observation of modulated spectra as shown in Fig. 22 b) and 22 c) is that the intensities of the two interfering laser pulses are of the same magnitude. Reducing the intensity of the more intense laser pulse by inserting a neutral density filter into the beam, e.g. with filter wheel FW4 in Fig. 19, is not a solution, since this filter would introduce additional group delay. Instead, the intensities are balanced by adjusting aperture A2 in Fig. 19. Closing aperture A2, however, slightly steers the beam path. Therefore, the spatial overlap of both laser beams at the position of target T2 is adjusted by moving in a neutral density filter with filter wheel FW4 and observing the image of the two foci on CCD camera CCD3 (Fig. 22 a).

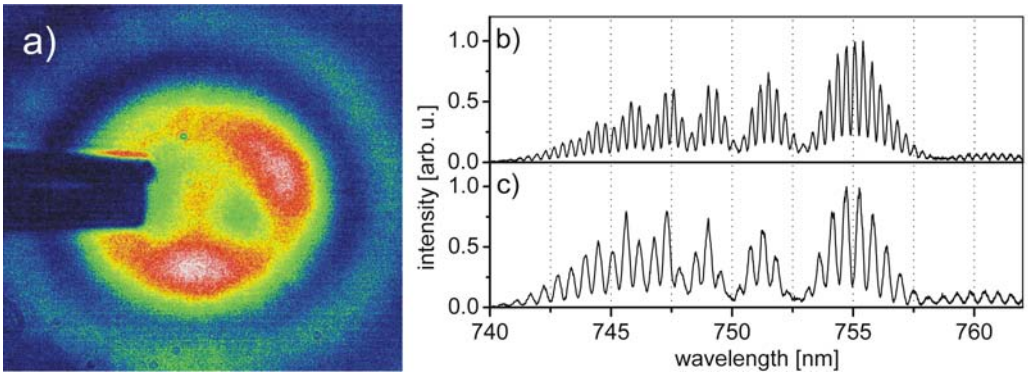

Fig. 22: a) Spatial interference with the shadow of the gas nozzle, b) and c): spectral interference of two fundamental laser pulses for $\tau = 5.4$ ps (b) and for $\tau = 3.5$ ps (c).

4.1.4 Active stabilization of the Mach-Zehnder interferometer

In the past, attosecond pump-probe experiments have been realized in collinear [7,68] and in Mach-Zehnder [28, 69] interferometer setups. Pump-probe experiments with a temporal resolution on an attosecond timescale in an interferometer setup require nm-scale relative stability of the optical beam path lengths of the two paths since temporal delays between the pump and the probe pulse are set by controlling the difference of the optical path lengths of both pulses. This can be ensured by an active feedback stabilization of the interferometer [69, 70], where the error signal is acquired in a reference interferometer. This reference interferometer is formed by half-inch optical components mounted on top of those forming the XUV-IR interferometer. By attaching the components on the mounts that support the XUV-IR interferometer we ensure that the behavior in terms of drift of the reference beam paths exactly mimic the drift motion of the beam paths of the fundamental and XUV laser pulses, which are used in the actual experiment. The thermal stability of the whole interferometer setup benefits from the use of stainless steel for most of the components, due to its small thermal expansion coefficient in comparison with e.g. aluminum. In the following, the two beam splitters mounted on the two perforated mirrors are called BS1 and BS2. The half inch mirrors of the upper reference interferometer, which are the little brothers of ML, M3 and M4 in Fig. 19, are called stabilization mirrors SML, SM3 and SM4, respectively. A continuous-wave (cw) laser beam of a low noise, vacuum compatible diode laser (ULN diode laser, Coherent) is split into two beams by BS1, which is mounted on the mirror mount of PM1 in Fig. 19. Both beams are recombined by a second half inch beam splitter BS2, which is mounted on the mirror mount of PM2. The beam, which is transmitted by BS1, propagates above the beam path of the high harmonics beam and is reflected by a half inch mirror SML attached on the mirror mount of ML in Fig. 19. Since M3 in Fig. 19 is used for controlling the delay between the fundamental laser pulse and the XUV laser pulse, M3 is not directly coupled with the reference interferometer. Instead, the mirror mount of M3

is mounted on a piezo translation stage PZT1. PZT1 and the stainless steel post, on which the mount of the half inch mirror SM3 of the reference interferometer is mounted, are assembled on the same base plate. M4 and SM4 are mounted on a second piezo translation stage PZT2 (NanoX200CAP, Piezosystem Jena), which is used for the active stabilization of both the lower interferometer and the upper reference interferometer.

After BS2, the intensity of the interference between both cw beams of the reference interferometer is measured by means of a small active surface photodiode (silicon pin detector ET-2000, EOT). It is operated in photoconductive mode with an active area of only 80 x 80 μm^2 in order to avoid averaging over several interference fringes. A change of the intensity measured by the photodiode corresponds to a change of the difference of the optical paths lengths of the two paths of the Mach-Zehnder interferometer. Therefore, the photodiode voltage was stabilized by means of a PID-algorithm written in LabVIEW and controlls the voltage, which sets the position of piezo translation stage PZT2. The PID-algorithm performs 400 corrections per second of the position of PZT2. The limiting factor for the speed of the active stabilization is the resonance frequency of PZT2 at approximately 500 Hz in case of a mass load of only 55 g for the mirrors M4, SM4, and their mounts. Therefore, only slow drifts due to thermal expansion of the breadboard, mirror mounts, etc. can be compensated but not fast vibrations introduced by e.g. turbo molecular pumps. Such fast vibrations have been efficiently suppressed by using dampers between the turbo molecular pumps and the walls of the vacuum chambers, by a decoupling of the walls of the chamber and the optical table inside the delay chamber on which the interferometer is mounted, and by using turbo molecular pumps with magnetic bearings.

In order to test the quality of the coupling between both interferometers, a second cw laser was set up in the HHG chamber and propagated through the lower interferometer from the focus for HHG in the HHG chamber all the way up to the focus in the experiment chamber. The focus in the experiment chamber was imaged outside on a second photodiode identical to the one used for the reference interferometer in the delay chamber. Figure 23 a) shows the relative change of the optical path lengths in both the upper reference interferometer and the lower interferometer, which has to be actively stabilized. This measurement proves, first, that both interferometers are coupled with an accuracy of less than 15 nm and, second, that the observed long-term drift motion of more than 100 nm is not negligible and has to be compensated by means of an active stabilization.

Before the active stabilization is started and after the stabilization is stopped, PZT2 is moved linearly over a distance of several microns in order to generate some fringes, which are detected by the photodiode of the reference interferometer in the delay chamber. These fringes serve as a calibration for the calculation of the changes of the path length from the measured photodiode voltages. The linear change of the photodiode voltage at the points of inflection of the sinusoidal curve is extrapolated to the minima and maxima and the photodiode voltage and converted to a path length change assuming a distance of $\lambda/2$ between adjacent extrema of the sinusoidal voltage curve. After this

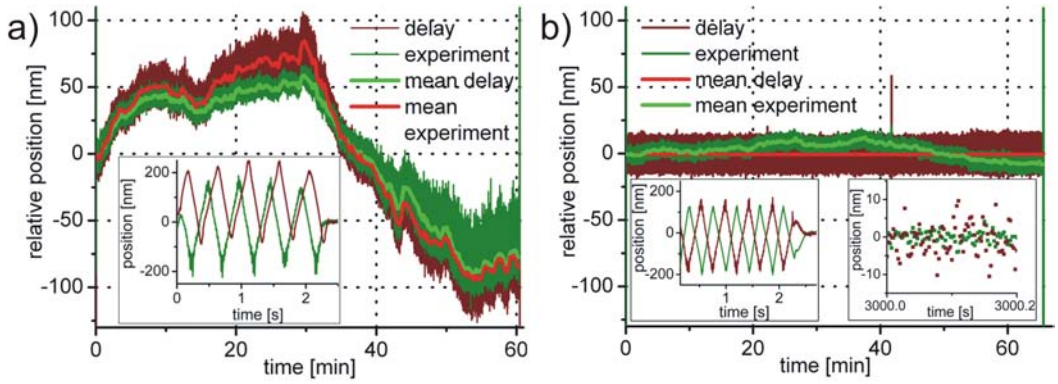

Fig. 23: a) relative change of the optical path length of the reference interferometer (delay, red) and the lower interferometer, which has to be stabilized (experiment, green). The thick red and green lines show the mean value per second of both interferometers. b) The same as in a) except that the active stabilization was turned on. The insets show the calibration by means of a linear movement of the piezo stage PZT2 before the active stabilization is started (see text). The right inset in b) illustrates the statistical noise of 80 data points.

calibration, the sinusoidal voltage curve changes to a zigzag curve as stipulated by the linear movement of PZT2 (see inset of Fig. 23 a) and b)).

Fig. 23 b) shows the same measurement as displayed in Fig. 23 a) in case of active stabilization of the Mach-Zehnder interferometer. It proves the capability of the presented stabilization scheme to suppress long term drift motions of the interferometer paths to within 50 attoseconds on a time scale of one hour. The residual drift motion of the IR-XUV interferometer, which is shown in Fig. 23, might be due to imperfect coupling of both interferometers. For time intervals of one second, which is usually the minimum integration time for the data acquisition of e.g. photoelectron spectra, the standard deviation has been calculated in case of the lower interferometer. The mean value of all standard deviations per one-second-interval is only 1.8 nm which corresponds to 6.0 attoseconds and defines the short term stability of the Mach-Zehnder interferometer. Different electromagnetic shielding of the photodiodes and cables explains the different statistical noise for both interferometers.

4.2 Flexible waveform synthesis with ω+2ω-waveforms

As already introduced in chapter 3.1.1 the ω+2ω-method for the generation of continuous XUV spectra as the spectral manifestation of isolated attosecond laser pulses in the time-domain is presented in detail in this chapter, which is composed of 3 parts: The first part addresses the experimental concept, on which the generation of $\omega + 2\omega$-waveforms is based. The second part describes the theoretical design of the optical components. The third part deals with the conduction of the experiment, experimental results and their interpretation.

4.2.1 Concept for the generation of ω+2ω-waveforms

The experimental setup for the synthesis of $\omega + 2\omega$-waveforms consists of a β-BBO for SH-generation, an α-BBO as a so-called timeplate, which adjusts the delay between the fundamental and the SH light and a $\lambda/2$-waveplate, which turns the polarization of the fundamental by 90° and the one of the SH by 180° into one plane for HHG:

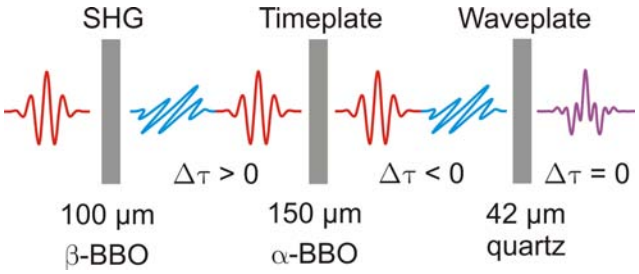

Fig. 24: Schematic view of the ω+2ω-setup, the laser beam propagates from the left to the right.

The following figure shows the orientation of the fundamental and second harmonic electric field polarization with respect to the optical axis in the β-BBO, timeplate and in the waveplate.

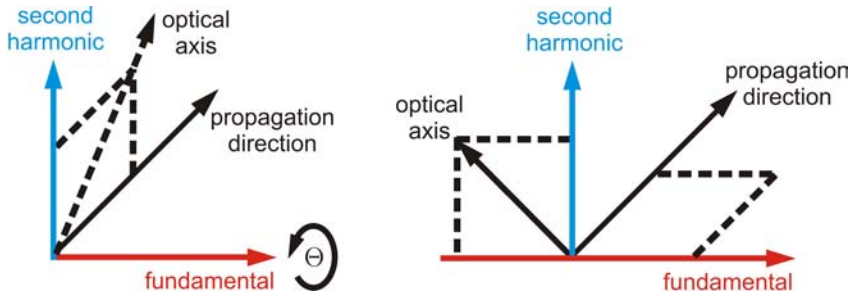

Fig. 25: 3-dim. orientation of fundamental and second harmonic electric field in the β-BBO and timeplate (left) and waveplate (right).

Criteria for the selection of all three components were

- the highest possible ratio of SH intensity to fundamental intensity
- the smallest possible thickness of each component in order to reduce the dispersion and therefore to maintain the short pulse duration.

The approach for the calculation of these components was as follows:

- First, β-BBO as a standard nonlinear crystal for SHG was selected due to its high damage threshold and conversion efficiency. The selection of a thickness of 100 μm was a tradeoff between increasing conversion efficiency and decreasing phase-matching bandwidth with increasing crystal thickness. The phase-matching cut-angle θ=29.2° was selected for the central wavelength of the fundamental pulse. Type I phase-matching was chosen since the perpendicular polarizations of SH and fundamental light are needed for the compensation of the the group delay with a so-called timeplate right after the BBO for SHG.
- Second, a suitable $\lambda/2$-plate, which turns the fundamental and SH polarization into the same plane was selected. Here, the most important criterion was its smallest possible thickness. For this purpose a true zero order waveplate made of crystal quartz with only 42 μm thickness was designed.
- Third, after calculating the group delay, which is introduced by the BBO for SHG and the waveplate, a suitable timeplate was selected, which causes the same group delay like the two previous components but with opposite sign. For this optical component a 150 μm thick α-BBO cut at θ=57° was chosen, since BBO exhibits a higher damage threshold in comparison to other possible materials like calcite and can be manufactured with a better surface quality.

4.2.2 Design of the optical components

The following equation shows the intensity $I_{2\omega}$ of the second harmonic, which is generated by a fundamental intensity I_ω in a birefringent material with length l, refractive indices $n_{2\omega}$ and n_ω and the nonlinear second order susceptibility $\chi^{(2)}_{ijk}$ [49]:

$$I_{2\omega} = I_\omega^2 \frac{\omega^2 Z_0 l^2}{2c_0^2 n_{2\omega} n_\omega^2} \left[\frac{\sin(\Delta k l/2)}{\Delta k l/2}\right]^2 \sum_{i=1,2} |\chi^{(2)}_{ijk} e_j e_k|^2 \tag{10}$$

Here, $Z_0 = \sqrt{\mu_0/\varepsilon_0}$ is the vacuum impedance, $k = 2\pi/\lambda$ the wavenumber and $\Delta k = k_{2\omega} - 2k_\omega$ the phase-mismatch.

In case of type I phase-matching with β-BBO the phase matching angle ϕ has to be 90° [46]. The phase-matching angle θ and the bandwidth BW(λ) of the frequency-doubled SH spectrum are given by

$$\cos^2\theta = \left(\frac{\frac{1}{n_{o,\omega}^2} - \frac{1}{n_{e,2\omega}^2}}{\frac{1}{n_{o,2\omega}^2} - \frac{1}{n_{e,2\omega}^2}} \right) \tag{11}$$

$$\mathrm{BW}(\lambda) = \frac{\sin^2(\Delta k l/2)}{(\Delta k l/2)^2}$$

$$\Delta k = k_{2\omega} - 2k_{\omega} = 2\pi \left(\frac{n_{2\omega}}{\lambda_{2\omega}} - \frac{2n_{\omega}}{\lambda_{\omega}} \right)$$

$$\frac{1}{n_{2\omega}^2(\theta)} = \frac{\cos^2\theta}{n_{o,2\omega}^2} + \frac{\sin^2\theta}{n_{e,2\omega}^2}$$

$$n_{\omega} = n_o.$$

Fig. 26 shows the calculated wavelength dependence of the phase-matching angle θ and the phase-matching bandwidth $\mathrm{BW}(\lambda)$ for three different thickneses l of β-BBO.

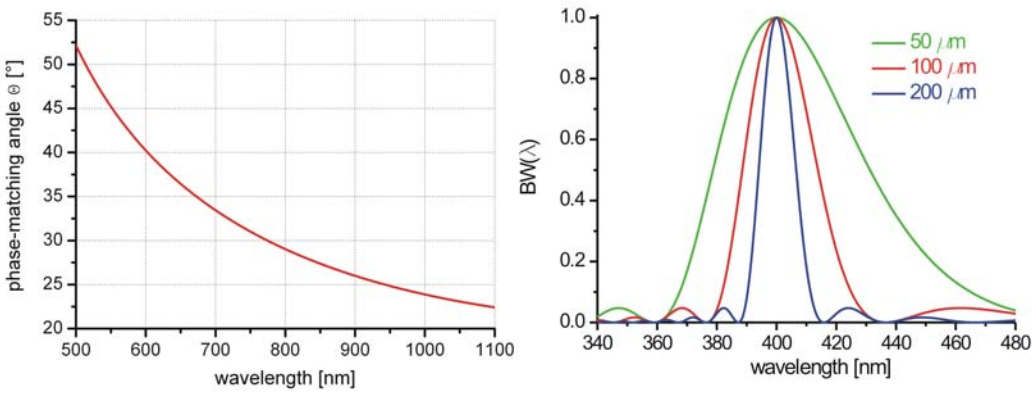

Fig. 26: Phase-matching angle θ (left) and phase-matching bandwidth $\mathrm{BW}(\lambda)$for three different thicknesses l of β-BBO.

The following Fig. 27 shows the calculated wavelength dependence of the group delay and the GDD for both fundamental and SH pulses after propagation through 100 μm of β-BBO:

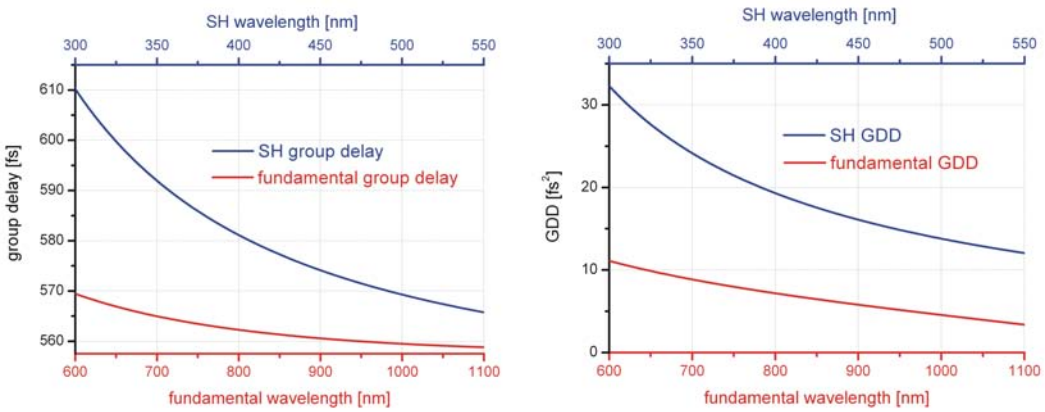

Fig. 27: Group delay $\Delta\tau$ (left) and GDD (right) for both fundamental (red curve) and SH (blue curve) after propagation through a 100 μm thick β-BBO, θ has been adjusted for phase-matching of the fundamental wavelength.

The thickness l of a so-called true zero order $\lambda/2$-waveplate is determined by the ordinary and the extraordinary refractive indices n_o and n_e:

$$\frac{2\pi}{\lambda} l |n_e - n_o| = \pi$$

Assuming a central wavelength of 760 nm for the fundamental pulse the thickness of a $\lambda/2$-waveplate made of crystal quartz is $l = 42.46$ μm. Due to the wavelength dependence of the refractive index a perfect $\lambda/2$-waveplate can only be designed for one single wavelength. In case of a broad spectrum the transmitted pulse will always be elliptically polarized. If this elliptically polarized pulse propagates through a polarizer adjusted to the polarization of the perfectly linearly polarized wavelength of 760 nm, then the normalized spectral transmittance T(λ) of this polarizer can be calculated according to the following formulas:

$$\mathrm{T}(\lambda) = \frac{1}{1 + \tan^2\left(\frac{\Delta\phi(\lambda)}{2}\right)} \tag{12}$$

$$\Delta\phi_\omega = \pi \left[1 - \frac{2l}{\lambda_\omega}\left(n_{e,\omega} - n_{o,\omega}\right)\right]$$

$$\Delta\phi_{2\omega} = 2\pi \left[1 - \frac{l}{\lambda_{2\omega}}\left(n_{e,2\omega} - n_{o,2\omega}\right)\right]$$

Derivation: In a cartesian coordinate system the ordinary axis is the x-axis and the extraordinary axis the y-axis. After propagation through the waveplate the electric $E(t)$ field can be described with the following vector:

$$E(t) = \begin{pmatrix} x(t) \\ y(t) \end{pmatrix} = \begin{pmatrix} \cos(\omega t) \\ \cos(\omega t + \Delta\phi) \end{pmatrix}$$

A change from this parametric representation to cartesian coordinates gives:

$$x^2 + y^2 - 2xy\cos(\Delta\phi) = \sin^2(\Delta\phi)$$

A prinicipal axis transformation gives:

$$x = \frac{1}{\sqrt{2}}(u - v)$$
$$x = \frac{1}{\sqrt{2}}(u + v)$$
$$\frac{u^2}{\sin^2(\Delta\phi)}\left[1 - \cos(\Delta\phi)\right] + \frac{v^2}{\sin^2(\Delta\phi)}\left[1 + \cos(\Delta\phi)\right] = 1$$

This is the equation of an ellipse. The ratio between its major and minor semi-axis is identical to the ratio between the two perpendicular polarization components $E_\perp$ and $E_\parallel$ of which only the latter one is transmitted through the polarizer behind the waveplate.

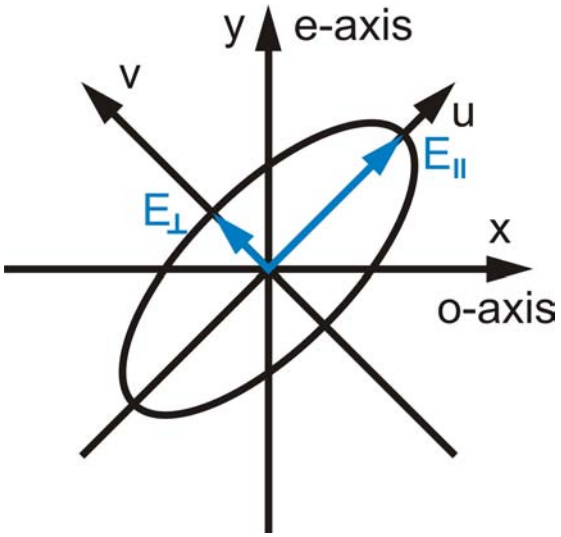

Fig. 28: Orientation of the two cartesian coordinate systems with axes x, y and u, v. The polarizer is set for maximum transmission of the electric field with polarization $E_\parallel$ and wavelength 760 nm. The ordinary and extraordinary axis are identical with the x- and y-axis.

For the corresponding intensities holds:

$$\frac{I_\perp}{I_\parallel} = \tan^2\left(\frac{\Delta\phi}{2}\right) \tag{13}$$

The total intensity I is given by

$$I = I_\perp + I_\parallel. \tag{14}$$

From eq. 13 and 14 follows eq. 12.

Fig. 29 shows the wavelength dependence of the intensity transmission $T(\lambda)$ through a polarizer behind the waveplate:

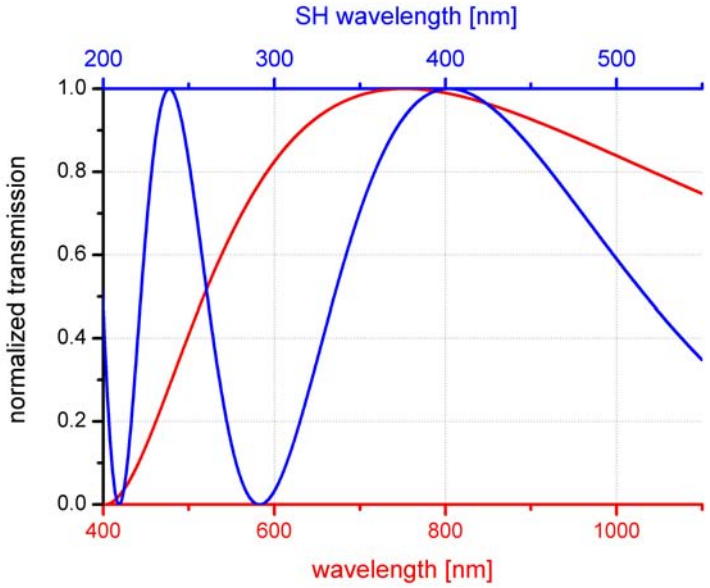

Fig. 29: Transmission $T(\lambda)$ of the fundamental (red) and the SH (blue) intensity through a polarizer adjusted for optimum transmission of the polarization $E_\perp$ at 760 nm.

Fig. 30 shows the group delay and the GDD for both fundamental and SH after propagation through a 42 μm thick $\lambda/2$-waveplate made of crystal quartz:

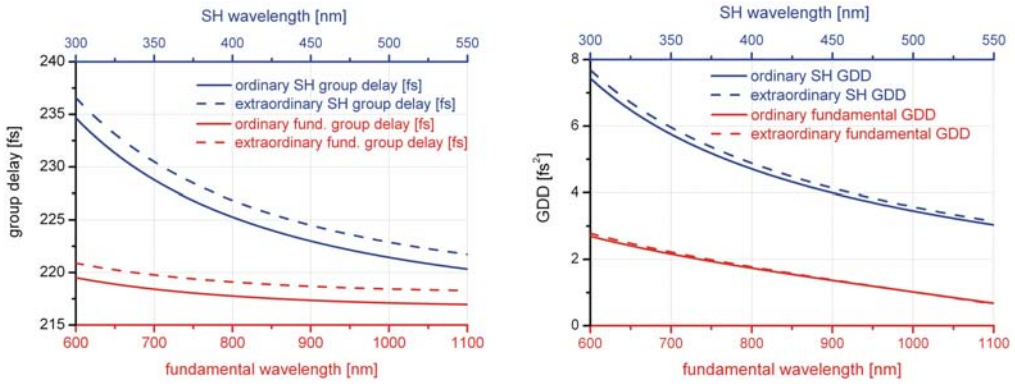

Fig. 30: Group delay $\Delta\tau$ (left) and GDD (right) for both fundamental (red curve) and SH (blue curve) after propagation through 42 μm thick crystal quartz.

In the following considerations the fundamental wavelength is set to 760 nm. The SH wavelength is set to 430 nm due to some experimental constraints, which will be explained in the next section. The group delay difference between the fundamental and the SH pulse after propagation through a 100 μm thick β-BBO crystal is according to Fig. 27

$$\Delta\tau_{\beta-\mathrm{BBO}} = +14.8 \text{ fs}.$$

If the group delay of the fundamental and the SH after propagation through the waveplate is defined as the mean group delay of the ordinary and the extraordinary wave then the waveplate introduces an additional group delay difference of

$$\Delta\tau_{\mathrm{waveplate}} = +6.4 \text{ fs}.$$

For temporal overlap after all three components, i.e. β-BBO, timeplate and waveplate, the timeplate has to introduce a group delay of

$$\Delta\tau_{\mathrm{timeplate}} = \text{-}21.2 \text{ fs}.$$

Fig. 31 shows the group delay difference

$$\Delta\tau_{\mathrm{timeplate}} = l\left(\frac{1}{v_{g,2\omega}} - \frac{1}{v_{g,\omega}}\right)$$

as a function of θ and the change of the phase delay

$$\frac{d\Delta\tau_P}{d\theta} = l\frac{d}{d\theta}\left(\frac{1}{v_{P,2\omega}} - \frac{1}{v_{P,\omega}}\right)$$

in a 150 μm thick α-BBO crystal:

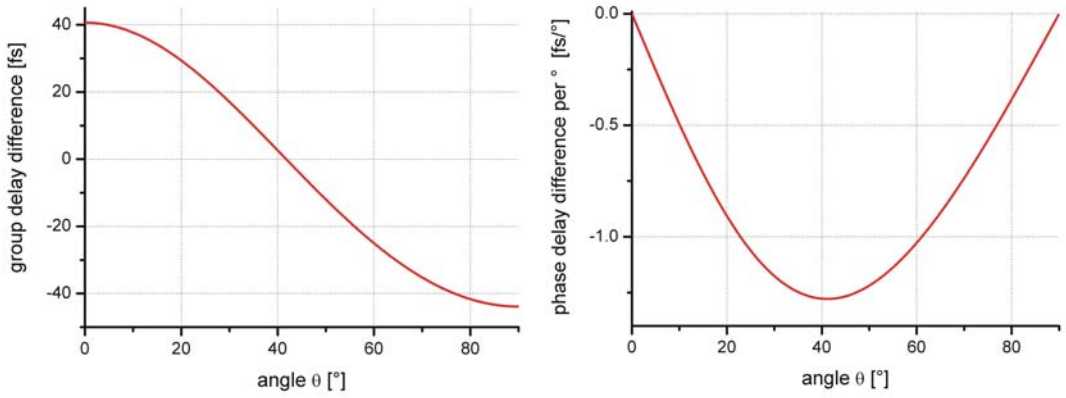

Fig. 31: Group delay difference $\Delta\tau_{\text{timeplate}}$ (left) versus cut-angle θ and first derivative of phase delay difference with respect to θ for a 150 μm thick α-BBO crystal.

From this follows that a 150 μm thick α-BBO crystal cut at $\theta = 57°$ introduces a suitable group delay difference between fundamental and SH of

$$\Delta\tau_{\text{timeplate}} = \text{-21.3 fs.}$$

The left graph in Fig. 31 shows that a change of θ by 1.0° corresponds to a relative phase shift between fundamental and SH wave of 1.1 fs at $\theta = 57.0°$.

The GDD, which is introduced by the timeplate at a cut-angle of $\theta = 57\ °$, is shown in the following Fig. 32:

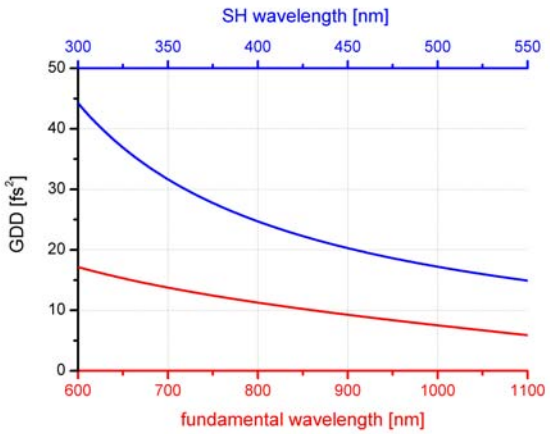

Fig. 32: GDD introduced by the timeplate for $\theta = 57\ °$.

4.2.3 Experimental results

Fundamental laser pulses were generated by a commercial laser system (Femtolaser compact pro, Femtolasers Produktions GmbH) as described in chapter 3.2 with 300 μJ pulse energy, 3 kHz repetition rate, stabilized carrier envelope phase and negative chirp in order to compensate the positive chirp, which was introduced by the subsequent optical components [10]. The fundamental spectrum supported a Fourier-limited pulse duration of 3.5 fs FWHM. Through an entrance window these laser pulses entered the vacuum system of the AS2 beamline as described in chapter 4.1. The setup for waveform synthesis and HHG, which is shown in Fig. 33, was installed in the HHG chamber of the AS2 beamline. The fundamental laser pulses were focused with a concave silver mirror M1 (ROC = -350 mm) and recollimated by a second concave silver mirror M2 (ROC = -350 mm). In the converging beam between M1 and M2 the β-BBO crystal was placed out of focus for second harmonic generation (SHG) at intensities just below its damage threshold. After recollimation both the fundamental and the second harmonic wave propagated through the timeplate, the half waveplate and four pellicles at Brewster's angle for polarization cleaning. The fundamental and the second harmonic were focused by a concave silver mirror M3 (ROC = -1000 mm) in a gas target with a backing pressure of 200 mbar of neon. The fundamental and second harmonic pulse energies in the gas target were measured to 180 μJ and 9 μJ, respectively. The substantial loss of pulse energy is attributed to Fresnel-reflections on the uncoated β-BBO, timeplate, waveplate and pellicles used for polarization cleaning in Brewser's angle of the fundamental wave. Silver coatings for all mirrors have been used due to the high reflectance in the spectral range of the fundamental pulse at the expense of a reduced reflectance for the SH pulse.

In order to achieve the highest possible reflectance the SH wavelength was set to 430 nm, leading to a detuned SH wave [71]. The spectral bandwidth of the SH pulses supported a Fourier-limited pulse duration of 13 fs. The generated high harmonics were transmitted through a 1.0 μm thick Zr foil and spectrally resolved with the grating spectrometer in the delay chamber of the AS2 beamline shown in Fig. 19 on page 41. High harmonics spectra have been recorded for different angles θ of the timeplate and different CEP settings of the fundamental pulse.

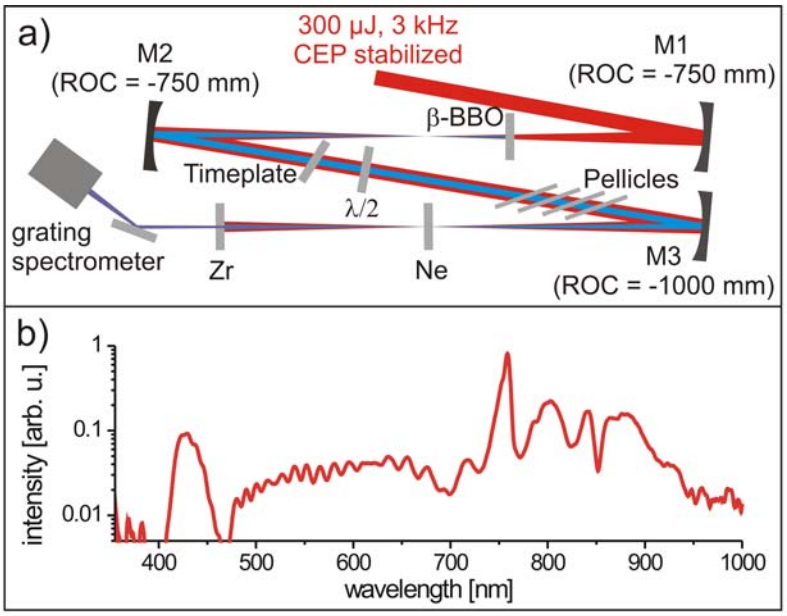

Fig. 33: a) Experimental setup for the synthesis of $\omega + 2\omega$-waveforms and high harmonic generation, b) generated driving waveform consisting of the fundamental spectrum centered at 760 nm and a detuned SH spectrum centered at 430 nm.

HHG generation was first optimized with the fundamental wave. Before HHG in the neon gas target the fundamental beam propagated through both the β-BBO crystal and the α-BBO crystal as well as through the waveplate and pellicles. The β-BBO crystal was placed 20 cm in front of the focus of the converging fundamental beam between mirror M1 and M2 in Fig. 33 a), where the fundamental intensity was too low for SHG due to the large fundamental beam diameter. The positive chirp caused by the β-BBO, α-BBO and the waveplate was compensated by introducing negative chirp with a pair of wedges placed after the hollow core fiber of the described laser system. This resulted in the shortest fundamental pulse duration in the neon gas target and the highest XUV photon flux after HHG.

After optimizing HHG with the fundamental only, the distance between the β-BBO and the focus between mirror M1 and M2 was decreased to 10 cm. Higher fundamental intensities due to the smaller beam diameter resulted in typical SHG conversion efficiencies of about 5 %. HHG was optimized again with the synthesized ω+2ω-waveform. The generated HH spectra showed a strong dependence on both the fundamental CEP, which is set by means of the active CEP stabilization of the described laser system, and the delay between the fundamental wave and the SH wave, which is controlled by changing the θ-angle of the timeplate (α-BBO). Changing the θ-angle of the timeplate by 1.0° at normal incidence of the laser beam results in a calculated phase delay of 1.1 fs between the fundamental carrier wave and the SH carrier wave. Since the fundamental wave is a pure ordinary wave in the timeplate and the second harmonic pulse is not a few-cycle pulse the CEP of both pulses is assumed to be constant during the timeplate scan. Therefore the change of the phase delay is approximately equal to the change of the group delay. A typical series of HH spectra at different delays ("timeplate scan") is shown in Fig. 34 a), which reveals a periodicity of 1.4 fs in perfect agreement with the period of the SH wave at 430 nm. The high harmonic spectra have been acquired in steps of $\Delta\theta = 0.01°$, which results in a delay resolution of 11 attoseconds. XUV photons with energies below 90 eV are strongly suppressed by the spectral transmission of the zirconium filter and the spectral efficiency of the grating as shown in Fig. 35 b). In the depicted energy range the spectral efficiency of the CCD detector is constant.

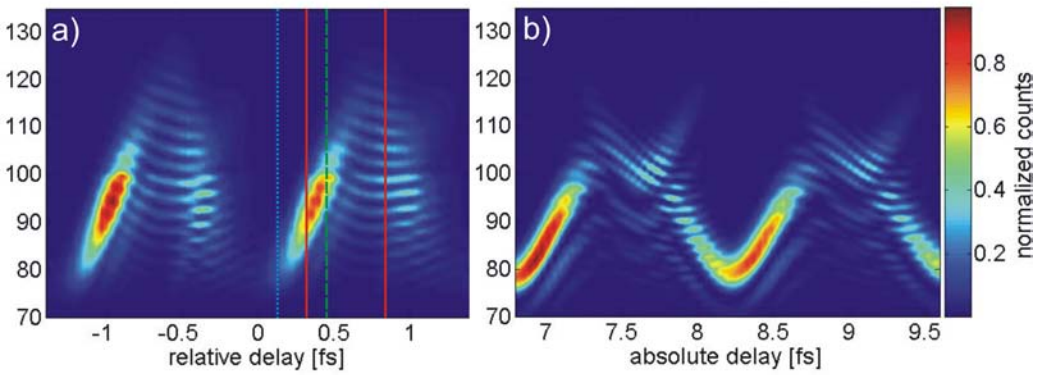

Fig. 34: a) Timeplate scan showing measured high harmonic spectra for different relative delays between the fundamental wave and the second harmonic wave. The selected high harmonic spectra of Fig. 35 are marked with vertical lines. b) Calculated high harmonic spectra assuming the experimental conditions of the timeplate scan in a) for different absolute delays t_0 according to eq. 15.

In general, all timeplate scans consist of one part with continuous XUV spectra at varying energies and a second part with modulated XUV spectra. Three XUV continua for

three different delays supporting Fourier-limited pulse durations of 161, 140 and 110 attoseconds FWHM are shown in Fig. 35 together with one modulated XUV spectrum, which demonstrates the resolution of the XUV grating spectrometer. Even harmonics appear in the modulated spectrum below 85 eV. The central photon energy of the XUV continua could be shifted from 80 eV to 100 eV by changing the phase delay by only 320 attoseconds.

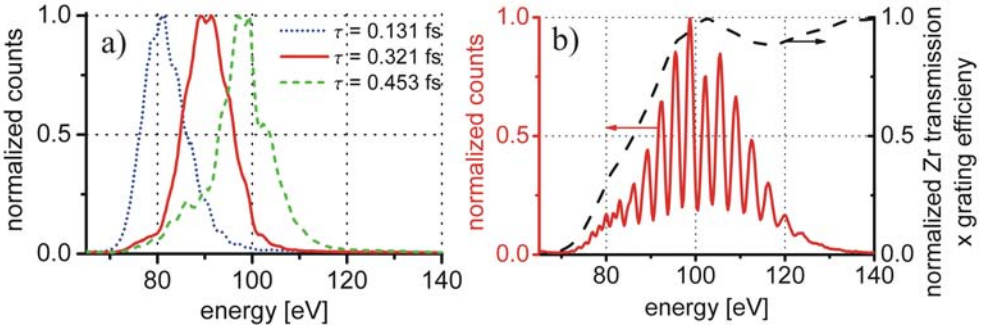

Fig. 35: XUV spectra taken from Fig. 34 a) for different delays τ: a) Continua tunable between 80 and 100 eV. b) Modulated XUV spectrum demonstrating the spectral resolution of the XUV spectrometer at $\tau = 0.844$ fs (solid curve). Even harmonics are visible below 85 eV. High harmonics at lower energies are suppressed by the Zr filter transmission and the calculated XUV grating efficiency (dashed curve).

Timeplate scans have been repeated for different CEP settings, which resulted in a shift of the XUV continua with respect to the delay axis. Changing the CEP by 2π led to identical timeplate scans. Changing the filter material from zirconium to aluminum and measuring timeplate scans below the aluminum absorption edge resulted in modulated XUV spectra as described in [72]. Even harmonics could only be observed at energies far below the cutoff of the high harmonic spectra, whereas an increasing SH pulse energy resulted in an increasing maximum photon energy of the observable even high harmonics.

A theoretical timeplate scan assuming the experimental conditions of the timeplate scan in Fig. 34 a) is presented in Fig. 34 b). The match between the two graphs appears to be fairly good. The theoretical scan was simulated by Ya Cheng and coworkers and is obtained using single-atom response HHG calculations in the framework of the strong field approximation [16]. Therefore, it naturally includes the contributions of both short- and long-trajectories (see chapter 3.1.1). The expression that was used for the superposition of the harmonic fields was

$$E(t)) = E\Big\{ \exp\left[-2\ln(2)\cdot t^2/\tau_1^2\right]\cos\left(\omega_1 t + \phi_1\right) + \sqrt{R}\exp\left[-2\ln(2)\cdot (t-t_0)^2/\tau_2^2\right]\cos\left(\omega_2(t-t_0) + 2\phi_1\right)\Big\} \tag{15}$$

where E is the electric field amplitude of the fundamental wave and $\sqrt{R} = E_{\omega_2}/E_{\omega_1}$ is the ratio of the field amplitudes of the second harmonic and fundamental waves. τ_i, ω_i and ϕ_i are the pulse durations (FWHM of electric field intensity), angular frequencies and carrier-envelope-phases of the fundamental wave (i=1) and its second harmonic (i=2). t_0 is the time delay between the fundamental wave and its second harmonic. High harmonic spectra are obtained by performing the Fourier-transform of the acceleration of the dipole moment. In this simulation, the laser intensity of the fundamental pulse amounts to $4.7{\cdot}10^{14}$ W/cm^2, and the ratio of the fundamental and second harmonic field amplitudes is chosen to be $\sqrt{R}$=4. The central wavelengths of the fundamental wave and its second harmonic are set at 800 nm and 430 nm, respectively. The pulse duration of the fundamental wave is set at 3.5 fs, while the pulse duration for the second harmonic wave is set at 15 fs. The fundamental CEP ϕ_1 was set at 220°. The calculated synthesized waveform, which generates the continuous high harmonic spectrum of Fig. 34 b) at an absolute delay of 6.9 fs is shown in Fig. 36. A further analysis in Fig. 36 b) reveals, that only high harmonics, which are generated during one half cycle, contribute to the intense XUV continuum, leading to the formation of an isolated attosecond pulse. Other half cycles do not contribute since either their ionization probability is too low or their XUV photon energy is reduced.

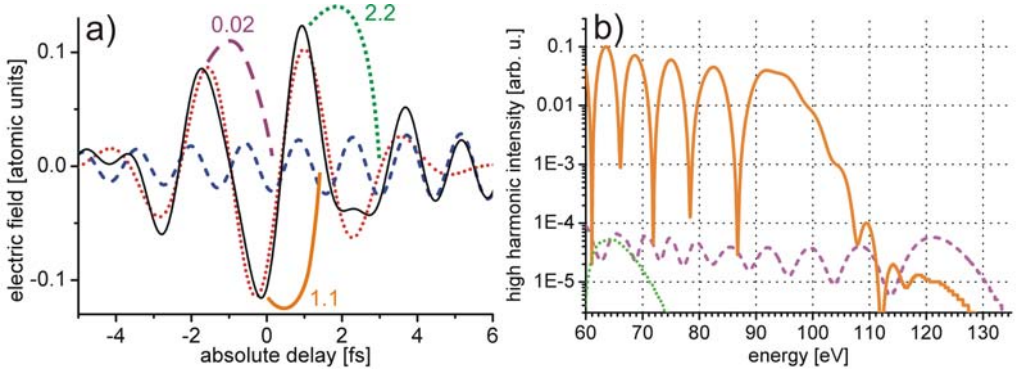

Fig. 36: a) Calculated waveforms of the fundamental (red dotted line), the second harmonic (blue dashed line) and their superposition (black straight line) at an absolute delay of 6.9 fs. Classical trajectories of maximum return energy and their ionization probabilities in units of 10^{-4} are also indicated. b) Calculated high harmonic spectra generated by the corresponding electron trajectories.

Calculations showed that HHG with ω+2ω-waveforms and longer fundamental pulse durations using the same intensity ratio $\sqrt{R} = 4$ results in comparable photon energies for

both even and odd harmonics, which prevents the formation of tunable XUV continua. Therefore we identified sufficiently short fundamental pulse durations as a prerequisite of this so far unique method for the generation of tunable attosecond pulses.

In conclusion, a powerful method for the generation of tunable isolated attosecond pulses was developed. In combination with the broadband metal-coated XUV mirrors presented in chapter 4.5 this technique has the potential for a tremendous simplification of future attosecond experiments. In the past, attosecond experiments in selected XUV spectral ranges were only possible by design, coating and alignment of tailored XUV multilayer mirrors for each XUV energy. Therefore, an efficient investigation of phenomena depending on the XUV photon energy, e.g. a comparison of fundamental processes like resonant and non-resonant photoemission from an atomic system, was either extremely time-consuming or rather impossible. The invention of metal-coated XUV mirrors in combination with the presented tunable XUV source brings attosecond physics close to the point, which femtosecond science has already reached 13 years ago by the development of convenient sources for tunable femtosecond laser pulses [73].

4.3 Intensive few-cycle pulses in the DUV

4.3.1 Motivation

The motivation for the generation of the shortest possible laser pulses in the deep ultraviolet (DUV), which is presented in this chapter, has to be seen in the framework of time-resolved measurements of electron dynamics in molecules on an attosecond timescale. Electronic dynamics in molecules will be initiated by a pump pulse and the unfolding evolution on an attosecond time-scale will be probed by an XUV pulse offering the corresponding temporal evolution. A condition for the feasability of such an experiment is a sufficiently high absorption cross section of the relevant molecular system in the spectral range of the pump laser pulse. For an easier theoretical handling of the achieved experimental results a molecular system containing only a limited number of atoms would be preferable. A further constraint given by the setup of the AS2 beamline as described in chapter 4.1 is that the molecular system under scrutiny should be gaseous or at least exhibit a sufficiently high vapour pressure. Unfortunately, there exist not many molecules with a high absorption cross section in the third harmonic spectral range of the fundamental driver pulses generated by the laser system, which has been described in chapter 3.2. Some promising candidates are presented in Fig. 37.

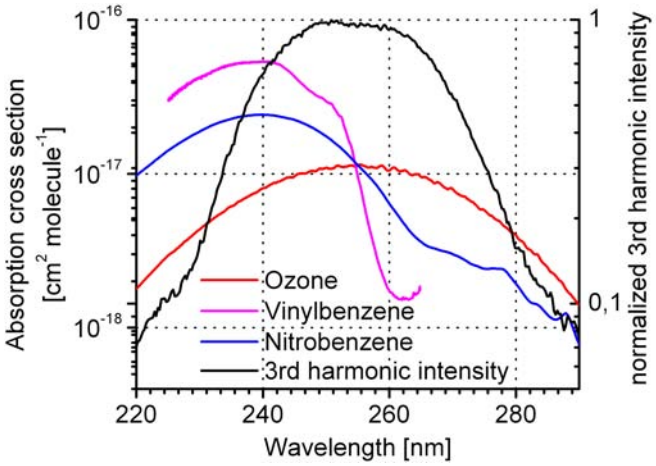

Fig. 37: Comparison of molecular absorption cross sections with the third harmonic spectrum of the generated UV pulses [74].

Since electron dynamics evolve in general on an attosecond time scale a UV pump pulse of shortest possible pulse duration would be favourable. Due to the rather small absorption cross sections presented in Fig. 37 the UV pulse energy should be high enough in order to excite a substantial percentage of the molecular ensemble.

At the beginning of this work existed no experimental technique for the generation of such high energetic and short laser pulses in the UV. The generation of the shortest

possible UV pulses was so far limited to methods using SHG and subsequent SFG in solids and gas filamentation setups [75–78]. Furthermore these methods are based on rather complicated setups for pulse generation and subsequent pulse compression. In the following a new technique for the generation of UV pulses with a pulse duration of 3.7 fs, a central wavelength of 266 nm, a pulse energy of 1 μJ and a repetition rate of 3 kHz is presented [11].

4.3.2 Experimental setup

The setup for the generation and characterization of sub-4-fs laser pulses is shown in Fig. 38. Fundamental laser pulses generated by the laser system described in chapter 3.2 are focused in a gas target consisting of a nickel tube filled with neon. Except for the comparatively high backing pressure of up to 6 bar this method is the same like the one used for HHG. Neon as nonlinear medium has been selected as a tradeoff between polarizability and plasma generation at fundamental intensities of 10^{14} W/cm^2. From helium to xenon the third order polarizability given by $\chi^{(3)}$ in equation 1 on page 11 is increasing resulting in an increasing conversion efficiency from fundamental light to its third harmonic. On the other hand, from helium to xenon the first ionization energy is decreasing, which gives rise to increasing ionization and plasma generation at the mentioned fundamental intensity. Since the generated plasma prevents phase-matching as a condition for efficient harmonic generation, plasma generation has to be limited.

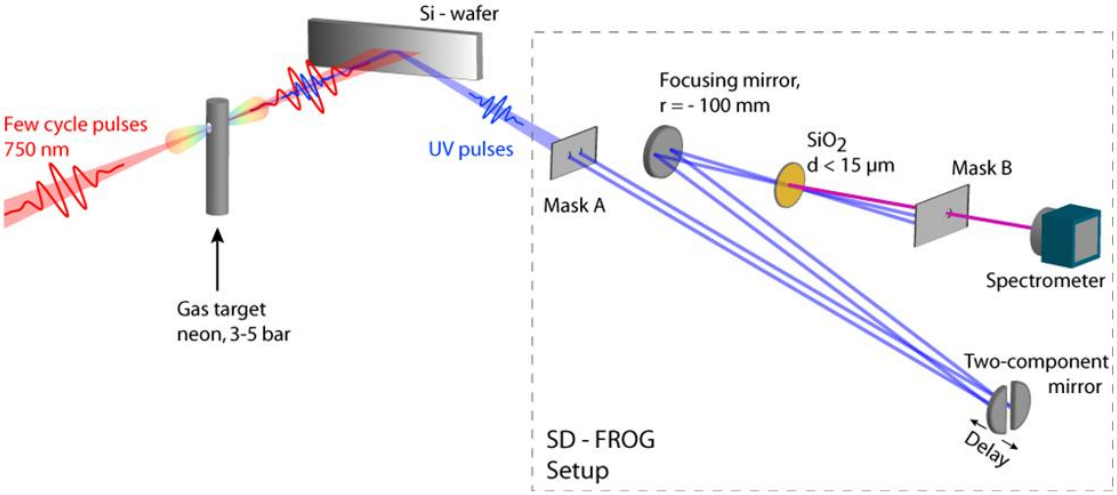

Fig. 38: Experimental setup for the generation of characterization of few-cycle UV pulses [11].

For a characterization of the generated 3rd harmonic pulses they have to be separated from the remaining much more intense fundamental light. This takes place in a non-dispersive way, preserving the short pulse duration of the UV pulses, by means of a

silicon surface upon which the third harmonic is reflected at Brewster's angle of the fundamental light. Since Brewster's angle is wavelength-dependent, the third harmonic exhibits a reflectance of 40 % at Brewster's angle of the fundamental radiation.

After the isolation of the UV pulses from the fundamental light they enter a dispersionless SD-FROG setup for pulse characterization [79]. SD stands for self-diffraction and describes a third-order nonlinear effect as introduced in chapter 3.1.1 [80]: two laser beams are temporally and spatially overlapped in a nonlinear medium. Due to the nonlinear Kerr-effect a modulation of the refraction index is generated resulting in a phase grating, which diffracts the two incident beams. Measuring the spectrum of the diffracted signal for different delays between the two incident beams results in a so-called FROG trace, which is shown in Fig. 39. The delay between the two laser beams is introduced by means of a split mirror upon which two replicas of the incident laser beam generated by a mask with two holes are reflected, whereas one of the two halfs of the split mirror is mounted on a piezo stage and can be moved with respect to the other half of the split mirror. Both beams are focused for different delays in a nonlinear medium made of a thin fused silica plate. The diffracted nonlinear signal is focused on the entrance slit of a spectrometer. Since third order self diffraction is not a phase-matched process [48], the thickness of the nonlinear medium has to be reduced to a minimum of only 15 μm. This ensured that the nonlinear medium had no substantial influence on the measured UV pulse duration [11]. However, the disadvantage of such a thin nonlinear material is an exceptional weak nonlinear signal.

4.3.3 Experimental results

A typical measured FROG-trace is shown in Fig. 39 a), which reveals that the red-shifted spectral components of the UV-pulse slightly precede the blue-shifted spectral components indicating positive chirp. As already demonstrated in chapter 4.4 a major advantage of FROG measurements becomes obvious: in contrast to an autocorrelation measurement a measured FROG trace tells the experimentalist immediately the sign of a potential chirp of the laser pulse. For a quantitative analysis a commercially available iterative FROG-algorithm is fed with the experimental data. Based on the assumption of a second order or third order nonlinear effect, which was in our case self-diffraction, this algorithm is able to reconstruct the electric field amplitude and phase in both spectral and time domain. Additionally it calculates a retrieved FROG trace shown in Fig. 39 b). The larger the difference between the measured and the retrieved FROG trace is, the larger is the error in the FROG measurement, giving the experimentalist a quantitative feedback regarding the quality of the measured data. However, in case of Fig. 39 a) and b) the retrieved FROG-trace nicely reproduces the residual positive chirp, which is visible in the measured FROG-trace. Fig. 39 c) and d) show the reconstructed electric field amplitude and phase in the time domain and in the spectral domain. The slightly parabolic shape of the spectral phase indicates positive chirp as defined in chapter 3.1.3, which is responsible for a pulse duration of 3.7 fs and therefore a bit longer than the Fourier-limited pulse duration of 3.5 fs supported by the measured spectrum of the UV

pulses.

To date, these measurements represent the shortest laser pulses in the spectral range between 200 and 300 nm. Due to the high pulse energy of about 1 μJ, these pulses can be used for triggering electronic dynamics of various molecular systems, which are subsequently probed by attosecond laser pulses with detection techniques as introduced in chapter 2.

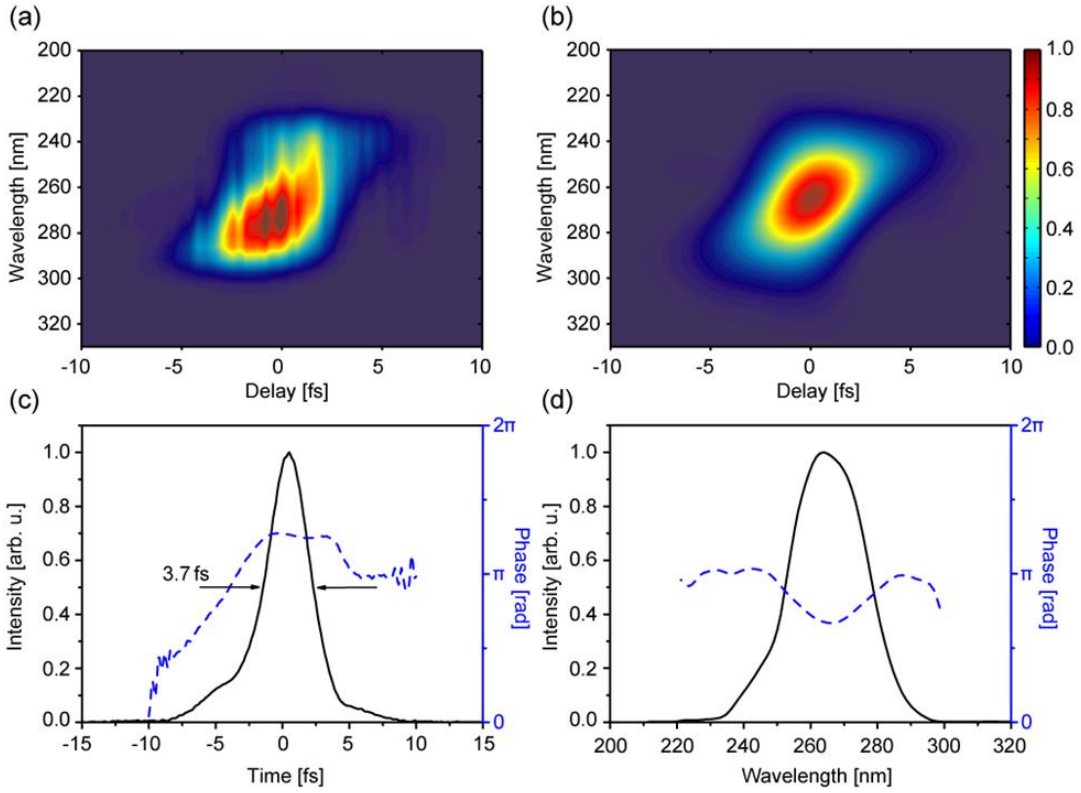

Fig. 39: a) Measured SD-FROG-trace of a 3.7 fs pulse in the DUV, b) Retrieved SD-FROG-trace, c) Retrieved electric field intensity and phase in the time domain, d) Retrieved electric field intensity and phase in the spectral domain [11].

4.4 Chirp control of attosecond laser pulses

4.4.1 Introduction

The invention of chirped multilayer mirrors revolutionized the generation of ever shorter femtosecond laser pulses in the visible and near infrared spectral range [54]. Up to now, multilayer mirrors as reflective optics in the XUV have been designed in order to achieve the highest possible reflectance, the broadest possible spectral bandwidth and the smallest possible GDD in order to preserve the phase of the incident attosecond laser pulses. The specific introduction of additional GDD by means of XUV multilayer mirrors for effective chirp compensation of the attosecond laser pulses as it is routinely done since more than 15 years in the generation of visible and near infrared femtosecond laser pulses was not pursued so far. At the latest with the breakage of the 100 as barrier [7] it was realized, that the generation of even shorter attosecond laser pulses will only be possible by a control of the chirp of the XUV pulses. In principle, the intrinsic positive chirp of the attosecond laser pulses caused by HHG with short trajectories as described in chapter 3.1.1 could be compensated by introducing negative chirp with thin metal filters, which are anyway used as high-pass filters, that transmit only the continuous part of the HH spectrum [7, 28]. But first, these filters absorb a substantial part of the only partially transmitted XUV continuum and second, their thickness ranges around 100 nm, which cannot be set precisely enough. Therefore the demonstration of chirped XUV multilayer mirrors is an important contribution to the future generation of attosecond laser pulses with pulse durations far below 100 attoseconds.

As a proof-of-principle experiment, streaking measurements have been performed with three different XUV multilayer mirrors: a first mirror, which introduces a GDD close to zero, a second mirror, which introduces negative GDD and a third mirror, which introduces positive GDD. In all measurements, which are shown in this chapter, negative delays mean that the XUV pulse comes first, i.e. precedes the fundamental femtosecond pulse. In contrast to other attosecond beamlines [7,68] the multilayer mirrors used in the AS2-beamline are flat (see chapter 4.1) and can be easily exchanged without any subsequent time consuming realignment of the complete setup. Therefore, the AS2-beamline is a unique setup for the complete characterization of multilayer XUV optics in terms of reflectance and phase.

The results for the three different XUV multilayer mirrors are presented in the following way: First the theoretical reflectance curve and GDD for each mirror are shown, which are based on calculations that have been done by Michael Hofstetter and coworkers. These theoretical predictions are examined by means of streaking experiments performed by the author and colleagues and a subsequent FROG analysis, which have been done by Justin Gagnon and coworkers. As a rule of thumb the observation of a chirped attosecond XUV pulse is visible by eye in streaking measurements if the absolute value of the GDD exceeds 5000 as^2. All experiments have been done at the AS2-beamline with active stabilization of the Mach-Zehnder-interferometer as a prerequisite for accurate streaking

measurements with attosecond resolution. These measurements demonstrate the successful stabilization of the interferometer setup in an attosecond pump-probe experiment. It also proves the exceptional quality of the streaking scans in terms of streaking amplitude, count rate and absence of distortions due to a short confocal parameter like in other attosecond beamlines [7, 68].

Due to the multilayer structure of XUV mirrors, spectral wings of the reflectance curve at lower and higher energies of the main peak cannot be prevented. Usually there are large phase jumps between adjacent wings of the reflectance curve. These phase jumps cause the formation of satellite pulses of an incident single attosecond pulse if the XUV spectrum of the incident pulse covers not only the main reflectance peak of the multilayer mirror but also one or several of these wings. All of these spectral wings at lower and higher energies of the main reflectance peak have to be suppressed. Low energy wings are usually suppressed by a metal filter, which is used for the absorption of low energy XUV photons that are generated during several half cycles of the driving fundamental field and therefore do not form one single attosecond pulse. High energy wings of the reflectance curve are suppressed by the cutoff of the XUV spectrum. That's why the general strategy in the planning of an experiment with XUV multilayer mirrors is usually the design of a multilayer mirror with a main reflectance peak that fits just between the absorption edge of a suitable high-pass filter and the cutoff of the generated XUV continuum. In the following XUV multilayer mirror designs the normalized transmission of the used high-pass filter - here 150 nm thick Pd - is included. The reflected XUV spectrum, which finally forms an isolated attosecond pulse is the product of the high-pass filter transmission, the multilayer mirror reflectance curve and the incident XUV spectrum from the HHG source. For this reason the reflectance curves, which are shown in the calculated mirror designs, cannot be compared with the spectral XUV intensity from the FROG retrieval, which additionally includes the incident XUV spectrum.

4.4.2 Multilayer mirror without chirp

Fig. 40 shows the design of an XUV multilayer mirror, which introduces the smallest possible chirp in the reflected attosecond pulse. The GDD oscillates around 0 as^2 and is well below an absolute value of 5000 as^2, so that in the streaking curve no visible chirp can be expected. In the reflectance curve the normalized transmission of a 150 nm thick Pd filter is included.

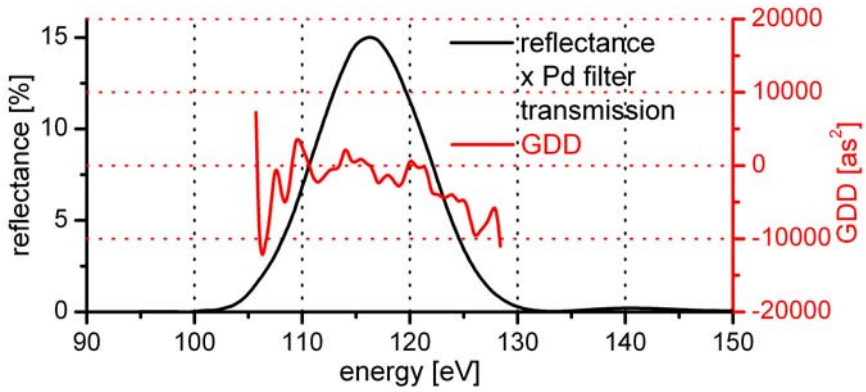

Fig. 40: Calculated reflectance and GDD of a multilayer mirror, which introduces a GDD close to zero [81].

Fig. 41 shows the streaking spectrogram, which has been measured utilizing an XUV multilayer mirror according to the design of Fig. 40. The streaking curve was measured with neon as target gas. With XUV photon energies above 100 eV there are two possible photoemission processes: photoionization via emission of a 2s electron or a 2p electron. The absorption cross section at 115 eV for the 2p electrons is by a factor of 10 larger than the one of the 2s electrons. Additionally, the 2p photoelectron count rate was increased by means of an electrostatic lens of the electron time-of-flight spectrometer. For this reason the streaking curve formed by the 2s photoelectrons is hardly visible and oscillates around electron energies of 70 eV, whereas the streaking curve of the 2p electrons is much more intense and oscillates around 95 eV. A small satellite pulse of the main attosecond pulse appears in the streaking curve of the 2p photoelectrons. This satellite pulse generates a second streaking curve shifted by π with respect to the streaking curve of the main attosecond pulse. The minima and maxima of this satellite curve do not show the same maximum count rate, since the minima of the 2p satellite curve coincide with the maxima of the 2s streaking curve and are additionally boosted by background photoelectrons at lower energies.

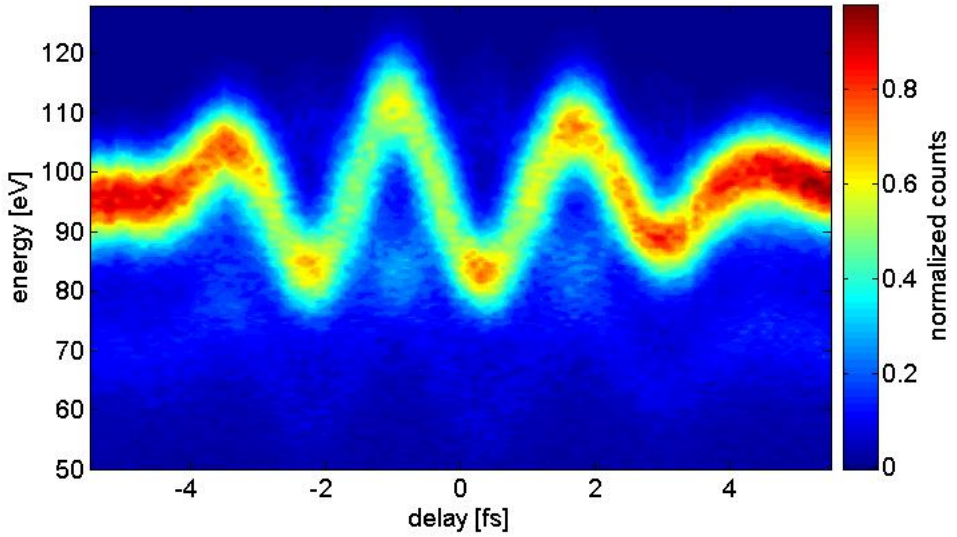

Fig. 41: Streaking curve with an unchirped XUV pulse.

Fig. 42 shows the spectral domain of the FROG retrieval result of the data in Fig. 41. The spectral bandwidth of the photoelectron spectra in Fig. 41 supports a Fourier-limited XUV pulse duration of 180 attoseconds. The retrieved XUV pulse duration is 188 attoseconds indicating a very small residual positive chirp of the attosecond pulse. This residual positive chirp can originate from the HHG process, the GDD introduced by the multilayer mirror and the palladium filter.

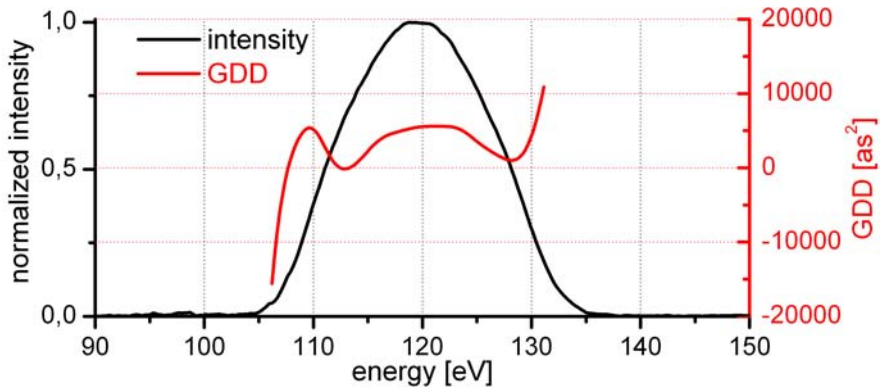

Fig. 42: FROG analysis of an XUV pulse with a chirp close to zero [82].

4.4.3 Multilayer mirror with negative chirp

Fig. 43 shows the design of an XUV multilayer mirror with negative chirp. This time the GDD, which is introduced by this mirror, oscillates around -15000 as^2. In comparison to the previous multilayer mirror the peak reflectance is reduced by a factor of 2 and the reflectance curve shows some wings of higher reflectance above 135 eV. Since the cut-off of the high harmonic spectrum is at 130 eV, these high energy wings of the reflectance curve cannot generate any satellite pulse.

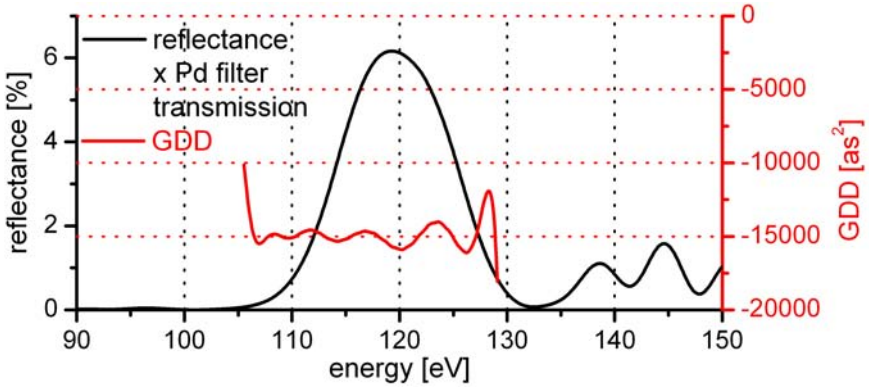

Fig. 43: Calculated reflectance and GDD of a multilayer mirror, which introduces a negative GDD [81].

Fig. 44 shows the streaking spectrogram, which has been measured with the XUV multilayer mirror designed according to Fig. 43. This time the spectral bandwidth and the maximum count rate of the photoelectron spectra shows a strong dependence on the sign of the slope of the measured vector potential curve. Parts with negative slope show a much broader spectral bandwidth and lower maximum count rate than parts with positive slope. This can be observed in the 2p streaking curve, for which the electrostatic lens of the electron time-of-flight spectrometer was optimized, as well as in the much weaker 2s streaking curve. As in the Fig. 41 a small amount of satellite pulse is visible in the spectrogram.

h!]

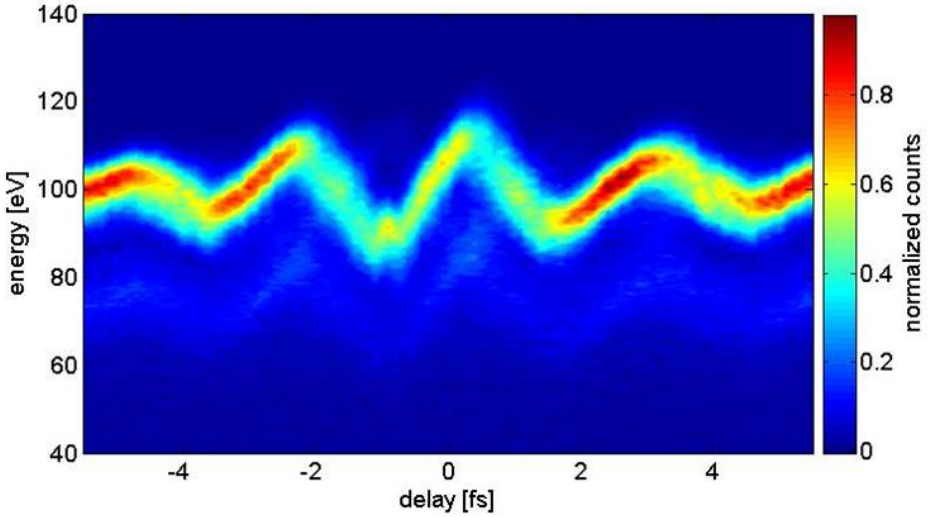

Fig. 44: Streaking curve with a negatively chirped XUV pulse.

The results of a FROG retrieval are depicted in Fig. 45. The retrieved GDD curve indicates a strong negative GDD oscillating around 15000 as^2, which reproduces surprisingly well within the measurement error the average GDD of -15000 as^2 of the design in Fig. 43. Such a large amount of negative GDD results in an XUV pulse duration far away from the Fourier-limit.

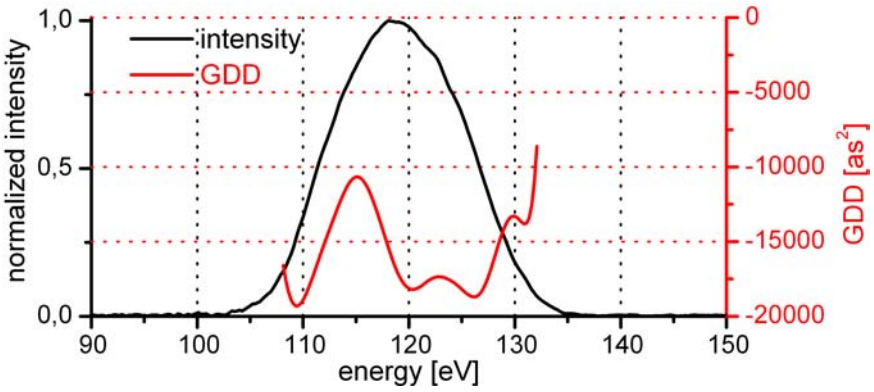

Fig. 45: FROG analysis of an XUV pulse with negative chirp [82].

4.4.4 Multilayer mirror with positive chirp

Fig. 46 shows the design of an XUV multilayer mirror, which introduces positive GDD. As in the case of the negatively chirped mirror the peak reflectance is reduced by a factor of 2 compared to the design of the multilayer mirror with minimum chirp in Fig. 40. The GDD curve oscillates around +15000 as^2. The wings of the reflectance curve above 135 eV are suppressed by the cutoff of the high harmonic spectrum at 130 eV.

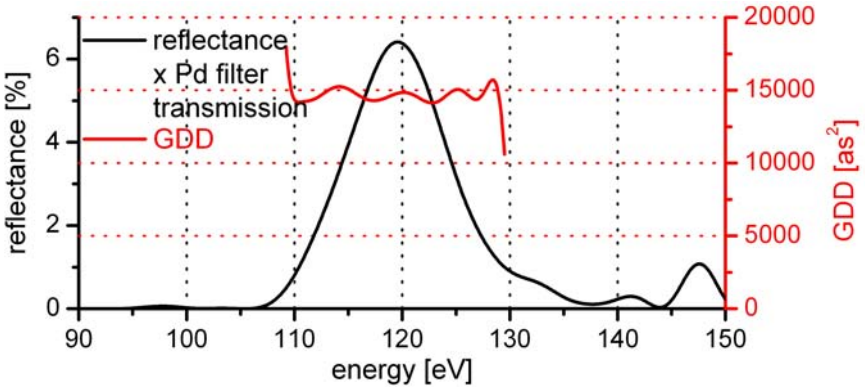

Fig. 46: Calculated reflectance and GDD of a multilayer mirror, which introduces a positive GDD [81].

Fig. 47 illustrates the corresponding streaking spectrogram, which shows the opposite behaviour of the spectrogram in Fig. 44: the parts of the vector potential with positive slope exhibit broader photoelectron spectra and a reduced maximum photoelectron count rate whereas the parts with negative slope show a larger maximum count rate and narrower photoelectron spectra. A FROG retrieval as shown in Fig. 48 of the data in Fig. 47 confirms the strong positive chirp of the design in Fig. 46.

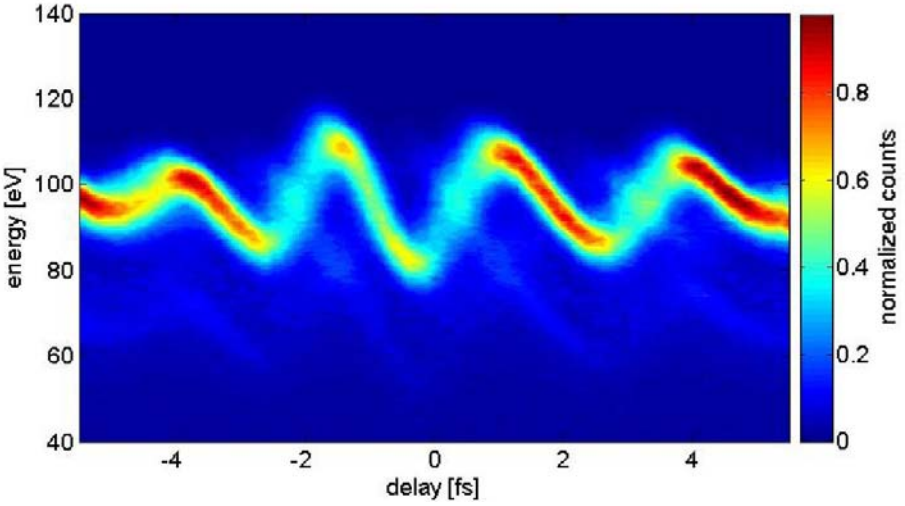

Fig. 47: Streaking curve with a positively chirped XUV pulse.

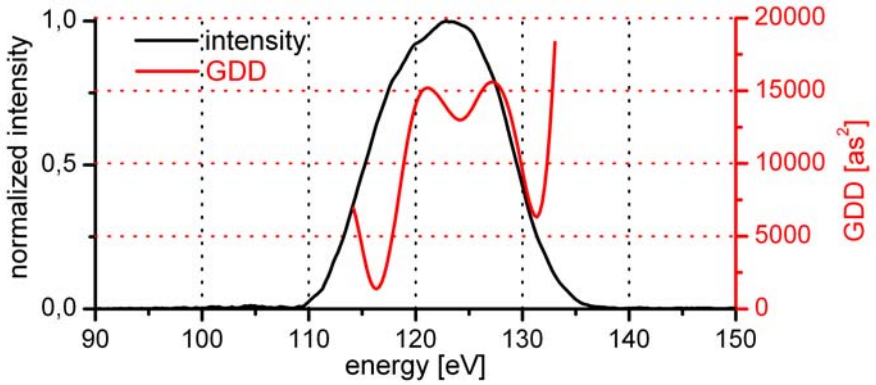

Fig. 48: FROG analysis of an XUV pulse with positive chirp [82].

4.5 Dramatically increased on target XUV flux

4.5.1 Metal-coated mirrors as reflective XUV optics

A fundamental challenge in research with extreme ultraviolet radiation is the lack of optics with sufficient reflectance. Apart from gracing incidence mirrors there exist no optics in the extreme ultraviolet, which offer reflectances comparable to those of silver-coated mirrors in the visible or gold-coated mirrors in the infrared. Therefore progress in experiments with attosecond laser pulses has always been compromised by the limited usability of gracing incidence optics [28, 69] or depended strongly on the development of suitable XUV multilayer optics [6]. At normal incidence the peak reflectance of state-of-the-art multilayer mirrors never exceeds 15%, if a spectral bandwidth of of more than 10 eV (FWHM) has to be reflected. The situation becomes even more complicated if very broadband reflectances of more than 20 eV are required. Such broadband XUV multilayer mirrors suffer from a peak reflectance of less than 5% [7]. Moreover, XUV multilayer mirrors suitable for attosecond laser pulses cannot be designed in any arbitrary spectral range, since the layers are made of different materials in order to modulate the imaginary part $Im(n)$ of the refractive index n. A standard material for XUV multilayer mirrors is silicon, which shows a strong absorption edge at 100 eV. Such an absorption edge causes strong phase effects preventing the preservation of the shortest possible pulse duration of the incident XUV pulses. In summary, even nowadays normal incidence XUV multilayer optics reveal a low reflectance, which is decreasing with an increasing reflected spectral bandwidth. On top of this, the reflected spectral bandwidth is limited and can only be designed in a few spectral windows of the XUV specrum.

All the difficulties with normal incidence XUV optics justify - besides other arguments, which have already been highlighted in chapter 4.1 - the invention of the AS2-beamline, since the angle of incidence of the XUV radiation on the XUV optic in the delay chamber in Fig. 19 on page 41 is 45° instead of normal incidence. On top of that, it turned out that multilayer XUV mirrors can be replaced by simple metal coated mirrors if several of these metal coated mirrors are sequentially used in order to increase the angle of incidence on each XUV-mirror. For example, three mirrors with an angle of incidence of 75° result in a total deflection of the XUV beam by 90° as required in the setup of the AS2 beamline.

This concept has been realized as shown in Fig. 49:

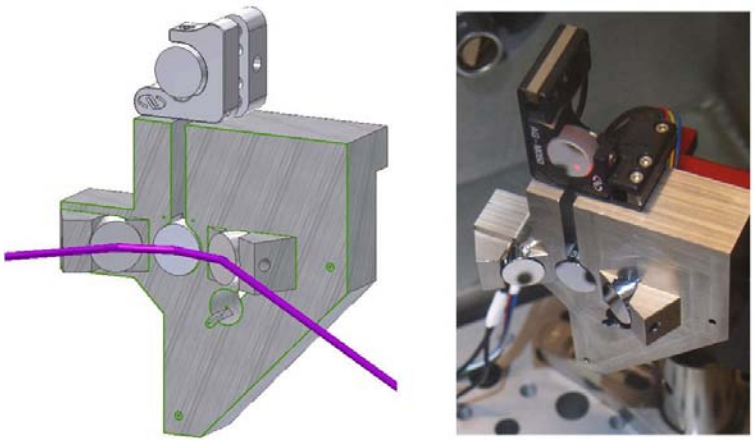

Fig. 49: left: design of a mirror mount, which deflects the XUV beam by 90° after 3 subsequent reflections at 75° angle of incidence, right: mirror mount for rhodium-coated XUV mirrors in the delay chamber of the AS2 beamline. The half-inch mirror on the top is part of the reference interferometer for the active stabilization of the Mach-Zehnder interferometer.

The spectral reflectance of metal coatings can easily be derived from the complex refractive index [29, 83]. In Fig. 50 the total reflectance after three reflections on metal coated mirrors at an angle of incidence of 75° is shown for ruthenium, rhodium and palladium [29]. All these coatings are commercially available and stable in air. In addition the reflectance curve of a normal incidence multilayer mirror is shown supporting a spectral bandwidth of about 25 eV (FWHM), which has been used for the generation of the shortest XUV pulses so far with a pulse duration of only 80 attoseconds [7, 81]. Apparently the application of metal coated XUV mirrors in the AS2 beamline allows an increase of the XUV flux on target by more than 2 orders of magnitude and an increase of the supported spectral bandwidth (FWHM) by a factor of 2. This invention opens the door to the generation of XUV pulses on target with pulse durations below 80 attoseconds at 100 times higher pulse energy. Another advantage of metal coated mirrors is that they preserve the phase of the XUV electric field, which is an important point, since many XUV multilayer mirror designs exhibit a useful spectral reflectance curve but cannot be used for the reflection of attosecond laser pulses due to disadvantageous phase effects.

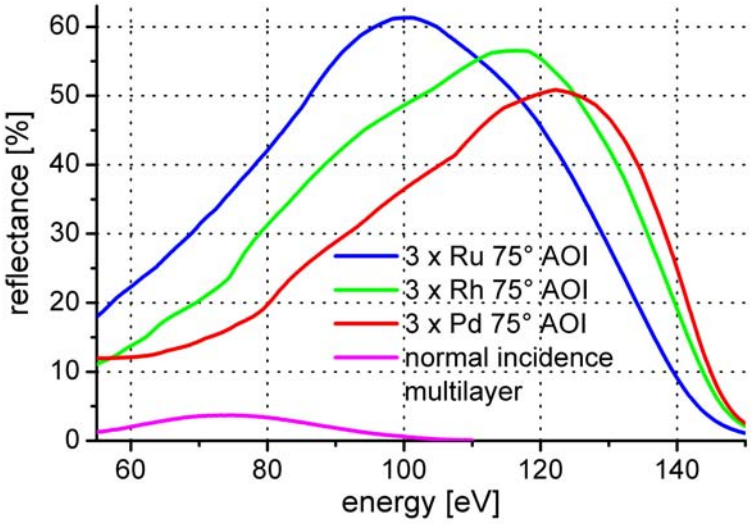

Fig. 50: Comparison of the total reflectance after 3 subsequent reflections on 3 metal coated mirrors at 75° angle of incidence and the reflectance at normal incidence of one multilayer mirror, which has been used for the generation of single XUV pulses with a pulse duration of 80 attoseconds [7].

4.5.2 Streaking measurements

A first streaking spectrogram with these novel metal coated XUV mirrors is shown in Fig. 51. In the past, all photoelectron spectra have been measured with a commercial electron time-of-flight spectrometer, which increases the acceptance angle of the emmitted photoelectrons by means of an electrostatic lens. Thus, it increases the photoelectron count rate by several orders of magnitude, which was a condition for the feasability of many attosecond experiments in the past due to the low XUV flux and absorption cross sections in the XUV. This lens supports only a limited spectral bandwidth of about 40 eV at a central energy of 100 eV. In case of 30 eV broad photoelectron spectra, which are streaked by additional 15 eV as shown in Fig. 51, this electrostatic lens fails since its supported spectral bandwidth is too small. Fortunately, by means of rhodium-coated XUV mirrors the XUV flux could be sufficiently increased so that streaking measurements at tolerable integration times per delay step are still doable. Rhodium as coating material in combination with a molybdenum filter were selected since rhodium shows the highest reflectance in the spectral range of the generated XUV continua between 80 eV and 120 eV. The shown streaking scan reveals a slight positive chirp of the XUV pulses. This positive chirp originates from the HHG with short trajectories as described in chapter 3.1.1 and is not completely compensated by the negative chirp introduced by the 150 nm thick molybdenum filter, which has been used as a high pass filter that transmits the continuous cut-off of the high harmonic spectrum (see Fig. 6 on page 18). The residual positive chirp of the XUV pulses could be compensated by a thicker metal filter, which

should result in a shorter attosecond pulse duration.

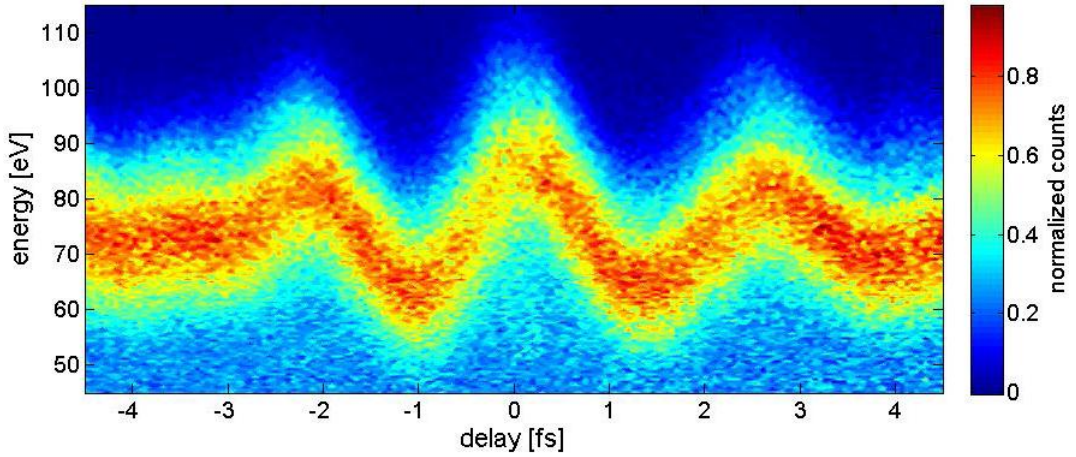

Fig. 51: Streaking scan with 150 nm Mo as spectral filter and rhodium mirrors. The integration time per delay step was 20 sec, the delay stepsize was 50 attoseconds.

Fig. 52 shows the temporal XUV intensity profile, which was retrieved by a FROG analysis of the streaking scan in Fig. 51. The XUV pulse duration is 77 attoseconds (FWHM).

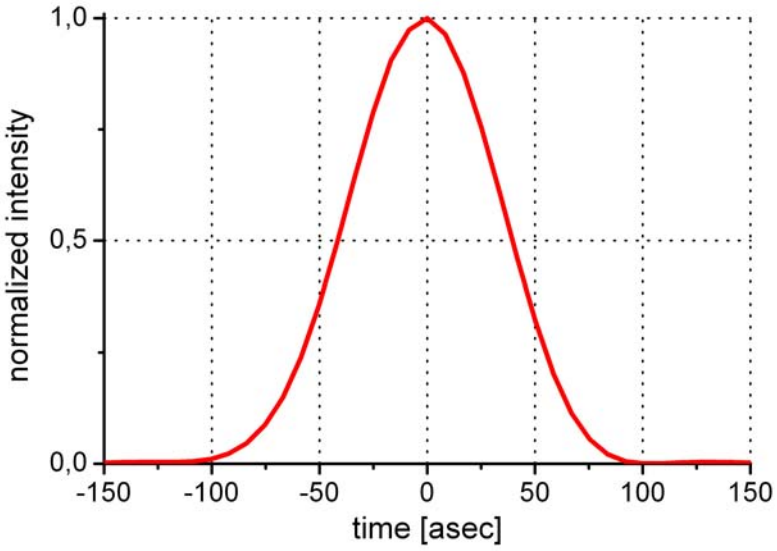

Fig. 52: Temporal XUV intensity profile retrieved from the streaking scan shown in Fig. 51.

5 Capturing electron dynamics

5.1 Time-resolved measurement of electron tunneling

5.1.1 Existing theoretical predictions and experimental results

Electron "tunneling" is a process where electrons get over a potential barrier, which they couldn't overcome in the classical picture if the energy of the electrons is not larger than the potential barrier. However, quantum mechanics predicts a limited probability for the transition of particles through a potential barrier even in case of particles with energies lower than the hight of the potential barrier. Therefore, the so-called "tunneling process" is a pure quantum mechanical process with no classical analog. The first theoretical description of electron tunneling processes in oscillating electric fields by Keldysh, which is one step of the HHG process (see Fig. 3), has been presented in chapter 3.1.1. An experimental approach for the time-resolved measurement of electron tunneling has been suggested by Brabec & Krausz [16] and was for the first time experimentally demonstrated by Uiberacker et al. [84].

In this experiment the XUV attosecond pulse acts as a pump pulse and the CEP stabilized few-cycle fundamental pulse as a probe. Since the photon energy in the order of 100 eV is much larger than the first ionization energy of all elements, an XUV photon can act in two different ways with an atomic system like a noble gas [84]:

- One photoelectron can be emitted from any electronic energy level with a binding energy smaller than the photon energy.
- One photoelectron can be emitted and one or more electrons can be promoted to higher energetic bound states. The photon energy is larger than the binding energy of the photoemitted electron plus the excitation energy of the promoted electron.

The first process can be regarded as a pure photoemission process, whereas the second process is a photoemission process accompanied by the electronic excitation of a second electron into a bound state, which is in general called a "shake-up" process. At the latest after the measurements, which will be presented in chapter 5.2, the widespread but experimentally unverified assumption that these two processes are instantaneous has to be discarded. In fact, these two processes appear to evolve on an attosecond time scale depending on the interaction of the photoemitted electron with all other electrons of the atomic system during the photoemission process. The subsequent relaxation dynamics of the electronically excited remanent ion, however, like e.g. Auger decays take place on a femtosecond [4] or picosecond timescale.

The pump-probe experiments, which are demonstrated in this chapter, proceed in the following way: The XUV pulse photoionizes neon atoms and generates electronically excited Ne^{1+} ions via various shake-up processes. The probing fundamental pulse allows the sufficiently excited bound electrons of the Ne^{1+} ions to leave the ion via electron tunneling as soon as the extrema of the fundamental electric field and the binding potential of the excited states form an adequate tunnel barrier according to Fig. 3 on page 13. The tunneling ionization of the excited electrons in the Ne^{1+} ions by means of the intense fundamental electric field results in the formation of Ne^{2+} ions. Since electron tunneling is only possible in the presence of a sufficiently strong fundamental electric field at the extrema of the fundamental waveform the integrated number of generated Ne^{2+} ions should increase stepwise with increasing delay between the XUV pump pulse and the fundamental probe pulse as schematically depicted in Fig. 53:

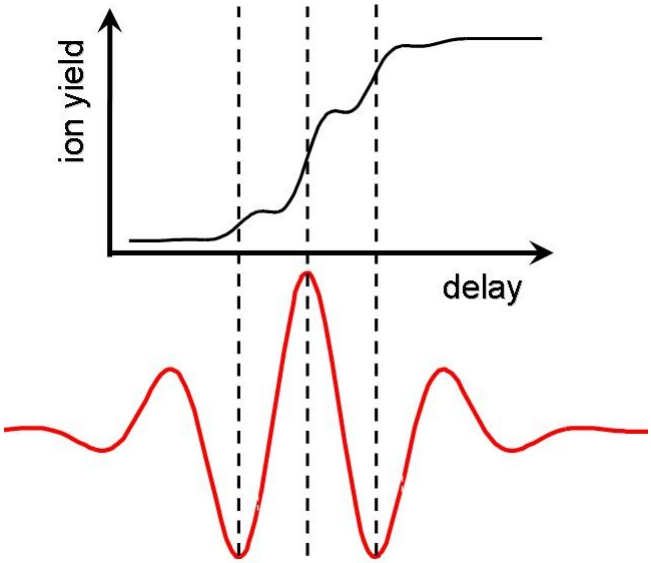

Fig. 53: The integrated number of Ne^{2+} ions increases stepwise with increasing delay between the XUV pump pulse and the attosecond probe pulse.

Neon as the best suitable atomic system for the time-resolved measurement of electron tunneling has been selected due to its high absorption cross section in the available XUV spectral range. Under the chosen experimental conditions the photoexcitation of Krypton and Xenon is accompanied by different Auger decays, which would complicate the interpretation of the experimental results [84, 85].

The first measurement of the stepwise change of the Ne^{2+} count rate in [84] as shown in Fig. 54 could not answer the question in which way the observed steps depend on the fundamental waveform since in this experiment the simultaneous measurement of Ne^{2+} ions and photoelectron streaking data for the identification of the present fundamental waveform were not possible. Now, this measurement has been done at the AS2-beamline,

which gives the possibility to perform streaking measurements in parallel in order to identify the phase of the ionizing wave as presented in chapter 4.1. The results of this measurement are presented in the following section of this chapter.

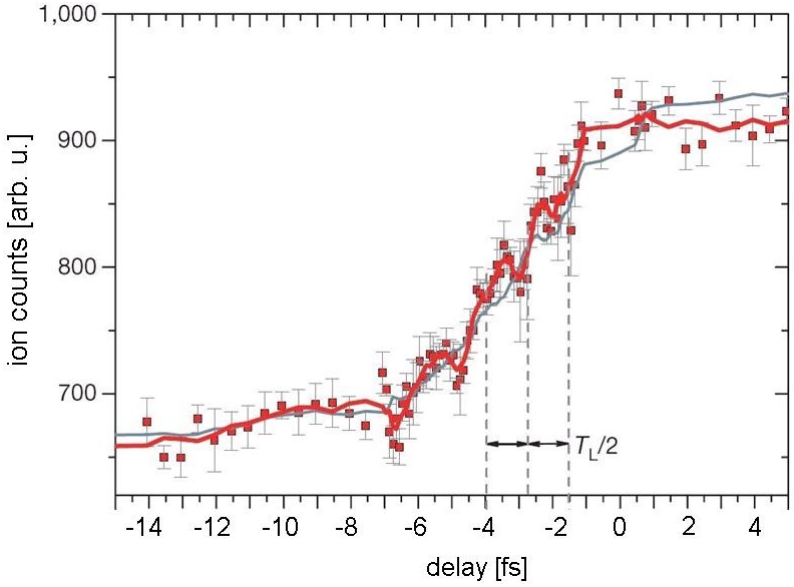

Fig. 54: Counts of Ne^{2+} ions versus delay between the fundamental pulse and the XUV pulse [84]. For negative delays the fundamental pulse precedes the XUV pulse. Subsequent steps are separated by half of the period T_L of the fundamental waveform. A theoretical explanation for the dips in each step, i.e. the short decrease of the Ne^{2+} counts after each step, has not been found yet.

5.1.2 New experimental results

The most severe problem in the measurement of electron tunneling via delay-dependent Ne^{2+} count rates were the poor statistics. Fig. 55 shows the Ne^{2+} count rate for different delays between the XUV pump pulse and the fundamental laser probe pulse. Apart from the first delay step and the last delay step the stepsize was 100 attoseconds. The integration time was 1 sec. A negative delay means in the following measurements that the XUV pump pulse precedes the fundamental probe pulse:

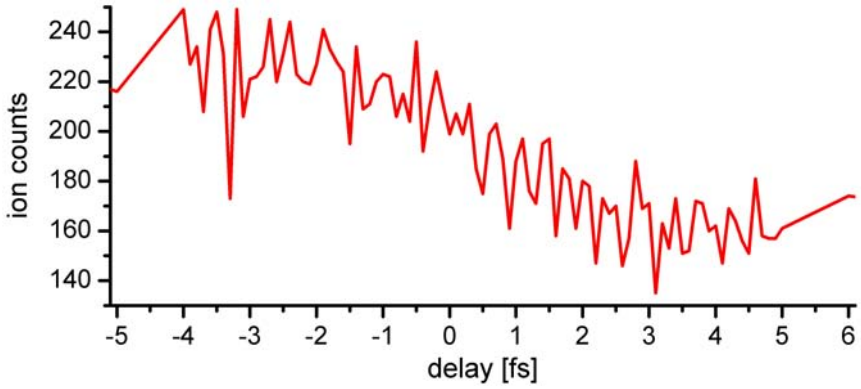

Fig. 55: Counts of Ne^{2+}-ions versus delay between the fundamental pulse and the XUV pulse. The integration time per delay step is 1 sec.

There is a clear decrease of the Ne^{2+} count rate with increasing delay visible. However, the theoretically predicted steps remain hidden in the background noise. Increasing the integration time per delay step to 45 sec was not sufficient for revealing the stepwise decrease of the Ne^{2+} count rate. For this reason, 24 scans with identical delay steps have been performed as shown in Fig. 56:

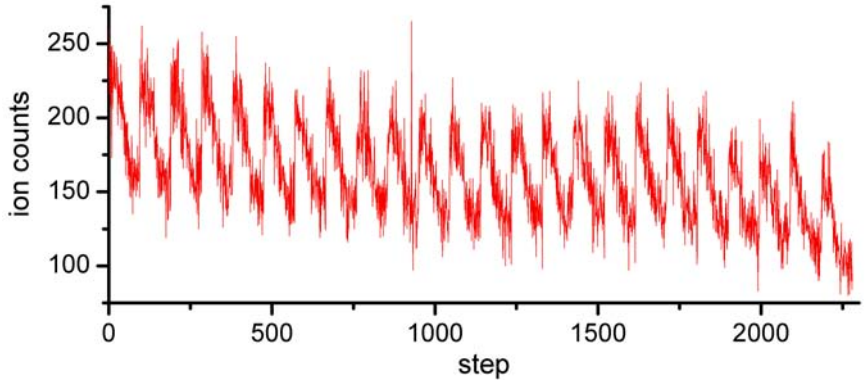

Fig. 56: Sequence of 24 delay scans between the fundamental pulse and the XUV pulse.

In all 24 scans a decrease of the Ne^{2+} count rate is obvious. The total measurement time for all 24 scans amounted to 45 minutes, during which the laser stability substantially degraded as can be concluded from the decreasing average number of Ne^{2+} counts per scan. Therefore each scan was normalized by dividing the number of Ne^{2+} counts per delay step by the average number of Ne^{2+} counts of the corresponding scan. This results in a normalized sequence of 24 scans as shown in Fig. 57:

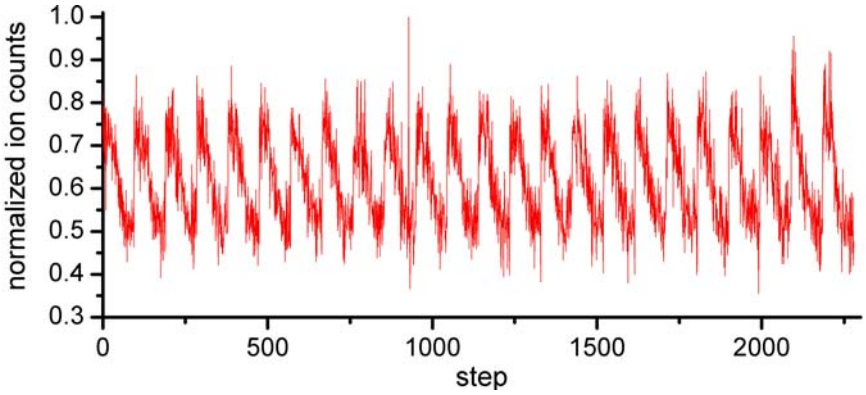

Fig. 57: sequence of 24 normalized delay scans between the fundamental pulse and the XUV pulse

Averaging of all 24 normalized scans gives a curve as shown in Fig. 58. The error bars indicate the standard deviation of 24 data points per delay step.

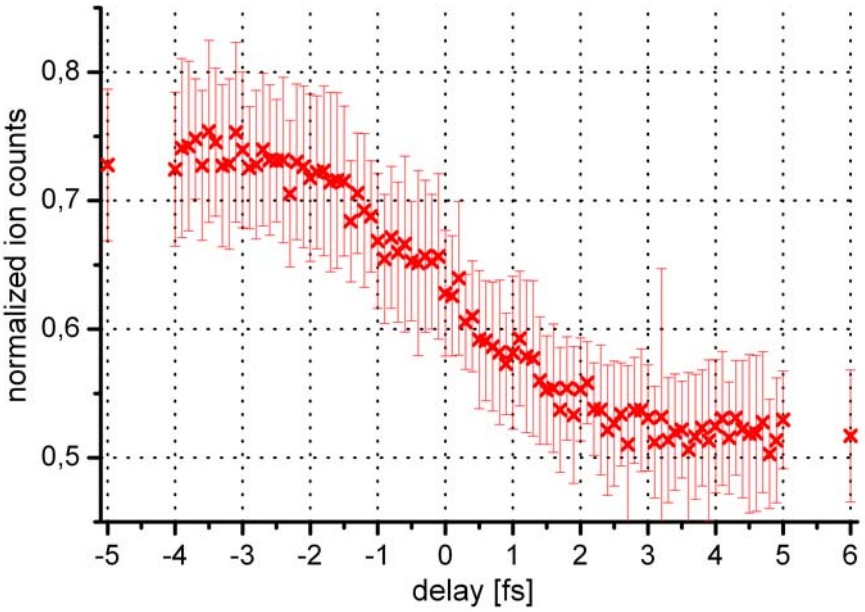

Fig. 58: Average of all 24 normalized delay scans. The error bars indicate the standard deviation from the mean value calculated by averaging 24 data points per delay step.

Here a stepwise decrease of the normalized Ne^{2+} count rate is already visible. Averaging the Ne^{2+} counts of three adjacent delay steps results in a further improvement of the statistics, which is depicted in Fig. 59. However, this adjacent averaging is at the expense of a reduced temporal resolution.

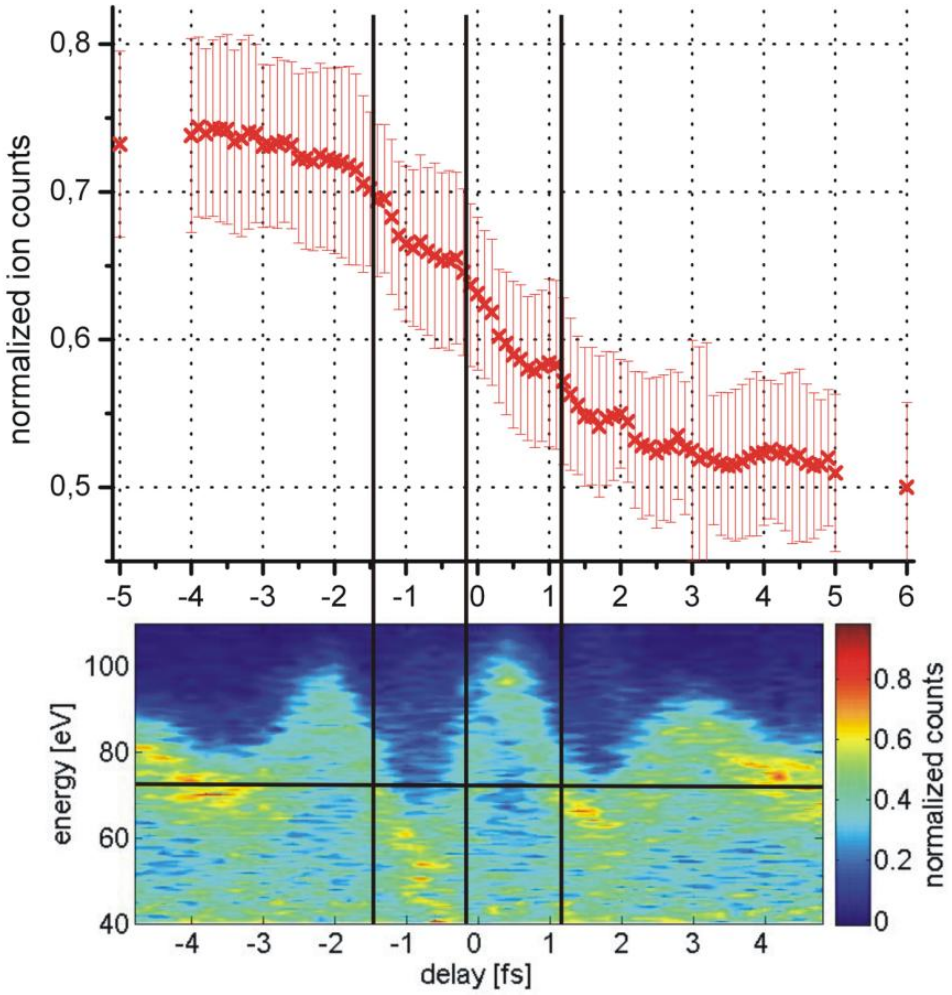

Fig. 59: Comparison of the delay-dependant Ne^{2+} counts with a photoelectron streaking scan: the upper curve shows the average of 24 normalized ion scans. 3 adjacent delay steps are averaged, which improves the statistics but decreases the temporal resolution. The error bars indicate the standard deviation of 72 data points per delay step.

The error bars in Fig. 59 indicate the standard deviation from the mean value of 72 data points. The mean value $\bar{n}_i$ for the delay step i was calculated according to

$$\bar{n}_i = \frac{1}{72} \sum_{j=1}^{24} (n_{i,j} + n_{i+1,j} + n_{i+2,j}),$$

where n_i denotes the number of Ne^{2+} counts at delay step i of scan j. The Ne^{2+} curve in Fig. 59 shows a step at a delay of about 0 fs, which is smaller than the standard deviation. From this follows that the presented data analysis is able to reveal the stepwise behaviour

of the Ne^{2+} curve. A comparision of the Ne^{2+} curve with a streaking scan, which has been acquired before measuring the Ne^{2+} curve, demonstrates that the observed steps coincide with the zero crossings of the streaking curve. Since the streaking curve depicts the vector potential $A(t)$ of the fundamental electric field $E(t)$ as explained in chapter 3.1.2, these zero crossings coincide with the minima and maxima of the electric field curve. This is the first measurement, which connects the stepwise behaviour of the Ne^{2+} count rate as already observed in [84] with a streaking measurement. However, the dips in the Ne^{2+} curve as presented in Fig. 54 could not be sufficiently reproduced so far. In the Ne^{2+} curve of Fig. 59 is only one dip at a delay of 0.8 fs visible but since the standard deviation is much larger than the depth of this dip the statistics are not sufficient for a confirmation of this feature.

5.2 Measuring the shortest time interval

5.2.1 Introduction

In this chapter it is investigated wether there is a measurable delay between different photoelectron emission processes in noble gases. The relevant electron binding energies of noble gases in eV and absorption cross sections in Mb, which are accessible with XUV photon energies of 100 eV, are listed in the following tabular [86, 87]:

He	orbital	1s	-	-	-	-
	energy [eV]	24.6	-	-	-	-
	cross section [Mb]	0.5	-	-	-	-
Ne	orbital	$2p_{3/2}$	$2p_{1/2}$	2s	-	-
	energy [eV]	21.6	21.7	48.5	-	-
	cross section [Mb]	4	4	0.4	-	-
Ar	orbital	$3p_{3/2}$	$3p_{1/2}$	3s	-	-
	energy [eV]	15.7	15.9	29.3	-	-
	cross section [Mb]	0.8	0.8	0.2	-	-
Kr	orbital	$4p_{3/2}$	$4p_{1/2}$	4s	$3d_{5/2}$	$3d_{3/2}$
	energy [eV]	14.1	14.1	27.5	93.8	95
	cross section [Mb]	0.5	0.5	0.2	1	1
Xe	orbital	$5p_{3/2}$	$5p_{1/2}$	5s	$4d_{5/2}$	$4d_{3/2}$
	energy [eV]	12.1	13.4	23.3	67.5	69.5
	cross section [Mb]	2	2	0.5	30	30

All measurements presented in this chapter have been done at the attosecond beamline AS1 as described in [88]. The delay convention is such, that for negative delays the fundamental pulse precedes the XUV pulse. Due to the natural absorption cross sections, the separation of the electron binding energies and the spectral bandwidth of the XUV attosecond pulse the measurements have been concentrated on Helium, Neon and Xenon. In case of Argon and Krypton either the absorption cross sections are too small for a sufficient photoelectron count rate or the energy gap between two adjacent binding energies was too small for a sufficient separation in the photoelectron spectrum since the XUV spectral bandwidth was about 8 eV (FWHM). The spectrum of the attosecond pulse is the product of the multilayer reflectivity, the transmission of the Pd filter and the generated HH spectrum. Fig. 60 shows the reflectivity and GDD of the multilayer mirror, which was used for all results that are presented in this chapter. The temporal intensity profile of the XUV pulse was calculated by means of a FROG retrieval of a streaking scan.

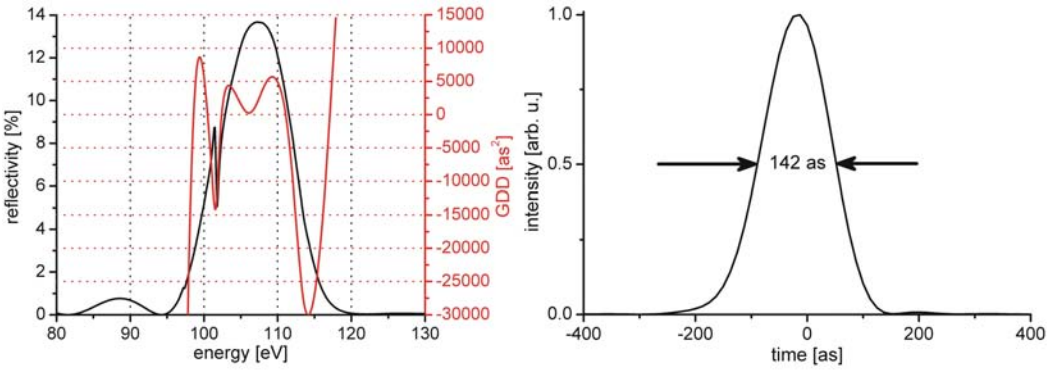

Fig. 60: left: calculated multilayer mirror reflectivity and GDD [81], right: temporal intensity retrieved with a FROG algorithm from a measured streaking spektrogramm [82].

5.2.2 Investigated photoelectron emission processes

Helium is an interesting system from a theoretical point of view, since it contains only 2 electrons and the atomic nucleus. Therefore a theoretical treatment of helium is much less complicated than in other heavier noble gases. In helium two different photoelectron emission processes have been studied: the first process is a direct photoelectron emission of one of the two 1s electrons, the second process is the photoelectron emission of one of the two 1s electrons after scattering at the other 1s electron, which is shifted from the 1s atomic orbital into the 2s atomic orbital:

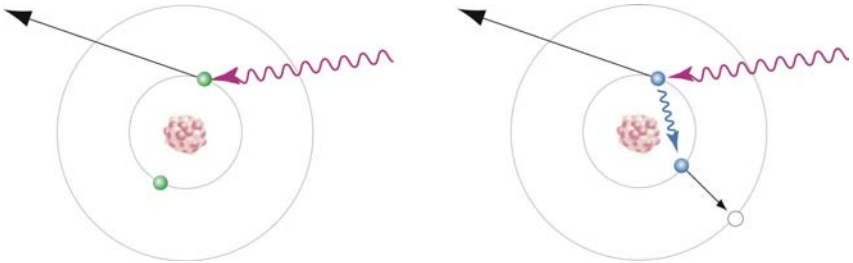

Fig. 61: Direct photoelectron emission (left) and photoelectron emission of the first 1s electron after transition of the other electron into the 2s orbital (right).

The difference in photoelectron energy between these two possibilities is therefore the necessary excitation energy for a transition from the 1s orbital to the 2s orbital. Unfortunately the absorption cross section for the photoelectron emission after scattering is very low. However, it was possible to observe two distinct streaking curves for both photoelectron emission processes:

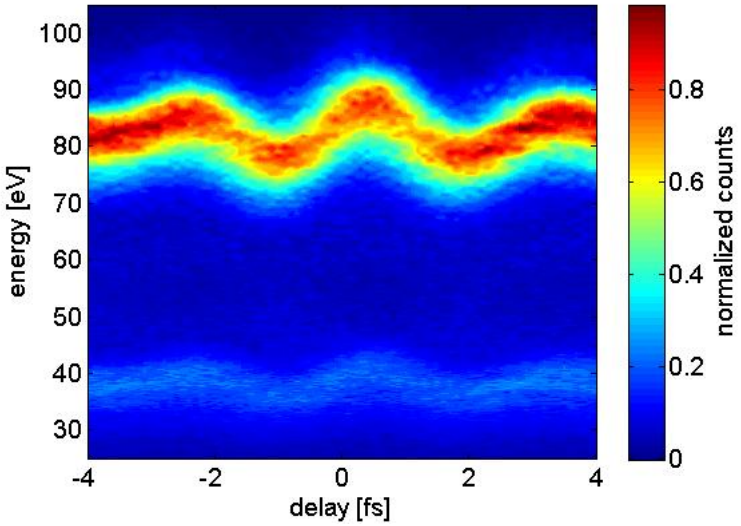

Fig. 62: Streaking of 1s photoelectrons of helium. The streaking curve at higher energies is formed by direct photoemission, the streaking curve at lower energies is formed by photoemission of the first electron and excitation of the second electron.

With photon energies of 100 eV neon can be ionized by photoelectron emission from the 2s shell or the 2p shell. In contrast to helium the emitted photoelectrons originate from two different atomic orbitals:

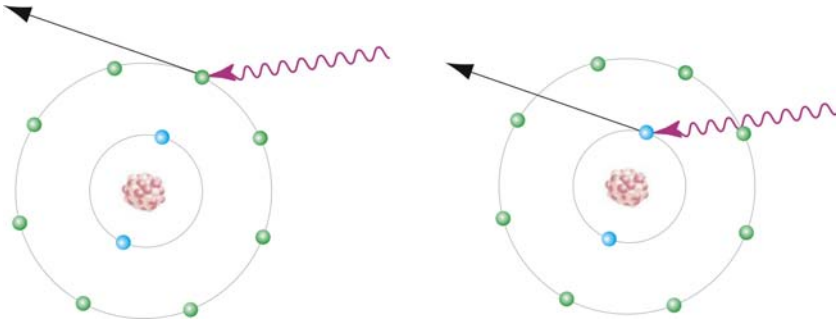

Fig. 63: Photoelectron emission from the 2p shell (left) and photoelectron emission from the 2s shell (right) in neon. The 1s shell is not shown.

Compared to helium much better statistics have been achieved with neon due to the larger absorption cross sections of the two possible photoelectron emission processes. However, the fact that neon contains already 10 electrons causes severe difficulties in an accurate theoretical treatment.

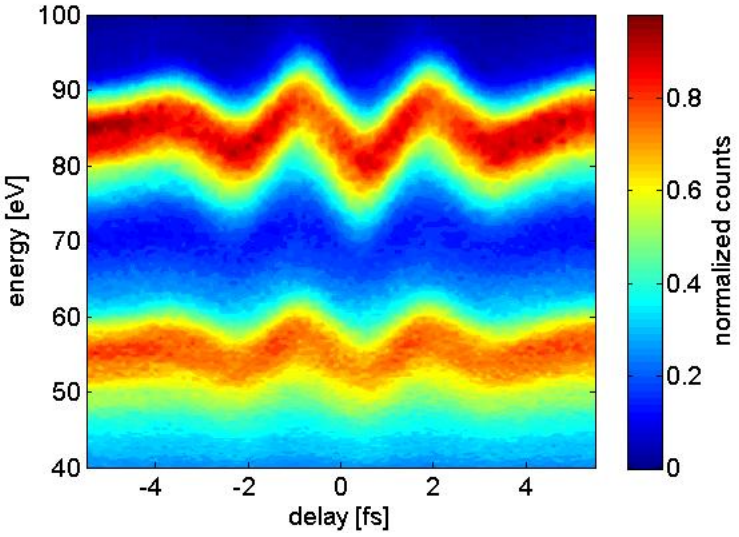

Fig. 64: Streaking of 2s and 2p photoelectrons of neon. The streaking curve at higher energies is formed by photoelectrons emitted from the 2p shell, the streaking curve at lower energies originates from electrons emitted from the 2s shell.

In case of xenon with 54 electrons per atom a reliable calculation of measured delays between altogether three possible photoelectron emission processes for 100 eV photon energy is even more challenging. Here, the photoemission from the 5p, 5s and 4d shell has been investigated. The simultaneous observation of photoelectrons originating from several different Auger decay processes together with the mentioned photoelectron emission from the 5p, 5s and 4d shell as well as the low absorption cross section for the photoelectron emission from the 5s shell complicated the data analysis significantly. But nevertheless, the streaking measurements with xenon served as a valuable reference for ruling out potential systematic measurement errors:

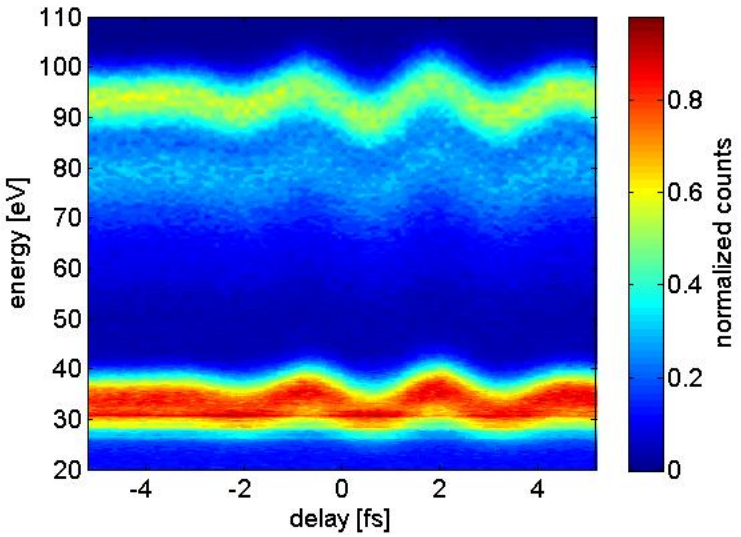

Fig. 65: Xe streaking scan showing the streaking curves of the 5p, 5s and 4d photoelectrons. The absorption cross section in case of the 5s photoelectron is rather low, so that the streaking curve between the 5p and 5s electrons is not well separated. The streaking curve of the 4d photoelectrons coincides with several lines of different Auger decays.

5.2.3 Experimental results

For the data analysis of the shown streaking spectrograms of helium, neon and xenon different methods have been developed. One crucial experimental difficulty were the low absorption cross sections for the 1s photoelectrons, which are emitted after scattering in He, the 2s photoelectrons in Ne and the 5p and 5s photoelectrons of Xe. In order to improve the count rate of these photoelectrons an electronic lens implemented in the electron time-of-flight spectrometer has been used, which increases the count rate in an energy range of about 40 eV (FWHM) by a factor of approximately 100. Unfortunately the same electronic lens boosts also the background which could not be subtracted afterwards since an independent background acquisition was not possible. The background in the photoelectron spectra could only be observed at the simultaneous presence of both the XUV laser pulse and the fundamental laser pulse.

The data analysis proceeds in the following steps:
First, two horizontal slices each containing one of the two streaking curves are cut out from the complete streaking scan, which is shown in Fig. 64:

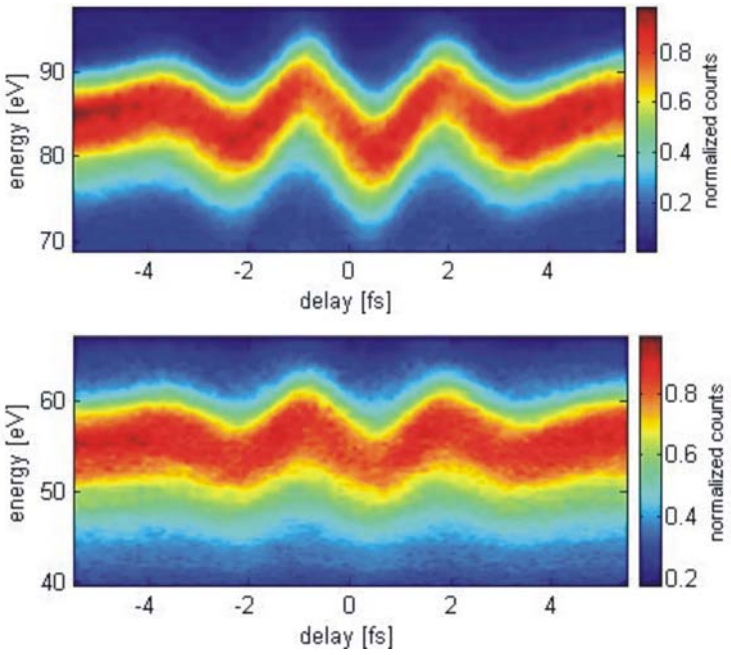

Fig. 66: top: streaking curve of the 2p photoelectrons of Ne, bottom: streaking curve of the 2s photoelectrons of Ne, both streaking curves are cutouts of the complete streaking scan in Fig. 64.

A precondition for this step is a sufficient separation of the two streaking curves. Therefore streaking scans with a too narrow energy gap in between the streaking curves cannot

be processed in this way.
Second, the two streaking scans, which are shown in Fig. 66 have to be converted into streaking curves, i.e. at each delay τ a value for the photoelectron energy has to be identified. For this step three different methods have been tested, which are called center-of-gravity method (COG), restricted-center-of-gravity method (RCOG) and maximum-of-spline method (MOS).

- The most reliable method was the COG method, since this method generated streaking curves with the lowest statistical noise. At each delay τ the photoelectron energy E was defined according to

$$E = \frac{\sum_{i=0}^{n-1} N_i E_i}{\sum_{i=0}^{n-1} N_i} \tag{16}$$

  N_i is the number of photoelectron counts with photoelectron energy E_i. Fig. 67 shows the result of this method in case of the neon streaking scan of Fig. 64:

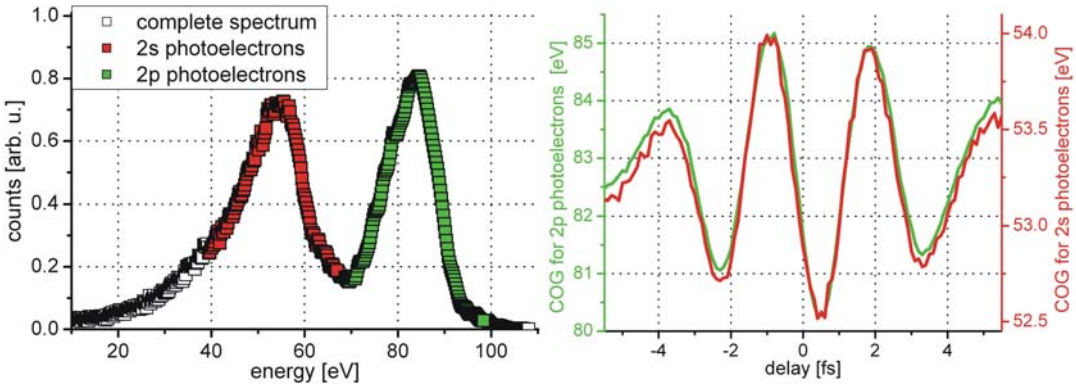

Fig. 67: Complete photoelectron spectrum at τ = -0.1 fs with selected parts for the calculation of the streaking curve for the 2s photoelectrons and the 2p photoelectrons by means of the center of gravity (left) and the calculated streaking curves (right).

  The disadvantage of this method was, that it includes also the background into the calculation. Since this background is energy dependent due to the electronic lens of the electron time of flight spectrometer, especially in case of the streaking scan of the 2s photoelectrons of Neon, the background has a significant influence on the calculated streaking curve.

- In order to reduce the influence of the background two more methods for the calculation of the streaking curve have been tested. The second method was the restricted-center-of-gravity (RCOG) method. The corresponding photoelectron energy for each delay τ was again calculated with equation (16), but this time only photoelectron counts N_i, which exceed an individually defined threshold value are taken into account. In this way, a smaller number of photoelectron counts, which

are dominated more by background noise, have no influence on the final result. The result of this method for the streaking scan of Fig. 64 is shown in the next figure:

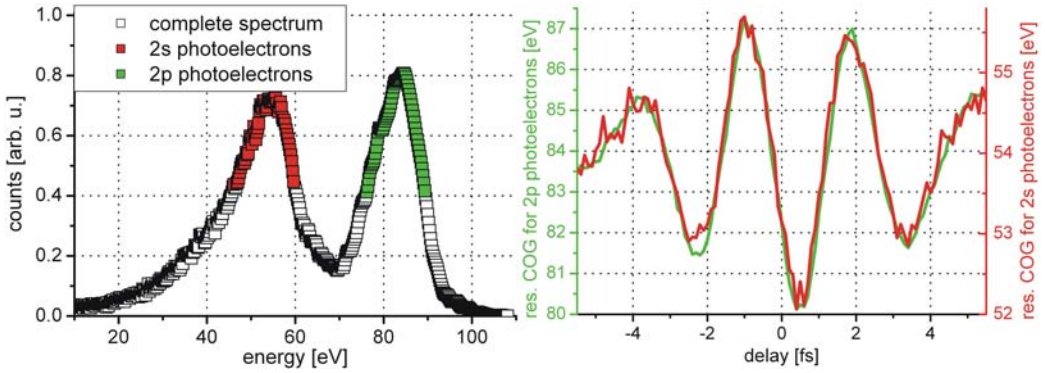

Fig. 68: Complete photoelectron spectrum at τ = -0.1 fs with selected parts for the calculation of the streaking curve for the 2s photoelectrons and the 2p photoelectrons by means of the restricted center of gravity method (left) and the calculated streaking curves (right).

In comparison with the COG method the RCOG shows a much better agreement between the streaking curves of the 2s photoelecctrons and the streaking curves of the 2p photoelectrons especially in the wings of the streaking curves. However, since less data points of the photoelectron spectra are incluced in the calculation of the restricted center of gravity, the statistics of the obtained streaking curves are a bit worse.

- The maximum-of-spline method (MOS) applies a cubic spline fit to each photoelectron spectrum. If **N** is the 1-dim. array of size n, which contains the electron counts and **E** is the 1-dim. array of size n with the corresponding photoelectron energies, then the cubic spline fit procedure minimizes the following function [89]:

$$p\sum_{i=0}^{n-1}\left((N_i - f(E_i)\right)^2 + (1-p)\int_{E_0}^{E_{n-1}}\left(f''(E)\right)^2 dE$$

$0 \leq p \leq 1$ is a balance parameter, which can be set individually. N_i is the ith element of **N**. E_i is the ith element of **E**. $f''(E)$ is the second order derivative of the cubic spline function $f(E)$.

The maximum of the cubic spline fit curve defines the photoelectron energy at the corresponding delay value. For $p = 0.6$ the photoelectron spectrum at delay τ = -0.1 fs in the streaking scan of Fig. 64, the cubic spline fit curves and the corresponding streaking curves are shown in the following figure:

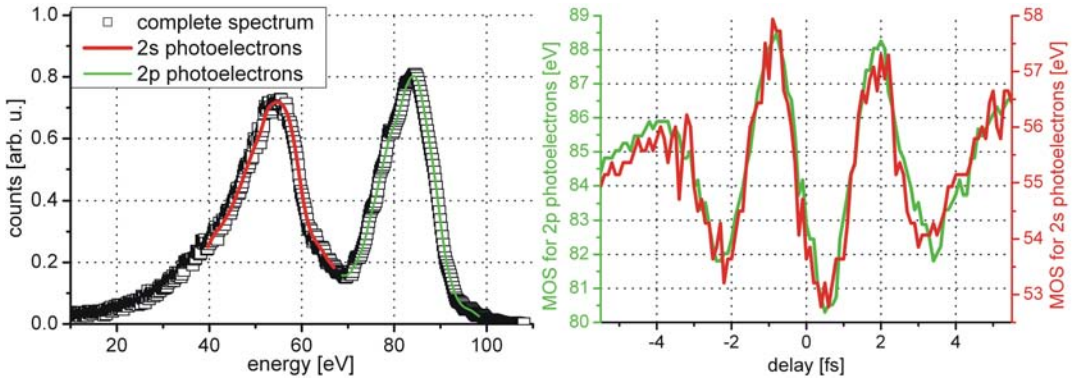

Fig. 69: left: complete photoelectron spectrum at τ = -0.1 fs with the cubic spline fit curves (red and green line) for the 2s photoelectrons and the 2p photoelectrons, right: streaking curves calculated by means of the maximum-of-spline (MOS) method.

Compared to the COG method and the RCOG method the MOS method causes the highest statistical noise in the streaking curves.

The most important argument for the use of the COG method is, that it contains no free parameter, which has to be adjusted. In the RCOG method the threshold parameter and in the MOS method the balance parameter p have to be defined. Depending on the quality of the streaking scan it turned out that in some cases both parameters can significantly change the final result concerning a potential delay between both streaking curves.
After the calculation of the streaking curves, the delay between them has to be calculated. For this task two methods have been tested. The first method is a Fourier analysis of the streaking curves. The second method is a fit procedure, for which a Gaussian pulse shape is assumed.
The Fourier analysis is based on the following theory:
The two streaking curves represent the following two vector potentials, which are for simplicity given in a complex notation:

$$A_1(t) = A_{10} \exp[i\omega t]$$
$$A_2(t) = A_{20} \exp[i\omega(t-\tau)]$$

Fourier transformation of both vector potentials gives:

$$\begin{aligned}
\tilde{A}_1(\omega) &= \int_{\omega=-\infty}^{+\infty} dt\, A_1(t) \exp\left[i\omega t\right] \\
\tilde{A}_2(\omega) &= \int_{\omega=-\infty}^{+\infty} dt\, A_1(t-\tau) \exp\left[i\omega t\right] \\
&= \int_{\omega=-\infty}^{+\infty} dt' A_1(t') \exp\left[-i\omega(t'+\tau)\right] \\
&= \tilde{A}_1(\omega) \exp(-i\omega\tau)
\end{aligned}$$

Therefore, the difference of the spectral phases of both streaking curves at the carrier frequency is identical to the temporal delay τ times the carrier frequency ω_0.
A Fourier analysis of the streaking curves shown in Fig. 67 gives the following curves for the Fourier amplitude and phase:

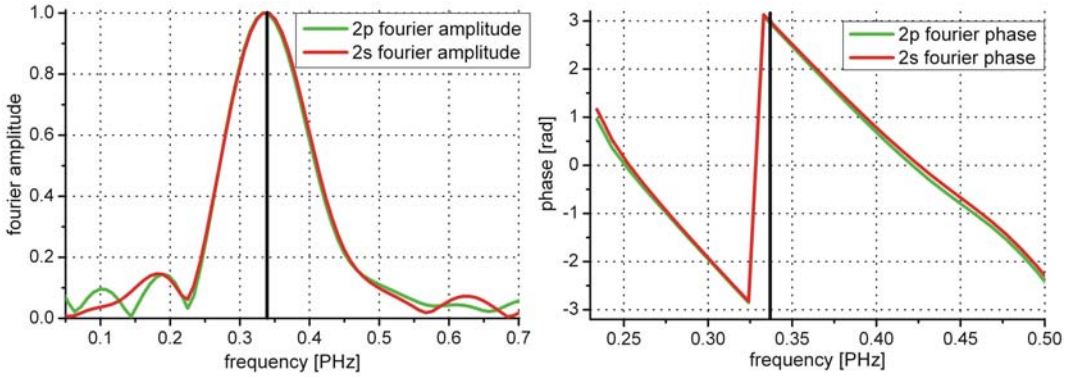

Fig. 70: Fourier amplitude and Fourier phase of the 2p and 2s streaking curves of Fig. 67.

Dividing the difference of the spectral phases, which are shown in Fig. 70, by the corresponding frequency gives the delay between both photoelectron emission processes:

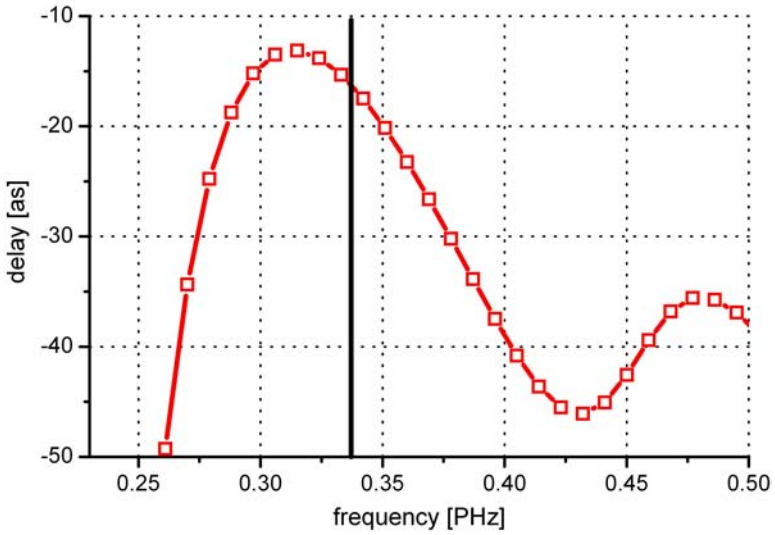

Fig. 71: Phase delay calculated from the fourier phase curves for the 2p and 2s photoelectrons in Fig. 70.

At the central frequency of 0.338 PHz a delay of -17.5 attoseconds is calculated, which means that the 2s photoelectrons are emitted 17.5 as earlier than the 2p photoelectrons.

The fit procedure is based on the assumption of as Gaussian pulse:

$$y(x) = a_1 + a_2 \exp\left[-\frac{4\ \ln(2)}{a_3^2}(x-a_4)^2\right] \cos\left[\frac{2\pi c}{a_5}(x-a_4-a_6) - \frac{1}{2}a_7(x-a_4)^2\right]$$

Definition of parameters:

x: time in fs
y: streaking curve in eV
a_1: offset in eV
a_2: streaking amplitude in eV
a_3: FWHM of Gaussian field envelope in fs
a_4: time shift in fs
a_5: carrier wavelength in nm
a_6: CEP in fs
a_7: linear chirp in rad/fs^2

Fig. 71 shows the result of this fitting procedure for the streaking curves of Fig. 67. First the two streaking curves have been fitted independently. Since the statistics of the

2p streaking curve are much better than the statistics of the 2s streaking curve, in a second fit procedure the fit parameters a_3, a_5, a_6 and a_7, which have been calculated for the 2p streaking curve before, are applied as fixed parameters for the second fit procedure of the 2s streaking curve.

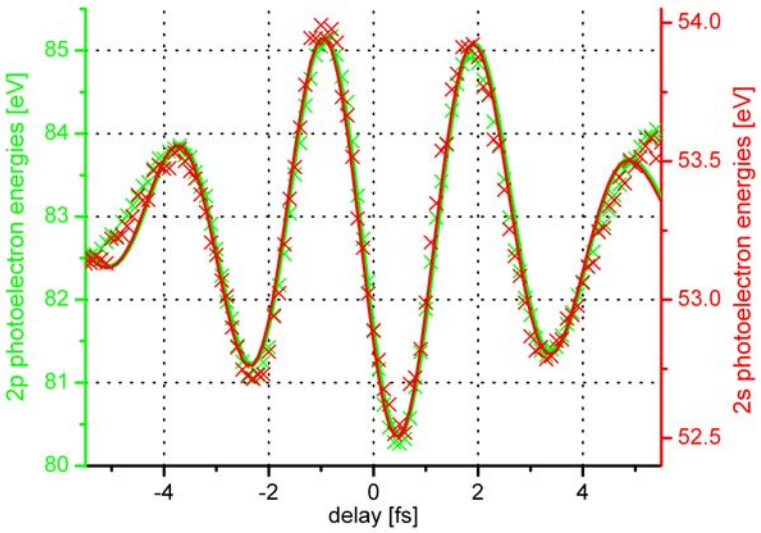

Fig. 72: Streaking curves calculated with the center of gravity method and Gaussian fit curves for the 2p photoelectrons and the 2s photoelectrons.

Eventually, the delay between both fit curves was defined as the difference of parameter a_4, which indicates the time shift between both streaking curves. The final result was a delay of -25.4 as, which is in fair agreement with the result of the Fourier analysis method.

A large number of scans has been acquired in case of neon and all scans have been analysed with the presented methods. Within the measurement error these methods allowed a quick data analysis during the experiments in the laboratory in order to find the best possible measurement parameters in terms of integration time, delay scan range and delay stepsize. In general this analysis confirmed a delay in the photoemission process between the 2s and 2p electrons of neon and it turned out that an integration time of 45 seconds, a delay stepsize of 100 attoseconds and a delay scan range of 10 femtoseconds resulting in a total measurement time of 75 minutes per scan was adequate for achieving sufficiently good statistics.

A more advanced and more time-consuming analysis method based on a time dependent Schrödinger-equation (TDSE) fit routine as described in [90] was invented by Nick Karpowicz. A data analysis with this method gave the following final result:

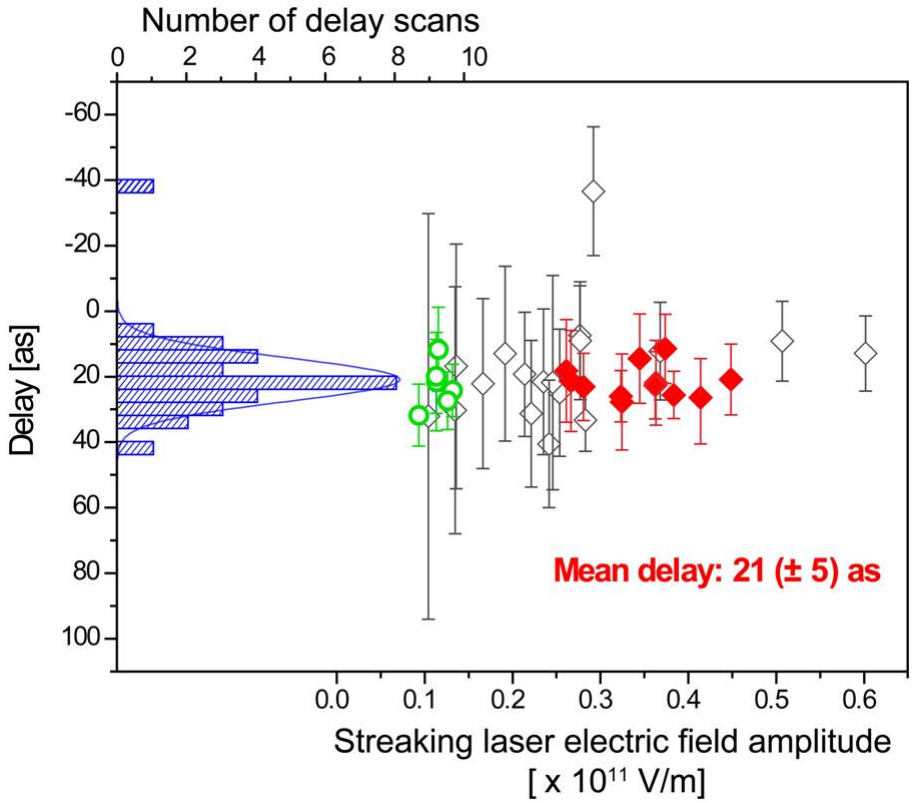

Fig. 73: Analysed delays between the photoemission of 2s and 2p electrons in neon versus the laser electric field amplitude. The red filled diamonds represent the most accurate scans with the lowest amount of satellite pulse. The green circles represent the results of spectrograms recorded with an XUV pulse with narrower bandwidth at the attosecond beamline AS3. The corresponding error bars of the analysed delays are derived from the associated retrieval uncertainties of the TDSE fit routine [90].

As depicted in Fig. 73 an analysis of all available scans revealed that the photoemission of the 2s electron in Neon is 20 ± 5 attoseconds earlier than the photoemission of the 2p electron. For this result 11 streaking scans have been selected, which exhibit the lowest amount of XUV satellite pulse and therefore constitute the most reliable data set. Some additional streaking scans have been performed at the attosecond beamline AS3 with a different multilayer mirror and a different electron time-of-flight spectrometer in order to exclude potential systematic measurement errors. These results are marked with green circles in Fig. 73 and confirm the so far measured delay.

Up to now, theory is not able to reproduce the measured delay in photoemission [90], which is mostly due to the complexity of neon as an electron system containing 10 electrons. Much more reliable theoretical predictions about potential delays in photoemission processes exist for helium, which contains only 2 electrons. Unfortunately the statistics in case of helium turned out not to be sufficient for the accurate measurement of a similar delay as can be concluded from Fig. 62. However, it is foreseeable that a higher XUV photon flux in future attosecond beamlines will soon allow for reliable experimental results also in case of helium.

6 Conclusions and outlook

This section should summarize the most important experimental results achieved in this thesis and draw the attention to future experiments, which have been enabled by this work:

- In conclusion, it can be stated that in the frame of this thesis the shortest ever measured time interval was detected via a direct measurement in the time domain. It was found that the photoemission of 2s electrons in neon is 20 attoseconds earlier than the photoemission of the 2p electrons. This discovery contradicts the so far common but experimentally unverified assumption of an instantaneous photoemission process. Due to the complexity of the neon atom as an atomic system containing 10 interacting electrons a sufficient theoretical explanation of this result is currently not possible.

- The second important experimental result achieved in this work was the clocking of electron tunneling in atoms with ultrashort laser pulses via a simultaneous measurement of the number of ions and the optical waveform. This result opens the door to investigations on the temporal structure of the electron tunneling effect as a second quantum mechanical effect besides the photoemission process on an attosecond timescale.

- High harmonic generation with synthesized optical waveforms consisting of the fundamental wave and its second harmonic wave culminated in the discovery of a method for the generation of tunable isolated attosecond laser pulses. In future experiments, this important finding will considerably simplify time-resolved experiments on an attosecond timescale for which XUV pulses with different photon energies are needed.

- The first characterization of chirped XUV mirrors in terms of reflectance and phase allows for full control of the attosecond pulse shape. Chirped XUV mirrors, which control the phase of attosecond laser pulses, will enable future investigations of electron dynamics that are imprinted in the phase of the electronic wavepacket. Furthermore, we have now the possibility to address selectively electronic transitions not only by the central energy of an XUV pulse but also by its chirp.

- The invention of metal-coated XUV mirrors increased the XUV flux on target by two orders of magnitude resulting in an improved signal-to-noise ratio by a factor of 10. In future experiments, such an improvement of the achievable statistics in attosecond experiments allows for the investigation of systems, which were so far not accessible due to their low absorption cross section in the XUV. Measuring a potential delay in the photoemission process of helium, which can be calculated much more reliably than in the case of neon, is now within reach.

- The generation of the shortest and most energetic laser pulses in the spectral range between 200 and 300 nm succeeded by means of third harmonic generation of few-cycle fundamental laser pulses. In future experiments, this simple method will serve for the generation of powerful pump-pulses for the excitation of electron dynamics in molecules, which are subsequently probed by attosecond laser pulses.

The experimental basis of these results and the proposed future experiments was the experimental setup of the attosecond beamline AS2, which has been originally suggested in 2005 [91]. This setup is now fully operational. The sufficient stability of the Mach-Zehnder interferometer suitable for pump-probe experiments on an attosecond timescale, which was the main uncertainty in the concept of this novel attosecond beamline system, has been verified in numerous streaking experiments. A large number of diagnostics has been installed and successfully tested:

- two XUV grating spectrometers, for the characterization of high harmonic radiation and for future transient absorption measurements
- one electron time-of-flight spectrometer for photoelectron spectroscopy
- one reflectron ion spectrometer for the detection of charged products of electronic processes
- imaging systems for the alignment of the temporal overlap of pump and probe beams

The mentioned diagnostics are now ready for the conduction of time-resolved experiments investigating electron dynamics in molecules [92]. One promising candidate is ozone, since its absorption cross section in the deep ultraviolet perfectly matches with the spectrum of the ultrashort UV-pulses, which have been generated in this work, and and also with the fundamental spectrum. The electronic excitation of the ozone molecule with both the fundamental and the third harmonic laser pulse will result in the coherent population of two excited electronic states, which give rise to the large absorption cross section in the Chappuis-band and Hartley-band. Probing the population of the coherently excited electronic states of ozone with attosecond XUV pulses by means of photoelectron spectroscopy will reveal the quantum beating between the two excited electronic states. The period T of a quantum beating is generally determined by the energy difference ΔE between the two excited states:

$$T[fs] = \frac{4.1357}{\Delta E[eV]}$$

The energy difference ΔE between the Hartley-band and the Chappuis-band amounts to 2.7 eV, resulting in a beating period of 1.5 fs. The measurement of photoelectron spectra of ozone for different delays between the fundamental and UV pump pulses and the XUV probe pulse will result in the observation of an oscillating photoelectron energy of electrons, which are released by the XUV probe pulse from the populated excited states

after the coherent electronic excitation took place. Since an excitation in the Hartley-band populates repulsive electronic states the ozone molecules will start to dissociate on a femtosecond timescale. Such a dissociation corresponds to a propagation along the reaction coordinate in Fig. 74 resulting in a shift of the energy of the excited electronic states and therefore also in a change of the observed beating frequency.

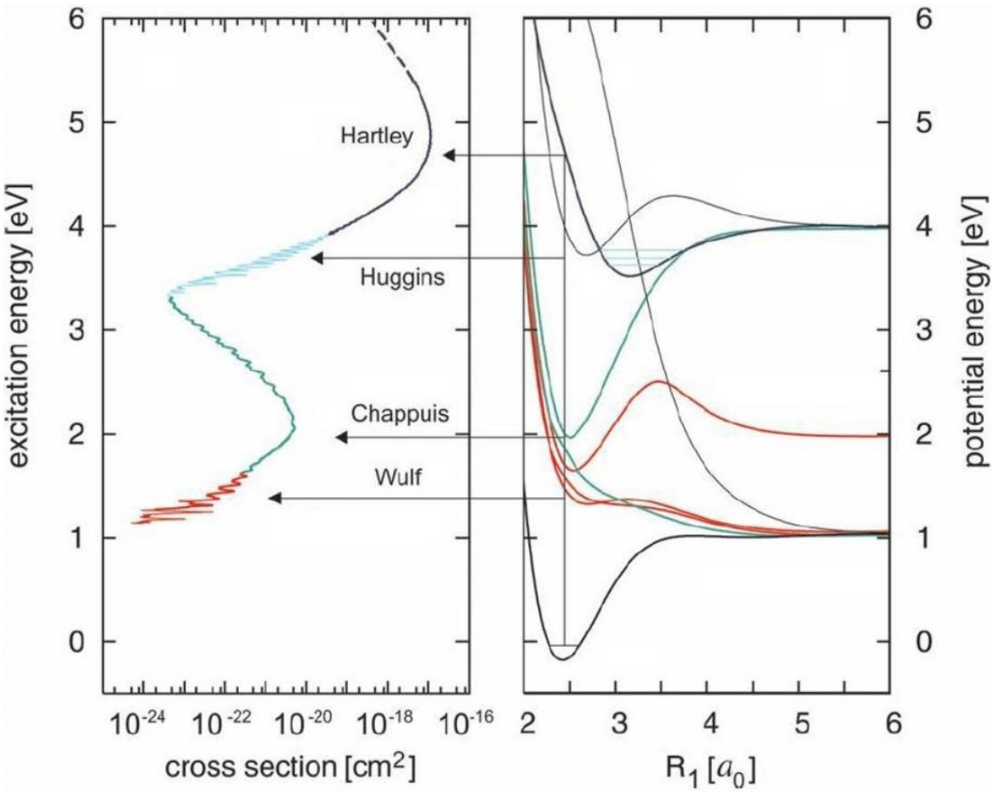

Fig. 74: Absorption cross section (left) and the calculated potential surfaces (right) of ozone [93]. The reaction coordinate R_1 is the distance between two adjacent oxygen atoms in the ozone molecule.

This experiment will be followed by more complicated investigations on electron dynamics in molecules. Time-resolving of ultrafast charge migration in biomolecules will give insight into biological processes like energy and information transport. Ultrafast adsorbant-to-substrate charge transfer may speed up photovoltaics. Understanding the very first instants of the formation of chemical bindings (rearrangement of electrons) may lead to coherent control of chemical reactions. All these processes and findings we can not foresee right now will have influence on molecular electronics, optical nanostructuring, ultrafast chemistry and many more fields in science.

7 Appendix

7.1 Derivation of Poisson's sum rule

Every periodic function

$$g(t) = \sum_{n=-\infty}^{+\infty} f(t + nT)$$

with period T can be expanded into a Fourier series

$$g(t) = \sum_{m=-\infty}^{+\infty} c_m \exp(im\omega_0 t) \quad \text{with } \omega_0 = \frac{2\pi}{T}. \tag{17}$$

The Fourier coefficients c_m are determined by

$$c_m = \frac{1}{T} \int_{t=-T/2}^{+T/2} dt\, g(t) \exp(-im\omega_0 t).$$

With $\tau = t + nT$ one has

$$\begin{aligned} c_m &= \frac{1}{T} \sum_{n=-\infty}^{+\infty} \int_{\tau=nT-T/2}^{nT+T/2} d\tau\, f(\tau) \exp\left[-im\omega_0(\tau - nT)\right] \\ &= \frac{1}{T} \sum_{n=-\infty}^{+\infty} \int_{\tau=nT-T/2}^{nT+T/2} d\tau\, f(\tau) \exp(-im\omega_0\tau) \underbrace{\exp(imn2\pi)}_{=1 \forall\, n,m} \\ &= \frac{1}{T} \int_{\tau=-\infty}^{+\infty} d\tau\, f(\tau) \exp(-im\omega_0\tau). \end{aligned} \tag{18}$$

Using eq. (17) and (18) we obtain

$$\begin{aligned} g(t) &= \sum_{n=-\infty}^{+\infty} f(t + nT) \\ &= \sum_{m=-\infty}^{+\infty} c_m \exp(im\omega_0 t) \\ &= \sum_{m=-\infty}^{+\infty} \frac{1}{T} \int_{\tau=-\infty}^{+\infty} d\tau\, f(\tau) \exp(-im\omega_0\tau) \exp(im\omega_0 t) \\ &= \frac{1}{T} \sum_{m=-\infty}^{+\infty} \int_{\tau=-\infty}^{+\infty} d\tau\, f(\tau) \exp\left[im\omega_0(t - \tau)\right]. \end{aligned} \tag{19}$$

Reexpressing $g(t)$ in terms of equally spaced Dirac delta functions and comparison with eq. (19) yields

$$\begin{aligned} g(t) = \sum_{n=-\infty}^{+\infty} f(t+nT) &= \sum_{n=-\infty}^{+\infty} \int_{\tau=-\infty}^{+\infty} d\tau\, f(\tau)\delta(\tau - t - nT) \\ &= \sum_{m=-\infty}^{+\infty} \int_{\tau=-\infty}^{+\infty} d\tau\, f(\tau) \frac{1}{T} \exp\left[im\omega_0(t-\tau)\right] \\ \Leftrightarrow \quad \sum_{n=-\infty}^{+\infty} \delta(\tau - t - nT) &= \frac{1}{T} \sum_{m=-\infty}^{+\infty} \exp\left[im\omega_0(t-\tau)\right]. \end{aligned}$$

With $x = (\tau - t)/T$ and $\omega = 2\pi/T$ one gets Poisson's sum rule [94]

$$\sum_{n=-\infty}^{+\infty} \delta\left(x - n\right) = \sum_{m=-\infty}^{+\infty} \exp\left(-im2\pi x\right). \tag{20}$$

8 Abbreviations

as	attosecond
ASE	amplified spontaneous emission
BBO	barium-borate
BS	beam splitter
BW	bandwidth
CEP	carrier envelope phase
COG	center of gravity
cm	centimeter
cw	continuous wave
DFG	difference frequency generation
DUV	deep ultraviolet
e-TOF	electron time of flight spectrometer
eV	electronvolt
FROG	frequency resolved optical gating
fs	femtosecond
FWHM	full width at half maximum
g	gram
GDD	group delay dispersion
GVD	group velocity dispersion
HH	high harmonics
HHG	high harmonic generation
HCF	hollow core fiber
Hz	hertz
kg	kilogram
Mb	megabarn
min	minute
MM	multilayer mirror
MOS	maximum of spline
MPI	multi photon ionization
ms	millisecond
μm	micrometer
nJ	nanojoule
nm	nanometer
NIR	near infrared
ns	nanosecond
PM	perforated mirror
PPLN	periodically poled lithium niobate
ps	picosecond
RCOG	restricted center of gravity
rad	radian
s	second

SD	self diffraction
SFG	sum frequency generation
SH	second harmonic
SHG	second harmonic generation
SPM	self phase modulation
SPIDER	spectral interferometry for direct electric field reconstruction
TDSE	time-dependent Schrödinger-equation
THG	third harmonic generation
TOD	third order dispersion
UV	ultraviolet
V	volt
XUV	extreme ultraviolet

9 Acknowledgements

First of all, I want to thank Prof. Ferenc Krausz for giving me the chance to do my PhD in his group and for providing the ideal research conditions.

In the same way I' m grateful to Prof. Reinhard Kienberger for supervising me during my study. He continuously supported me with his experience and knowledge and was always of great help whenever I had problems in all matters related to my work. I am indebted to Martin Schultze, who provided his valuable expertise in laser alignment, in streaking measurements and in the operation of numerous scientific instruments like time-of-flight spectrometers and CEP-stabilization systems. Without his engagement the results, which have been presented in this thesis, would not have been possible. I am thankful to Prof. Johannes Barth as the second reviewer of this thesis.

During the last few years it has always been a pleasure to me to collaborate with many nice colleagues even in times when the experiment totally misbehaved. I want to thank Balint Horvath, with whom I' ve spent many nights and weekends (in the lab), for the warm working atmosphere, for his staying power in situations when the sought after measurement signal managed to hide for several months. I' ve spend a nice time with Ulrich Graf, Markus Gabrysch and Eleftherios Goulielmakis during the generation and characterization of ultrashort UV-pulses. Michael Hofstetter provided numerous flat and curved XUV-multilayer mirrors, which have been a prerequisite for the conduction of many experiments presented in this thesis.

My work was continuously supported by several working students and diploma students. I am grateful to Denis Bytschkow for the design of a healthy lift-up system for the 20-kg-lid of our high harmonic generation chamber, which found its application also at other attosecond beamlines of our group. I appreciate the contributions of Katrin Peeper and Johann Riemensberger for the CEP stabilization of our laser system and the active stabilization of the Mach-Zehnder interferometer of the AS2-beamline. Last but not least I want to thank Benjamin Dennhardt for his very competent work on the active interferometer stabilization, his very helpful assistance and his great motivation, which enabled him to acquire the knowledge for operating the AS2 beamline.

I am also thankful for the technical support provided by many excellent technicians of our group. Mr. Schönauer and Mr. Rauffer designed a great number of vacuum and optomechanical components, which have all been fabricated by the MPQ workshop under the guidance of Mr. Strobel. Mr. Haas and Mr. Horn have been of great help in all matters related to electronics, especially in the interferometer stabilization electronics. Mr. Fischer and Mr. Böswald supported me in the setup of large-scale turbo pump mounts and many other vacuum components.

Since I' ve started my PhD I' ve been profiting a lot from the previous work of numerous colleagues, who have originally designed the basic concept and setup the vacuum system

of the AS2 beamline: Eleftherios Goulielmakis, Stefan Köhler, Bernhard Reiter, Matthias Uiberacker, Reinhard Kienberger, Michael Hentschel and others.

Special thanks go to Mrs. Wild and her unbeatable organizing ability not only in the framework of IMPRS. Similarly I' m grateful to the administrative staff of Prof. Krausz' office and the MPQ purchase department for handling an uncountable number of my orders during the last few years.

Finally, I want to thank many of my former and present colleagues and collaborators for the nice working atmosphere and their support: Elisabeth Bothschafter, Adrian Cavalieri, Prof. Ya Cheng, Yunpei Deng, Prof. Wolfgang Domcke, Ralph Ernstorfer, Justin Gagnon, Sergy Grebenshchikov, Ivanka Grguras, Xun Gu, Wolfram Helml, Prof. Christof Janssen, Elisabeth Magerl, Gilad Marcus, Thomas Metzger, Volodymyr Pervak, Antonia Popp, Oleg Pronin, Florentin Reiter, Prof. Eberhard Riedle, Agustin Schiffrin, Karl Schmid, Harmut Schröder, Alexander Schwarz, Wolfgang Schweinberger, Prof. Armin Scrinzi, Adrian Wirth, Tibor Wittmann and Vladislav Yakovlev.

10 Curriculum vitae

Contact information

Name: Markus Fieß
Address: Max-Planck Institute of Quantum Optics, Hans-Kopfermann-Straße 1, 85748 Garching
Phone: +49 (0) 89 32905 623
E-mail: markus.fiess@mpq.mpg.de

Personal data

Date and place of birth: October 20, 1981 in Oberkirch, Germany
Citizenship: German
Gender: male

Education

11/2006-present
Max-Planck-Institut für Quantenoptik, Garching, Germany
and Ludwig-Maximilians-Universität München, Germany
Dissertation title: "Advancing attosecond metrology"
Supervisor: Prof. Dr. Ferenc Krausz

04/2002-10/2006
Technical University of Karlsruhe, Germany
Diploma in Chemistry
Thesis title: "Aufbau eines FROG-Systems zur Charakterisierung von Femtosekunden-Laserpulsen"
Supervisor: Prof. Dr. Horst Hippler

07/2001-03/2002
Luftwaffenmusikkorps 2, Karlsruhe, Germany
military service

09/1992-06/2001
Hans-Furler Gymnasium, Oberkirch, Germany
High School Diploma

11 Literature

References

[1] T. H. Maiman. Stimulated optical radiation in ruby. *Nature*, **187**(4736): 493–494, 1960.

[2] A. J. De Maria, D. A. Stetser, and H. Heynau. Self mode-locking of lasers with saturable absorbers. *Applied Physics Letters*, **8**: 174–176, 1966.

[3] J. J. Sakurai. *Modern Quantum Mechanics*. Adison Wesley, Reading, Massachusetts, 1994.

[4] M. Drescher, M. Hentschel, R. Kienberger, M. Uiberacker, V. Yakovlev, A. Scrinzi, Th. Westerwalbesloh, U. Kleineberg, U. Heinzmann, and F. Krausz. Time-resolved atomic inner-shell spectroscopy. *Nature*, **419**: 803–807, 2002.

[5] A. L. Cavalieri, N. Müller, Th. Uphues, V. S. Yakovlev, A. Baltuska, B. Horvath, B. Schmidt, L. Blümel, R. Holzwarth, S. Hendel, M. Drescher, U. Kleineberg, P. M. Echenique, R. Kienberger, F. Krausz, and U. Heinzmann. Attosecond spectroscopy in condensed matter. *Nature*, **449**: 1029–1032, 2007.

[6] M. Hentschel, R. Kienberger, Ch. Spielmann, G. A. Reider, N. Milosevic, T. Brabec, P. Corkum, U. Heinzmann, M. Drescher, and F. Krausz. Attosecond metrology. *Nature*, **414**(29): 509–513, 2001.

[7] E. Goulielmakis, M. Schultze, M. Hofstetter, V. S. Yakovlev, J. Gagnon, M. Uiberacker, A. L. Aquila, E. M. Gullikson, D. T. Attwood, R. Kienberger, F. Krausz, and U. Kleineberg. Single-cycle nonlinear optics. *Science*, **320**: 1614–1617, 2008.

[8] G. Wedler. *Lehrbuch der Physikalischen Chemie*. Wiley-VCH, Weinheim, fourth edition, 1997.

[9] R. L. Mössbauer. Kernresonanzfluoreszenz von Gammastrahlung in Ir^{191}. *Zeitschrift für Physik*, **151**: 124–143, 1958.

[10] A. L. Cavalieri, E. Goulielmakis, B. Horvath, W. Helml, M. Schultze, M. Fieß, V. Pervak, L. Veisz, V. Yakovlev, M. Uiberacker, A. Apolonskiy, F. Krausz, and R. Kienberger. Intense 1.5-cycle near infrared laser waveforms and their use for the generation of ultra-broadband soft-x-ray harmonic continua. *New Journal of Physics*, **9**(242), 2007.

[11] U. Graf, M. Fieß, M. Schultze, R. Kienberger, F. Krausz, and E. Goulielmakis. Intense few-cycle light pulses in the deep ultraviolet. *Optics Express*, **16**(23): 18956–18963, 2008.

[12] W. Demtröder. *Experimentalphysik 2: Elektrizität und Optik*. Springer, Heidelberg, second edition, 2002.

[13] R. W. Boyd. *Nonlinear Optics*. Academic Press, London, second edition, 2003.

[14] D. B. Brayton. Small particle signal characteristics of a dual-scatter laser velocimeter. *Applied Optics*, **13**(10): 2346–2351, 1974.

[15] G. Mainfray and C. Manus. Multiphoton ionization of atoms. *Reports on Progress in Physics*, **54**: 1333–1372, 1991.

[16] T. Brabec and F. Krausz. Intense few-cycle laser fields: Frontiers of nonlinear optics. *Reports on Progress in Physics*, **72**(2): 545–591, 2000.

[17] G. S. Voronov and N. B. Delone. Ionization of the xenon atom by the electric field of ruby laser emission. *JETP Letters*, **1**(2): 66–68, 1965.

[18] E. A. Martin and L. Mandel. Electron energy spectrum in laser-induced multiphoton ionization of atoms. *Applied Optics*, **15**(10): 2378–2380, 1976.

[19] P. Agostini, F. Fabre, G. Mainfray, G. Petite, and N. K. Rahman. Free-free transitions following six-photon ionization of xenon atoms. *Physical Review Letters*, **42**(17): 1127–1130, 1979.

[20] L. V. Keldysh. Ionization in the field of a strong electromagnetic wave. *Soviet Physics JETP*, **20**: 1307, 1965.

[21] M. V. Ammosov, N. B. Delone, and V. P. Krainov. Tunnel ionization of complex atoms and atomic ions by an alternating electromagnetic field. *Soviet Physics JETP*, **64**: 1191, 1986.

[22] P. B. Corkum. Plasma perspective on strong-field multiphoton ionization. *Physical Review Letters*, **71**(13): 1994–1997, 1993.

[23] M. Lewenstein, Ph. Balcou, M. Yu. Ivanov, A. L'Huillier, and P. B. Corkum. Theory of high-harmonic generation by low-frequency laser fields. *Physical Review A*, **49**(3): 2117–2132, 1994.

[24] X. Gu, G. Marcus, Y. Deng, T. Metzger, C. Teisset, N. Ishii, T. Fuji, A. Baltuska, R. Butkus, V. Pervak, H. Ishizuki, T. Taira, T. Kobayashi, R. Kienberger, and F. Krausz. Generation of carrier-envelope-phase-stable 2-cycle 740-μj pulses at 2.1-μm carrier wavelength. *Optics Letters*, **17**(1): 62–69, 2009.

[25] P. Colosimo, G. Doumy, C. I. Blaga, J. Wheeler, C. Hauri, F. Catoire, J. Tate, R. Chirla, A. M. March, G. G. Paulus, H. G. Muller, P. Agostini, and L. F. Dimauro. Scaling strong-field interactions towards the classical limit. *Nature Physics*, **4**(5): 386–389, 2008.

[26] K. Varjú, P. Johnsson, R. López-Martens, T. Remetter, E. Gustafsson, J. Mauritsson, M. B. Gaarde, K. J. Schafer, Ch. Erny, I. Sola, A. Zair, E. Constant, E. Cormier, E. Mével, and A. L'Huillier. Experimental studies of attosecond pulse trains. *Laser Physics*, **15**: 888, 2005.

[27] P. Antoine, A. L'Huillier, and M. Lewenstein. Attosecond pulse trains using high-order harmonics. *Physical Review Letters*, **77**(7): 1234–1237, 1996.

[28] G. Sansone, E. Benedetti, F. Calegari, C. Vozzi, L. Avaldi, R. Flammini, L. Poletto, P. Villoresi, C. Altucci, R. Velotta, S. Stagira, S. De Silvestri, and M. Nisoli. Isolated single-cycle attosecond pulses. *Science*, **314**: 443–446, 2006.

[29] Berkeley Center for X-ray optics. Website, 2010. http://henke.lbl.gov/optical_constants/.

[30] P. B. Corkum, N. H. Burnett, and M. Y. Ivanov. Subfemtosecond pulses. *Optics Letters*, **19**(22): 1870–1872, 1994.

[31] I. J. Sola, E. Mével, L. Elouga, E. Constant, V. Strelkov, L. Poletto, P. Villoresi, E. Benedetti, J.-P. Caumes, S. Stagira, C. Vozzi, G. Sansone, and M. Nisoli. Controlling attosecond electron dynamics by phase-stabilized polarization gating. *Nature Physics*, **2**(5): 319–322, 2006.

[32] M. Maier, W. Kaiser, and J. A. Giordmaine. Intense light bursts in the stimulated raman effect. *Physical Review Letters*, **17**(26): 1275–1277, 1966.

[33] K. L. Sala, A. Kenney-Wallace, and G. E. Hall. CW autocorrelation measurements of picosecond laser pulses. *IEEE Journal of Quantum Electronics*, **QE-16**(9): 990–996, 1980.

[34] D. J. Kane and R. Trebino. Characterization of arbitrary femtosecond pulses using frequency-resolved optical gating. *IEEE Journal of Quantum Electronics*, **29**(2): 571–579, 1993.

[35] R. Trebino, K. W. DeLong, D. N. Fittinghoff, J. N. Sweetser, M. A. Krumbügel, B. A. Richman, and D. J. Kane. Measuring ultrashort laser pulses in the time-frequency domain using frequency-resolved optical gating. *Review of Scientific Instruments*, **68**(9): 3277–3295, 1997.

[36] C. Iaconis and I. A. Walmsley. Spectral phase interferometry for direct electric-field reconstruction of ultrashort optical pulses. *Optics Letters*, **23**(10): 792–794, 1998.

[37] P. Tzallas, D. Charalambidis, N. A. Papadogiannis, K. Witte, and G. D. Tsakiris. Direct observation of attosecond light bunching. *Nature*, **426**(20): 267–271, 2003.

[38] J. Itatani, F. Quéré, G. L. Yudin, M. Yu. Ivanov, F. Krausz, and P. B. Corkum. Attosecond streak camera. *Physical Review Letters*, **88**(17): 173903, 2002.

[39] K. Kinoshita, M. Ito, and Y. Suzuki. Femtosecond streak tube. *Review of Scientific Instruments*, **56**(6): 932–938, 1987.

[40] J. Gagnon, E. Goulielmakis, and V. S. Yakovlev. The accurate FROG characterization of attosecond pulses from streaking measurements. *Applied Physics B*, **92**(17): 25–32, 2008.

[41] R. Kienberger, E. Goulielmakis, M. Uiberacker, A. Baltuska, V. Yakovlev, F. Bammer, A. Scrinzi, Th. Westerwalbesloh, U. Kleineberg, U. Heinzmann, M. Drescher, and F. Krausz. Atomic transient recorder. *Nature*, **427**(26): 817–821.

[42] E. Goulielmakis, M. Uiberacker, R. Kienberger, A. Baltuska, V. Yakovlev, A. Scrinzi, Th. Westerwalbesloh, U. Kleineberg, M. Drescher, and F. Krausz. Direct measurement of light waves. *Science*, **305**(27): 1267–1269, 2004.

[43] S. Linden, H. Giessen, and J. Kuhl. XFROG - a new method for amplitude and phase characterization of weak ultrashort pulses. *Physica Status Solidi (B)*, **206**: 119–124, 1998.

[44] R. L. Fork, C. H. Brito Cruz, P. C. Becker, and C. V. Shank. Compression of optical pulses to six femtoseconds by using cubic phase compensation. *Optics Letters*, **12**(7): 483–485, 1987.

[45] Newlight Photonics Inc. Datasheet for α-BBO. Website, 2010. www.newlightphotonics.com/alpha-BBO-crystal.html.

[46] D. N. Nikogosyan. Beta barium borate (BBO). *Applied Physics A*, **52**: 359–368, 1991.

[47] Melles Griot. Dispersion-equations of optical materials. Website, 2010. http://www.cvimellesgriot.com/products/Documents/Catalog/Dispersion_Equations.pdf.

[48] R. Trebino. *Frequency-Resolved Optical Gating: The Measurement of Ultrashort Laser Pulses*. Kluwer Academic Publishers, Dordrecht, first edition, 2002.

[49] G. A. Reider. *Photonik, Eine Einführung in die Grundlagen*. Springer, Wien, second edition, 2004.

[50] D. E. Spence, P. N. Kean, and W. Sibbett. 60-fsec pulse generation from a self-mode-locked Ti:sapphire laser. *Optics Letters*, **16**(1): 42–44, 1991.

[51] M. Piché. Beam reshaping and self-mode-locking in nonlinear laser resonators. *Optics Communications*, **86**(2): 156–160, 1991.

[52] A. Stingl, M. Lenzner, Ch. Spielmann, F. Krausz, and R. Szipöcs. Sub-10-fs mirror-dispersion-controlled Ti:sapphire laser. *Optics Letters*, **20**(6): 602–604, 1995.

[53] P. M. W. French. The generation of ultrashort laser pulses. *Reports on progres in physics*, **58**(2): 169–262, 1995.

[54] R. Szipöcs, K. Ferencz, C. Spielmann, and F. Krausz. Chirped multilayer coatings for broadband dispersion control in femtosecond lasers. *Optics Letters*, **19**(3): 201–203, 1994.

[55] R. Strickland and G. Mourou. Compression of amplified chirped optical pulses. *Optics Communications*, **56**(7): 219–221, 1985.

[56] S. Sartania, Z. Cheng, M. Lenzner, G. Tempea, Ch. Spielmann, F. Krausz, and K. Ferencz. Generation of 0.1-tw 5-fs optical pulses at a 1-khz repetition rate. *Optics Letters*, **22**: 1562–1564, 1997.

[57] Femtolasers Produktionsgesellschaft GmbH. User manual for femtosecond multipass amplifier femtopower compact pro. 2001.

[58] S. A. Planas, N. L. P. Mansur, C. H. Brito Cruz, and H. L. Fragnito. Spectral narrowing in the propagation of chirped pulses in single-mode fibers. *Optics Letters*, **18**(9): 699–701, 1993.

[59] M. Nisoli, S. DeSilvestri, O. Svelto, R. Szipöcs, K. Ferencz, Ch. Spielmann, S. Sartania, and F. Krausz. Compression of high-energy laser pulses below 5 fs. *Optics Letters*, **22**(8): 522–524, 1997.

[60] A. Baltuška, Th. Udem, M. Uiberacker, M. Hentschel, E. Goulielmakis, Ch. Gohle, R. Holzwarth, V. S. Yakovlev, A. Scrinzi, T. W. Hänsch, and F. Krausz. Attosecond control of electronic processes by intense light fields. *Nature*, **421**(6): 611–615, 2003.

[61] T. Fuji, J. Rauschenberger, C. Gohle, A. Apolonski, T. Udem, V. Yakovlev, G. Tempea, T. Hänsch, and F. Krausz. Attosecond control of optical waveforms. *New Journal of Physics*, **7**(116), 2005.

[62] T. Fuji, A. Apolonski, and F. Krausz. Self-stabilization of carrier-envelope offset phase by use of difference-frequency generation. *Optics Letters*, **29**(6): 632–634, 2004.

[63] M. Zimmermann, C. Gohle, R. Holzwarth, T. Udem, and T. W. Hänsch. Optical clockwork with an offset-free difference-frequency comb: accuracy of sum- and difference-frequency generation. *Optics Letters*, **29**(3): 310–312, 2004.

[64] J. K. Ranka, R. S. Windeler, and A. Stentz. Visible continuum generation in air silica microstructure optical fibers with anomalous dispersion at 800 nm. *Optics Letters*, **25**(1): 25–27, 2000.

[65] I. P. Christov, M. M. Murnane, and H. C. Kapteyn. High-harmonic generation of attosecond pulses in the "single-cycle" regime. *Physical Review Letters*, **78**(7): 1251–1254, 1997.

[66] T. Kita, T. Harada, N. Nakano, and H. Kuroda. Mechanically ruled aberration-corrected concave gratings for a flat-field grazing-incidence spectrograph. *Applied Optics*, **22**(4): 512–513, 1993.

[67] M. Wagner and H. Schröder. A novel four grid ion reflector for saturation of laser multiphoton ionization yields in a time of flight mass spectrometer. *International Journal of Mass Spectrometry and Ion Processes*, **128**: 31–45, 1993.

[68] T. Pfeifer, M. J. Abel, P. M. Nagel, W. Boutu, M. J. Bell, Y. Liu, D. M. Neumark, and S. R. Leone. Measurement and optimization of isolated attosecond pulse contrast. *Optics Letters*, **34**(12): 1819–1821, 2009.

[69] M. Chini, H. Mashiko, H. Wang, S. Chen, C. Yun, S. Scott, S. Gilbertson, and Z. Chang. Delay control in attosecond pump-probe experiments. *Optics Express*, **17**(24): 21459–21464, 2009.

[70] F. M. Böttcher, B. Manschwetus, H. Rottke, N. Zhavoronkov, Z. Ansari, and W. Sandner. Interferometric long-term stabilization of a delay line: a tool for pump-probe photoelectron-photoion-coincidence spectroscopay on the attosecond time scale. *Applied Physics B*, **91**: 287–293, 2008.

[71] H. Merdji, T. Auguste, W. Boutu, J.-P. Caumes, B. Carré, T. Pfeifer, A. Jullien, D. M. Neumark, and S. R. Leone. Isolated attosecond pulses using a detuned second-harmonic field. *Optics Letters*, **32**: 3134–3136, 2009.

[72] E. Mansten, J. M. Dahlström, J. Mauritsson, T. Ruchon, A. L'Huillier, J. Tate, M. B. Gaarde, P. Eckle, A. Guandalini, M. Holler, F. Schapper, L. Gallmann, and U. Keller. Spectral signature of short attosecond pulse trains. *Physical Review Letters*, **102**: 083002, 2007.

[73] T. Wilhelm, J. Piel, and E. Riedle. Sub-20-fs pulses tunable across the visible from a blue-pumped single-pass noncollinear parametric converter. *Optics Letters*, **22**(19): 1494–1496, 1997.

[74] Max Planck Institute for Chemistry, Mainz. Spectral atlas of gaseous molecules. Website, 2010. http://www.atmosphere.mpg.de/enid/42416d7f1bc9fdca99b480d71e080185,0/Spectra/Quick_Search_5so.html.

[75] T. Fuji, T. Horio, and T. Suzuki. Generation of 12 fs deep-ultraviolet pulses by four-wave mixing through filamentation in neon gas. *Optics Letters*, **32**(17): 2481–2483, 2007.

[76] P. Baum, S. Lochbrunner, and E. Riedle. Tunable sub-10-fs ultraviolet pulses generated by achromatic frequency doubling. *Optics Letters*, **29**(14): 1686–1688, 2004.

[77] Ch. G. Durfee III, S. B. Backus, H. C. Kapteyn, and M. M. Murnane. Intense 8-fs pulse generation in the deep ultraviolet. *Optics Letters*, **24**(10): 697–699, 2004.

[78] S. A. Trushin, K. Kosma, W. Fuß, and W. E. Schmid. Sub-10-fs supercontinuum radiation generated by filamentation of few-cycle 800 nm pulses in argon. *Optics Letters*, **32**(16): 2432–2434, 2007.

[79] M. Li, J. P. Nibarger, C. Guo, and G. N. Gibson. Dispersion-free transient-grating frequency-resolved optical gating. *Applied Optics*, **38**(24): 5250–5253, 1999.

[80] T. S. Clement, A. J. Taylor, and D. J. Kane. Single-shot measurement of the amplitude and phase of ultrashort laser pulses in the violet. *Optics Letters*, **20**(1): 70–72, 1995.

[81] courtesy of Michael Hofstetter.

[82] courtesy of Justin Gagnon.

[83] E. D. Palik. *Handbook of optical constants of solids*. Academic Press, London, 1985.

[84] M. Uiberacker, Th. Uphues, M. Schultze, A. J. Verhoef, V. Yakovlev, M. F. Kling, J. Rauschenberger, N. M. Kabachnik, H. Schröder, M. Lezius, K. L. Kompa, H.-G. Muller, M. J. J. Vrakking, S. Hendel, U. Kleineberg, U. Heinzmann, M. Drescher, and F. Krausz. Attosecond real-time observation of electron tunneling in atoms. *Nature*, **446**: 627–632, 2007.

[85] Th. Uphues, M. Schultze, M. F. Kling, M. Uiberacker, S. Hendel, U. Heinzmann, N. M. Kabachnik, and M. Drescher. Ion-charge-state chronoscopy of cascaded atomic auger decay. *New Journal of Physics*, **10**: 025009, 2008.

[86] U. Becker and D. A. Shirley. *VUV and Soft X-Ray Photoionization*. Plenum Press, New York, 1996.

[87] M. Cardona and L. Ley. *Photoemission in Solids I: General Principles*. Springer Verlag, Berlin, 1978.

[88] M. Schultze, E. Goulielmakis, M. Uiberacker, M. Hofstetter, J. Kim, D. Kim, F. Krausz, and U. Kleineberg. Powerful 170-attosecond xuv pulses generated with few-cycle laser pulses and broadband multilayer optics. *New Journal of Physics*, **9**: 243, 2007.

[89] National Instruments (2006) Definition of VI "'Cubic Spline Fit.vi"' in Documentation of LabVIEW 8.2.

[90] M. Schultze, M. Fieß, N. Karpowicz, J. Gagnon, M. Korbman, M. Hofstetter, S. Neppl, A. Cavalieri, Y. Komninos, Th. Mercouris, C. A. Nicolaides, R. Pazourek, S. Nagele, J. Feist, J. Burgdörfer, A. M. Azzeer, R. Ernstorfer, R. Kienberger, U. Kleineberg, E. Goulielmakis, F. Krausz, and V. S. Yakovlev. Delay in photoemission. *Science, accepted*.

[91] E. Goulielmakis. PhD-thesis, Ludwig-Maximilians-Universität München. 2005.

[92] J. Schmidt, E. Goulielmakis, and V. S. Yakovlev. Modelling attosecond probing of electron wavepacket dynamics in non-aligned molecules. *Journal of Physics B: Atomic, Molecular and Optical Physics*, **41**(11), 2008.

[93] S. Y. Grebenshchikov, Z.-W. Qu, H. Zhu, and R. Schinke. New theoretical investigations of the photodissociation of ozone in the Hartley, Huggins, Chappuis, and Wulf bands. *Physical Chemistry Chemical Physics*, **9**: 2044–2064, 2007.

[94] P. M. Morse and H. Feshbach. *Methods of Theoretical Physics, Part I.* McGraw-Hill, New York, 1953.